

ELECTRO-OPTIC PHASE MODULATION, FREQUENCY COMB
GENERATION, NONLINEAR SPECTRAL BROADENING, AND
APPLICATIONS

A Dissertation

Submitted to the Faculty

of

Purdue University

by

Oscar E. Sandoval

In Partial Fulfillment of the
Requirements for the Degree

of

Doctor of Philosophy

August 2019

Purdue University

West Lafayette, Indiana

**THE PURDUE UNIVERSITY GRADUATE SCHOOL
STATEMENT OF DISSERTATION APPROVAL**

Dr. Andrew M. Weiner, Chair

School of Electrical and Computer Engineering

Dr. Peter Bermel

School of Electrical and Computer Engineering

Dr. Sunil A. Bhave

School of Electrical and Computer Engineering

Dr. Daniel S. Elliott

School of Electrical and Computer Engineering

Approved by:

Dr. Dimitrios Peroulis

Head of the School of Electrical and Computer Engineering

This work is dedicated to my family & friends who made this dream a reality. I missed a lot of birthdays, celebrations, and just days I could have been surrounded by all of you. I love you all, and thank you for supporting me in this endeavor. I hope you know you were always on my mind, and I hope you are proud of what I have done here. I strive to make sure I keep making you proud in the future. Los quiero mucho.

I want to especially thank my parents, Oscar and Georgina Sandoval, and younger brother, Jesse Sandoval. You sacrificed the most. You didn't question me when I told you I wanted to go to northwest Indiana and pursue my graduate studies. You let me go, through tears. Tears that we both shed, and do so every time we say goodbye. I hope you feel like this sacrifice was worth it. I hope I make you proud. I carry you with me everyday, and will for the rest of my life.

And to my grandparents Donato and Margarita Sandoval. Gracias por todos sus sacrificios. Gracias por siempre estar preocupados por mi. Los quiero mucho.

Purdue will always be a special place for me, it is here that I met the love of my life, Katie Hummel. I can't wait to see what the future has in store for us. You made the tough times a bit easier and the good times sweeter. Thank you for allowing me to be your teammate through life. Thank you for making me a better person. I hope you know that this is worth it because I get to share it with you. I love you! A lot!

What's next?

ACKNOWLEDGMENTS

I want to thank Professor Weiner for his continued support, his guidance, and for always treating me with empathy. Many professors would not have sacrificed their Friday mornings to go over E&M problems in order to ensure preparation for the QE. I leave here a better scientist because of his continued mentorship, thank you Professor.

Thank you to Dr. Dan Leaird for his help and for the enlightening research conversations. Dan is our lab manager, but he is much more than that. He is a reassuring presence.

To all my collaborators, it has been a pleasure to work alongside all of you.

To my committee members, Professor Bermel, Professor Elliott, and Professor Bhava, thank you for your guidance in the completion of this work.

And to the members of the Ultrafast Optics and Optical Fiber Communications Laboratory, it has been my privilege to be your colleague.

TABLE OF CONTENTS

	Page
LIST OF FIGURES	viii
ABBREVIATIONS	xiv
ABSTRACT	xvi
1 INTRODUCTION	1
1.1 The Optical Frequency Comb, from Self-Referenced to High Repetition Rate Combs	1
1.2 Generating High Repetition Rate Optical Frequency Combs via Electro- Optic Modulation	3
1.3 Spectral Broadening High Repetition Rate OFC	6
1.3.1 Methods for spectral broadening	7
1.4 Generation of Optical Frequency Combs in Microresonators via Four Wave Mixing	10
1.5 Dual Comb Spectroscopy	13
1.6 Biphoton Frequency Combs	15
1.7 Organization of Work	17
2 SPECTRAL BROADENING OF HIGH REPETITION RATE OPTICAL FREQUENCY COMBS EMPLOYING A NONLINEAR OPTICAL LOOP MIRROR	18
2.1 Spectral Broadening With the Aid of a Nonlinear Optical Loop Mirror	19
2.2 Nonlinear Optical Loop Mirror Scattering Matrix Formulation	21
2.3 Simulations of Effect of Number of Phase Modulators on Nonlinear Optical Loop Mirror Performance	27
3 CHARACTERIZATION OF SINGLE-SOLITON KERR COMBS VIA DUAL COMB ELECTRIC FIELD CROSS-CORRELATION	32
3.1 Achieving Mode-Locking in Microresonators	33
3.1.1 Bright soliton formation in anomalous dispersion microresonators	33

	Page
3.1.2 Pump line phase offset of single soliton Kerr comb	35
3.2 Dual Comb Electric Field Cross-Correlation Measurement for Study on Pump Line Phase Offset in Soliton Kerr Combs	37
3.2.1 Dual comb interferometry via electric field cross-correlation . . .	37
3.2.2 Signal comb - single-soliton Kerr comb sampled through drop port of silicon nitride microresonator	40
3.2.3 Reference comb - spectrally broadened electro-optic frequency comb	41
3.2.4 Retrieving phase of single-soliton Kerr comb via dual comb in- teferometry	46
3.2.5 Study on pump line phase offset of single-soliton Kerr comb . .	49
4 POLARIZATION DIVERSITY PHASE MODULATOR FOR MEASUR- ING FREQUENCY-BIN ENTANGLEMENT OF BI-PHOTON FREQUENCY COMBS IN A DEPOLARIZED CHANNEL	52
4.1 Motivation	53
4.2 Polarization Diversity Phase Modulator	54
4.3 Frequency Bin Entanglement Measurements	57
4.4 Cross-Polarized Signal and Idler Photon Pairs	64
4.5 Co- and Cross-Polarized Signal and Idler Photon Pairs in a Depolarized Biphoton Frequency Comb	65
4.6 Active Stabilization of Inteferometer	69
4.6.1 Interferometer active stabilization technique	69
4.6.2 Stabilization of classical light out of interferometer	71
4.6.3 Stabilization of classical light through the polarization diversity phase modulator	76
4.6.4 Effect of RF delay imbalance on the polarization state of light exiting the PDPM	80
5 CONCLUSION	84
5.1 Brief Summary	84
5.2 Future Outlook	85
REFERENCES	88

VITA 100

LIST OF FIGURES

Figure	Page
1.1 Application Wheel [5]. The applications on the left side of the wheel belong to the self-referenced frequency comb. The applications on the right belong to the higher rep-rate combs.	2
1.2 Cartoon depicting what an OFC looks like in the time domain (top), and in the frequency domain (bottom) [10]. The top figure also depicts the CEO arising from the shift between fast oscillating electric field and pulse envelope.	3
1.3 Depiction of the two types of four wave mixing taking place inside a microresonator, degenerate and nondegenerate four wave mixing [38].	10
1.4 A cartoon depicting a microring resonator with a bus waveguide [43].	12
1.5 (a) Cartoon depicting the basic concept of dual comb spectroscopy (DCS). The goal of DCS is to map the optical information to the RF domain. (b) The two types of DCS, asymmetric and symmetric [60].	14
1.6 (a) Optical frequency domain picture of dual comb spectroscopy DCS. (b) RF domain picture of DCS. (c) Time domain visualization of the reference and signal pulses walking through each other. (d) Oscilloscope picture of DCS [60].	15
1.7 The general depiction of a biphoton frequency comb (BFC) [90]. A BFC is a coherent superposition of N-energy matched frequency bins.	16
2.1 Example of broadened frequency comb with spectral ripple associated with residual third order phase. The residual third order phase manifests as temporal wings in the time domain.	19
2.2 Experimental setup for spectral broadening employing one NOLM stage and one NALM stage. [93].	20
2.3 Cartoon depicting NOLM comprised of a 2x2 power coupler and a length of HNLF. The NOLM is a Sagnac interferometer.	22
2.4 Plot of NOLM transmission; note the oscillatory behavior.	24
2.5 Experimental setup for removing residual third order wings via the NOLM.	25

Figure	Page
2.6 (a) OFC generated from 1 IM and 1 PM. (b) Comparison of AC trace of compressed pulse out of the EO comb generator. The compression is performed via a Fourier transform pulse shaper. Only linear chirp is compensated for.	26
2.7 (a) Spectrum out of the NOLM. (b) Corresponding time domain trace out of the NOLM; notice the removal of the third order dispersion wings. . . .	26
2.8 Simulated spectral results of one PM and one IM. The solid spectrum corresponds to compensating for all orders of spectral phase. And the dotted spectrum corresponds to compensating for only quadratic spectral phase.	29
2.9 Simulated spectral results of two PMs and one IM. The two different spectra correspond to either compensation of all orders of spectral phase (solid) or only quadratic spectral phase compensation (dotted).	30
2.10 Simulated spectral results of three PMs and one IM. The two different spectra correspond to either compensation of all orders of spectral phase (solid) or only quadratic spectral phase compensation (dotted).	30
2.11 Summary of simulation results. The lowest spectral ripple is from using only one PM. However, two PMs seems like a good compromise for low ripple and broad spectrum.	31
3.1 The signature of soliton generation. The transitions from a noisy chaotic state to N solitons. Further red detuning eventually leads to the single soliton regime [106].	34
3.2 Microscopic image of microresonator with through and drop ports.	35
3.3 (a) Optical spectra after EDFA and pulse shaper for pump wavelength of 1551.27nm (b) Autocorrelation data (blue) and simulation (red) based on measured spectrum assuming flat phase. Autocorrelation data with π phase shift applied to the pump (green).	36
3.4 Cartoons depicting the (a) setup and (b) spectra of the dual comb EFXC.	39
3.5 Single soliton generated in SiN microring resonator depicted in figure 3.2. This spectrum is taken from the drop port. Note the slight offset of the pump line arising from Raman interactions. The free spectral range (FSR) is 227.5 GHz.	41
3.6 Experimental setup for spectrally broadening electro-optic frequency comb for use as reference comb in the dual comb interferometry measurements.	42
3.7 Spectrum of electro-optic frequency comb generated from two phase modulators and one intensity modulator.	43

Figure	Page
3.8 Apodized EO comb and corresponding compressed AC trace.	43
3.9 The output of the nonlinear optical loop mirror.	44
3.10 The reference pulse used in the dual comb interferometry measurements.	45
3.11 The experimental setup for performing dual comb interferometry for characterization of single-soliton Kerr-comb [103].	46
3.12 (a) A portion of the measured time domain interferogram. (b) The reconstructed interferogram after compensating for fiber dispersion. The dashed box in (a) and (b) represent one period of the interferogram and the orange lines are the envelope of the interferogram. (c) The blue trace is the power spectrum of the interferogram. The orange trace is the retrieved phase of the different optical modes. The pump line exhibits a phase offset. The inset in (c) is the reconstructed intracavity waveform using the retrieved comb phase [103].	47
3.13 Results of pump line phase offset study with increasing pump wavelength. The data point indicated by the arrow corresponds to the data presented in figure 3.12c.	50
4.1 Schematic of the polarization diversity phase modulator (PDPM) – single-mode and polarization-maintaining fiber are depicted in red and blue, respectively. PBS - polarization beam splitter, VOA - variable optical attenuator, VODL - variable optical delay line, PM - phase modulator.	54
4.2 Progression of spectral ripple removal, signifying balancing the lengths of the arms of the PDPM.	55
4.3 Experimental setup for measuring frequency-bin entanglement in a BFC. Note that either a standalone phase modulator (PM) or polarization diversity phase modulator (PDPM) is used to mix frequencies in this arrangement.	57
4.4 (A), (D) show the change in power scattered into the +1 sideband, as a function of polarization, for a standalone PM and the PDPM, respectively. (B)-(C) show the change in coincidence and count rates for frequency-bin entanglement measurements using a standalone PM. (E)-(F) are analogous to (B)-(C) but for the PDPM and include data for two values of the joint phase – $\phi_{S_2} + \phi_{I_2} = 0$ (solid) and $\phi_{S_2} + \phi_{I_2} = \pi$ (hollow). Results are plotted on an azimuthal slice of the Poincaré sphere corresponding to linearly polarized light. (SA – slow axis and FA – fast axis)	60

Figure	Page	
4.5	Results from frequency-bin entanglement measurements. (A) Coincidences (blue) and counts (red) when using the standalone PM for three different orientations of the polarization - 0° (solid), 90° (dotted), and an intermediate state (dashed). (B) Coincidences and counts when using the PDPM for two cases - one where photons are equally likely to be in either arm (dashed) and the other where photons go entirely through one arm (solid). The insets show the relative orientation between the polarization of signal and idler bins.	62
4.6	The figures, going from left to right, contrast the performance of a standalone PM with the PDPM. Data for the PDPM is presented for two values of the joint phase ($\phi = \phi_{S2} + \phi_{I2}$) on S_2I_2 . Data for the the $\phi = \pi$ point was recorded to clearly establish that the coincidences recorded in (b) are the result of two-photon interference and not leakage from neighboring frequency-bins. (a) Coincidences and count rate, as a function of BFC polarization, in two-photon interference experiments when using standalone PM. (b)-(c) analogous to (a) but for the PDPM.	63
4.7	Frequency-bin entanglement measurements on orthogonally polarized signal-idler pairs using (A) a standalone PM and (B) the PDPM. Dashed and solid red lines correspond to the signal and idler count rates, respectively. The insets show the relative orientation between the polarization of signal and idler bins.	64
4.8	Experimental setup for state preparation and measurement of frequency-bin entanglement. PC – polarization controller and PMF – polarization maintaining fiber.	66
4.9	The effect of the polarization scrambler on the polarization state of the frequency-bin pairs when the launch condition is changed from 0° to 45° . PC – polarization controller and PMF – polarization maintaining fiber. The polarization scrambler effectively rotates the global polarization of the BFC.	67
4.10	Interference traces and visibilities from measurements of frequency-bin entanglement in a BFC. The performance of a standalone PM (blue) was compared with that of the PDPM (red). The experiments were carried out for both co- (A) and cross-polarized (B) signal idler pairs.	68
4.11	Block diagram of the feedback control loop for actively stabilizing the PDPM.	69

Figure	Page
4.12 Measured path length fluctuations through the PDPM when the interferometer is not stabilized. The top plot shows the photodetector (PD) voltage as a function of time. The data was recorded over 500 seconds and sampled every 0.5 ms. The bottom plot shows the spectrum of the path length fluctuations, the spectrum shows that the fluctuations are in the order seconds.	71
4.13 Setup to achieve and show active stabilization of classical light in an interferometer. DPC - deterministic polarization controller, PBS - polarization beam splitter, CW - continuous wave laser, PZT - piezo electric transducer (fiber phase shifter), PID - proportional integration derivative. $\lambda_{CW_1} = 1555$ nm and $\lambda_{CW_2} = 1545$ nm.	72
4.14 20 minute measurement of the output power of the stabilization laser (backwards path - orange arrows). This shows the interferometer being stabilized for the first 10 minutes and not being stabilized for last 10 minutes. For the data with stabilization on, the standard deviation of the fluctuations is $2.57 \mu\text{W}$, and for the stabilization off data the standard deviation is $150.36 \mu\text{W}$	74
4.15 20 minute measurement of optical power of classical light (forward propagation - purple arrows). This shows the interferometer being stabilized for the first 10 minutes and not being stabilized for last 10 minutes. The polarization setting on the DPC is set to a polarization ensuring light through both arms of the PDPM and causes this power imbalance between output ports of the test PBS. a - port A of the test PBS, b - port B of the test PBS.	75
4.16 Polarization stability of the classical light through the test interferometer as its polarization is swept from -90° to $+90^\circ$ in 10° increments. Power is recorded out of each port of the test PBS for 10 minutes at each polarization setting. a - port A of the test PBS. b - port B of the test PBS.	76
4.17 Experimental setup for active stabilization of the PDPM. The RF components necessary to balancing the PDPM electrically are now incorporated. This setup is used to demonstrate that the polarization transformation observed in figure 4.21 is due to the RF delay mismatch between the PMs.	77
4.18 20 minute measurement of stabilization laser output. The first ten minutes are with stabilization on (and RF delay balanced), and the last ten minutes are with stabilization off. For the data with stabilization on, the standard deviation of the fluctuations is $0.032 \mu\text{W}$, and for the stabilization off data the standard deviation is $152.36 \mu\text{W}$	78

Figure	Page
4.19 20 minute measurement of the polarization stability of the classical light in the forward propagation direction (purple arrow). a - port A of the test PBS. b - port B of the test PBS.	79
4.20 Polarization stability of the classical light through the PDPM with the PMs on and RF delay balanced as its polarization is swept from -60° to $+60^\circ$ in 10° increments (measured and controlled with the DPC at the forward input of the PDPM). Power is recorded out of each port of the test PBS for 5 minutes at each polarization setting. a – port A of the test PBS. b – port B of the test PBS. The extinction between the output ports of the test PBS is increased when the RF delay is balanced.	80
4.21 Polarization stability of the classical light through the PDPM with the PMs on and RF delay (purposefully) imbalanced. Polarization is swept from -50° to $+50^\circ$ in 10° increments (measured and controlled via DPC at input of PDPM). Power is recorded out of each port of the test PBS for 5 minutes at each polarization setting. a – port A of the test PBS. b – port B of the test PBS. Notice that in this iteration, there exists less extinction between the two output ports of the test PBS.	81
5.1 Example of dark pulse spectrum generated from a normal dispersion microresonator.	85
5.2 We expect to visualize the breathing dynamics of the dark breather by observing (purple) sidebands on the retrieved RF comb from the Dual Comb EFXC measurement.	86

ABBREVIATIONS

OFC	optical frequency comb
EO	electro-optic
FWM	four-wave mixing
RF	radio frequency
CEO	carrier envelope offset
PM	phase modulator
IM	intensity modulator
DDF	dispersion decreasing fiber
HNLF	highly nonlinear fiber
SPM	self-phase modulation
GVD	group velocity dispersion
CW	continuous wave
CMA-ES	covariance matrix adaptation evolution strategy
WGM	whispering gallery mode
SiN	silicon nitride
EFXC	electric field cross-correlation
DCS	dual comb spectroscopy
LLE	Lugiato-Lefever equation
NOLM	nonlinear optical loop mirror
NALM	nonlinear amplifying loop mirror
SMF	single mode fiber
AC	autocorrelation
FWHM	full width at half maximum
SSFM	split-step Fourier method

SHG	second-harmonic generation
BPD	balanced photo-detector
PDPM	polarization diversity phase modulator
VOA	variable optical attenuator
VODL	variable optical delay line
PBS	polarization beam splitter
SPDC	spontaneous parametric down conversion
PPLN	periodically poled lithium niobate
InP	indium phosphide
AWG	arrayed waveguide grating
MLL	mode-locked laser

ABSTRACT

Sandoval, Oscar E. Ph.D., Purdue University, August 2019. Electro-Optic Phase Modulation, Frequency Comb Generation, Nonlinear Spectral Broadening, and Applications. Major Professor: Andrew M. Weiner.

Electro-optic phase modulation can be used to generate high repetition rate optical frequency combs. The optical frequency comb (OFC) has garnered much attention upon its inception, acting as a crucial component in applications ranging from metrology and spectroscopy, to optical communications. Electro-optic frequency combs (EO combs) can be generated by concatenating an intensity modulator and phase modulator together. The first part of this work focuses on broadening the modest bandwidth inherent to the EO combs. This is achieved by propagation in a nonlinear medium, specifically propagation in a nonlinear optical loop mirror (NOLM). This allows for broadening the EO frequency comb spectrum to a bandwidth of 40 nm with a spectral power variation of $< 10\text{ dB}$. This spectrally broadened EO comb is then used in dual comb interferometry measurements to characterize the single soliton generated in an anomalous dispersion silicon-nitride microresonator. This measurement allows for rapid characterization with low average power. Finally, electro-optic phase modulation is used in a technique to prove frequency-bin entanglement. A quantum network based on optical fiber will require the ability to perform phase modulation independent of photon polarization due to propagation in optical fiber scrambling the polarization of input light. Commercially available phase modulators are inherently dependent on the polarization state of input light making them unsuited to be used in such a depolarized environment. This limitation is overcome by implementing a polarization diversity scheme to measure frequency-bin entanglement for arbitrary orientations of co- and cross- polarized frequency-bin entangled photon pairs.

1. INTRODUCTION

1.1 The Optical Frequency Comb, from Self-Referenced to High Repetition Rate Combs

The femtosecond optical frequency comb (OFC) garnered much attention in the fields of optical synthesis and metrology [1] during its birth in 2000 [2–4]. As its popularity grew, so did its application portfolio. Its applications began to include molecular spectroscopy, optical clocks, and optical/radio-frequency (RF) arbitrary waveform generation [5]. The impact of the OFC was so great, the 2005 Nobel Prize in physics was shared by T.W. Hansch and J.L. Hall. The type of comb used for this Nobel winning work, and work done on the left side of the application wheel presented in figure 1.1 [5], is the so-called self-referenced comb, which offers higher precision and accuracy. This type of comb is octave spanning (f - $2f$) and is used to determine the absolute position of the frequency components. If the reader desires more insight into the development of the self-referenced OFC, reference [6] offers quite an intriguing account of the progression and development of this flavor of comb.

However, this type of comb only offers repetition rates (rep-rate) below GHz levels, except for one notable exception [7]. For applications on the right side of the application wheel, fig. 1.1, a different type of comb is required. Applications ranging from LIDAR, arbitrary optical/RF waveform generation [8], and further optical communication techniques require a different flavor of comb. The comb desired for these applications is one that is more robust and simple to implement and, more importantly, offers repetition rates > 10 GHz. This type of comb will be referred to as the high rep-rate comb and is the focus of this document. The high rep-rate comb is less demanding in terms of bandwidth and absolute frequency stabilization, but it

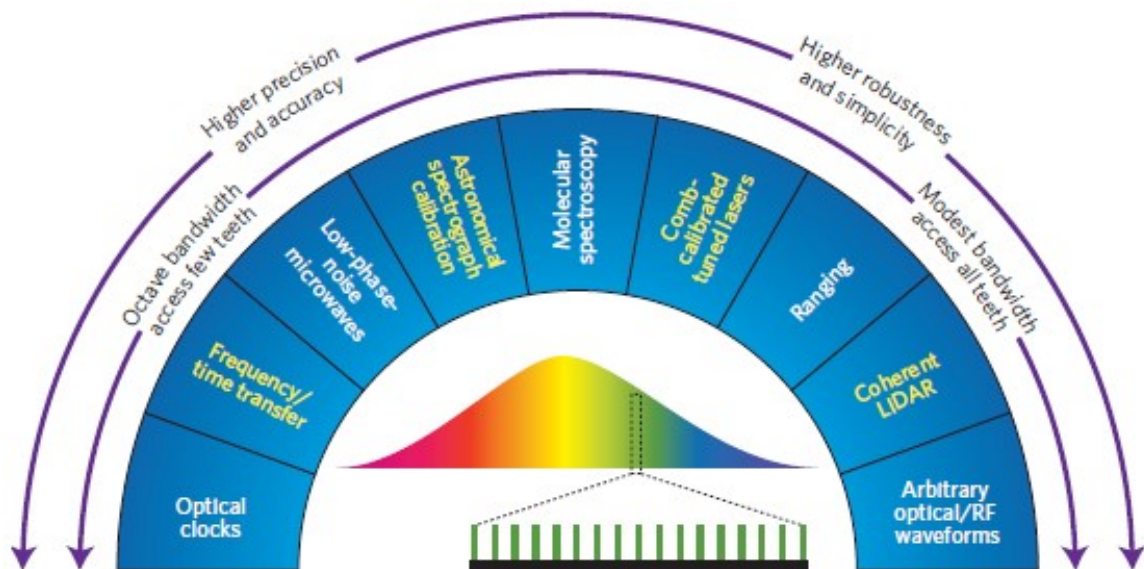


Fig. 1.1.: Application Wheel [5]. The applications on the left side of the wheel belong to the self-referenced frequency comb. The applications on the right belong to the higher rep-rate combs.

does require the ability to independently tune the central frequency and repetition rate.

A high repetition rate OFC with relatively broad optical bandwidth and low noise level offers a huge new avenue of possibilities not only in microwave photonics [9], but also in applications that will be presented in the following document. However, the high rep-rate comb is not as broad as its self-referenced counterpart. Therefore, methods for broadening the spectrum of these high-rep rate combs is of interest.

The aim of this work was not to create a very broad (> 100 nm) comb with extremely low spectral flatness (< 5 dB). Instead, the aim of this work is to present a relatively broad frequency comb comprised of commercially available components that can be used in applications needing the ability to tune the center wavelength and repetition rate of the OFC. Before diving into the rest of this work, the following

section will introduce the reader to an overview of generating high rep-rate OFC via electro-optic modulation.

1.2 Generating High Repetition Rate Optical Frequency Combs via Electro-Optic Modulation

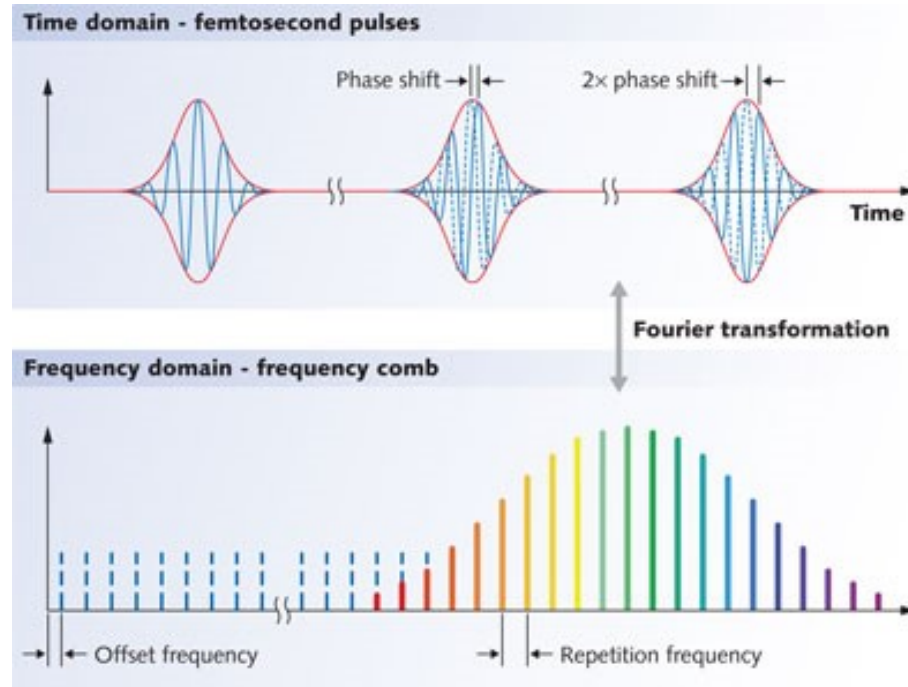


Fig. 1.2.: Cartoon depicting what an OFC looks like in the time domain (top), and in the frequency domain (bottom) [10]. The top figure also depicts the CEO arising from the shift between fast oscillating electric field and pulse envelope.

A frequency comb is a light source, whose spectrum consists of evenly spaced components [5]. However, for a light source to be labeled a frequency comb, it must also meet the following parameters [9]. Figure 1.2 shows that an OFC in the frequency domain looks like a series of evenly spaced delta Dirac functions, and in the time domain, like a series of optical pulses.

1. Maintain high spectral coherence across the entire bandwidth.

2. Possess the ability to synthesize in an independent manner the repetition rate of the comb.

A frequency comb can be thought of as an equidistant array of delta-function, see equation 1.1.

$$E(\omega) = \sum_N A_N \delta(\omega - \omega_N) e^{j\phi_N} \quad (1.1)$$

Where A_N and ϕ_N are the amplitude and spectral phase of the Nth comb line, respectively. δ is the Kronecker delta function, ω is the carrier frequency, and ω_N is the position of the Nth comb line. If the pulses generated by the laser were identical, then the absolute positions of the spectral components would be integer multiples of the laser repetition rate. However, due to dispersion and nonlinearities, there is a slip, known as the Carrier Envelope Offset (CEO). This arises from the constant shifts in the oscillation of the electric field with respect to the pulse envelope. Therefore, the position of the Nth comb, ω_N , is given by equation 1.2.

$$\omega_N = N\Delta\omega + \delta\omega \quad (1.2)$$

Where N is an integer, $\Delta\omega$ is the frequency spacing of the lines, and is defined as $\Delta\omega = \frac{f_{\text{rep}}}{2\pi}$, where f_{rep} is the rep-rate of the frequency comb. Finally, $\delta\omega$ is the CEO frequency. In 2005 T. W. Hanch and J. L. Hall were awarded half of the Nobel Prize in physics for their efforts in determining the CEO frequency via Self-Referencing. In Self-Referencing, the phases of frequency components spaced by an octave (f to 2f) are compared to determine and lock the CEO frequency. This allows for precise stabilization of the frequency components at a known location. The reader is pointed to their Nobel lectures for further insight [11, 12].

The second parameter that needs to be met for a light source to be labeled a frequency comb is the possibility to change the repetition rate i.e. the frequency spacing of the lines in an independent manner. For these self-referenced combs, the ability to change the repetition rate is a difficult process, usually involving the

stabilization of the laser cavity. Therefore, the need for a different flavor of comb is re-iterated.

Reference [9] reviews the idea of opto-electronic frequency comb generators. The idea is to send a CW laser into an opto-electronic system driven by an RF source. At the output of the opto-electronic system a frequency comb will be generated. This idea was first proposed in the 60s [13] and in the 70s and 80s was researched as a means of generating picosecond pulses [14, 15]. Usually the opto-electronic system will be comprised of an electro-optic intensity or phase modulator, or a combination of both. In 2003 Fujiwara et al. developed a flat top high rep-rate frequency comb by concatenating an intensity modulator (IM) and a PM phase modulator (PM) [16]. This is the method our group employs to generate high rep-rate combs electro-optically. The idea is that the IM carves out a train of pseudo square pulses from the input CW laser. The PM imparts a quadratic phase on each pulse. The carving of the pulses is timed so that it occurs when the chirping imparted by the PM is linear. This is the impetus that creates the flat top spectrum. Previously, only phase modulation was used in generating these electro-optic combs, but by phase modulation alone, the spectral lines suffer from significant line-to-line amplitude variations [17].

The phase imparted onto the CW laser is given by equation 1.3.

$$\Phi = \frac{\pi V}{V_\pi} \cos(2\pi ft) \quad (1.3)$$

Where V and f are the maximum voltage and frequency of the RF signal from the RF oscillator, respectively. And V_π is an important parameter inherent to the electro-optic coefficient of the material and the waveguide structure of the modulator, known as the Half-Wave Voltage. This parameter gives information on the amount of RF power needed for generation of a π phase shift.

Another important parameter in these electro-optic modulated frequency combs is the modulation index, given in equation 1.4.

$$\Delta\theta = \frac{\pi V}{V_\pi} \quad (1.4)$$

To obtain a broad optical bandwidth, the modulation index must be high. To maximize the value of the modulation index, a modulator with a low V_π and capable of accepting a high RF voltage (V) is desired.

One way to increase the value of the modulation index is by placing multiple PMs in tandem. This is because the effective V_π is given by equation 1.5.

$$V_{\pi\text{eff}} = \left(\frac{1}{\sum_{i=1}^N V_{\pi i}} \right)^{-1} \quad (1.5)$$

Therefore, as more phase modulators are cascaded, the effective V_π is decreased and the modulation index is increased.

1.3 Spectral Broadening High Repetition Rate OFC

Many of the high repetition rate comb generators provide a spectrum of modest bandwidth. For some applications a broader comb may be needed. Therefore, broadening these types of combs is an area of research that has garnered much attention. A brief review of different methods for achieving spectral broadening of high repetition rate frequency combs follows. Most take advantage of the fact that these types of OFC generators output optical pulses in the $1 \sim 10$ ps regime, making them useful in achieving spectral broadening in a highly nonlinear passive medium [9].

The passive medium in which spectral broadening is realized can have two types of dispersion. To briefly describe the differences between the two, the following explanation has been adapted from [18, 19]. Presuming a Fourier transform limited pulse, upon propagation in an anomalous dispersion material, the higher frequency components travel faster than the lower frequency components, i.e., the leading edge of the pulse is blue shifted and the trailing edge of the pulse is red shifted. D is the dispersion parameter and it has units of ps/nm/km. For anomalous dispersion $D > 0$. In the case of propagation in a normal dispersion material, the higher frequency components of the pulse travel slower than the lower frequency components, i.e., the leading edge of the pulse is red shifted and the trailing edge of the pulse is

blue shifted. For normal dispersion $D < 0$. In each of these dispersion regimes, the method for achieving spectral broadening is different. Here we begin the brief review on methods for achieving spectral broadening of high repetition rate frequency combs.

1.3.1 Methods for spectral broadening

In anomalous dispersion, modulation instability can lead to amplification of small amounts of input noise that can lead to the degradation of the spectral coherence of the comb [20]. Therefore, the dispersion profile of the external nonlinear fiber must be carefully chosen, which is why dispersion decreasing fibers (DDF) are attractive for nonlinear broadening in the anomalous dispersion regime. These types of fibers can lead to significant broadening [21, 22] and pulse compression through a process known as adiabatic soliton compression [18]. Further examples of broadening in DDF are shown in [23] and [24].

In the normal dispersion regime, modulation instability is not a problem. In this regime, spectral broadening can be achieved by launching the short pulses into a highly nonlinear fiber (HNLF). In normal dispersion HNLF, the physical mechanism leading to spectral broadening is self-phase modulation (SPM) [18, 25]. SPM stems from the optical Kerr effect, which is a change in the refractive index due to an applied electric field. It is important to note that SPM is also present in the anomalous dispersion regime, but the interplay between the group velocity dispersion (GVD) and SPM balance each other and can lead to the formations of solitons [18]. In the normal dispersion regime, SPM and GVD act in concert and lead to a time varying phase that modifies the spectrum by adding new spectral components, i.e., spectral broadening. SPM is dependent on the intensity of the optical pulse. Therefore, increasing the power of the pulse will lead to an increase in spectral broadening. This is the method of choice for the spectral broadening in this work, because it is simple to implement with commercially available HNLF.

In reference [26], the authors show spectral broadening in 1km of normal dispersion HNLF. And more recently, at CLEO in 2017, Metcalf et al., [27], showed spectral broadening in normal dispersion HNLF at the 1 μ m wavelength.

Along with employing normal dispersion HNLF, work has been done in shaping or apodizing the seed pulse prior to being launched into the nonlinear fiber. In [26, 28], and [29] the seed spectrum was shaped into a parabola prior to being launched into the HNLF. By seeding the HNLF with a pulse having a spectrum that is nearly Gaussian, this can lead to a flat broadened spectrum by taking advantage of the notions of optical wave-breaking [30]. In optical wave-breaking, different frequency components generated by SPM meet and interfere at the same time location. This occurrence can lead to an enhancement of the flatness of the central region of the spectrum [31].

Alternatively, another nonlinear effect called four-wave mixing (FWM) can be exploited to achieve broadening. In FWM the $\chi^{(3)}$ response of the nonlinear medium is used to reshape the complex field of the input waveform in order to obtain the desired spectral profile. In an example of this work, reference [32], two narrow bandwidth combs are centered at different wavelengths and are mixed in a length of HNLF. The nonlinear interaction leads to the generation of new frequency combs centered about other frequency components through a cascade of FWM. If the system is properly phase matched, this can lead to a power enhancement that simultaneously broadens the comb and preserves flatness. Further examples of this method can be found in [28, 33, 34]. It should be noted, however, that the two seed combs need to be phase-locked in order to achieve a broader comb that can retain long term frequency stability [9], thus adding to the intricacy of this method.

Further increasing the complexity of the nonlinear medium, in 2011 Kuo et al., reference [35], introduced a technique based on two-pump parametric mixing. By precisely managing the dispersion of the HNLF that served as the mixer, they generated a broadened comb with 140 nm bandwidth. Along the same path, in 2012 Myslevits et al. re-hashed the precise dispersion management of the HNLF. In this

two stage HNLF setup, they controlled the dispersion characteristics of the HNLF by inserting strain on the fiber [36]. In this work, two CW tones can be spaced arbitrarily apart to generate a comb frequency pitch (rep-rate). By inducing strain-synthesized dispersion, they can induce phase matching, and thus generate a 150 nm broad frequency comb. This broadening is impressive, but it should be noted that the HNLF used in this work is a specialty fiber and the strain-induced dispersion increases the complexity of this scheme.

The above references used two CW lasers for parametric mixing in HNLF to generate a frequency comb. In the following technique for spectral broadening, they also use two CW lasers for seeding a broadening stage [17]. One CW (CW1) laser is used in an electro-optic comb generator comprised of one intensity modulator (IM) and one PM. The second CW (CW2) laser is not modulated, and combined with the generated frequency comb from CW1. This is the same FWM scheme in [32]. The difference is that instead of using 100m of HNLF to spectrally broaden the FWM generated comb, a 1cm long silicon waveguide is used. They claim the silicon waveguide has a nonlinear parameter 3 orders of magnitude greater than the HNLF. The nonlinear parameter of the silicon waveguide is $10^3 \frac{\text{rad}}{\text{W}\cdot\text{km}}$ and the nonlinear parameter of the HNLF is $1.72 \frac{\text{rad}}{\text{W}\cdot\text{km}}$. They generated a broadened frequency comb with more than 100 lines at a rep-rate of 10 GHz.

Finally, one last interesting method of generating spectrally broadened frequency combs is via a technique called adaptive pulse shaping [37]. The idea is to pre-shape the comb being launched into the HNLF to obtain the desired spectral shape after the HNLF. They use an algorithm based off the covariance matrix adaptation evolution strategy (CMA-ES). By monitoring the spectrum out of the HNLF, they can continually shape the spectrum before the HNLF, via a pulse shaper, until they achieve a flat broadened comb. This method generated a 26nm broad comb at a rep-rate of 10 GHz.

1.4 Generation of Optical Frequency Combs in Microresonators via Four Wave Mixing

Looking to the future of optical frequency comb generators, the next approach will require reducing their size, cost, weight, and power consumption. This will allow for the application of optical frequency generators outside of the laboratory environment [9].

A new principle has emerged that uses parametric frequency conversion in high resonance quality factor microresonators [38]. This new approach may allow for chip-scale integration and applications in astronomy, microwave photonics, and telecommunications [38]. Of note, two different references have shown on-chip comb generation with an incorporated compact pump laser, [39] and [40].

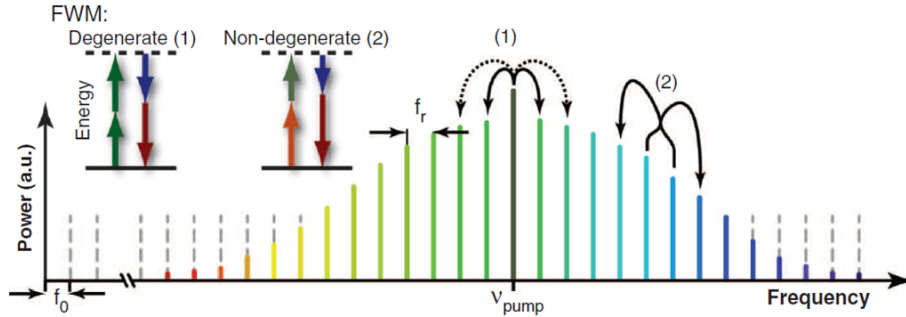


Fig. 1.3.: Depiction of the two types of four wave mixing taking place inside a microresonator, degenerate and nondegenerate four wave mixing [38].

The following explanation of the nonlinear process in the cavity is adapted from references [41] and [38]. Parametric oscillation occurs when the round trip parametric gain exceeds the loss in the cavity. The parametric oscillations stem from the third order nonlinear parametric process known as four wave mixing (FWM). FWM occurs when two pump photons are converted into an up-shifted “signal” photon, and a down-shifted “idler” photon, conserving energy in the process. The efficiency of the FWM process depends on the pump intensity, waveguide nonlinearity, interaction length, and the degree of phase mismatch. Phase matching allows the generated light

to add up constructively along the length of the waveguide. Parametric gain requires not only phase matching, but also requires relatively high optical intensity and long interaction length.

An advantage of the optical microresonator is the fact that the threshold for comb generation scales with the inverse of the quality (Q) factor squared. Therefore, a high Q leads to a dramatic reduction in required optical power.

The parametric oscillation leads to spectra containing multiple sidebands, i.e., frequency combs. Two nonlinear processes lead to comb generation, see figure 1.3. The first is the “degenerate” FWM process. This process generates photons from the same frequency i.e., the signal and idler photon have the same parent photon. The second process is the “nondegenerate” FWM. In this process photons are generated from different frequencies. It is termed nondegenerate FWM because the two pump photons have different frequencies.

In an ideal setting, the cavity would confine light indefinitely, and would have resonant frequencies at precise values [42]. However, due to dispersion, this ideal case is not possible. The dispersion of the cavity leads to variations of the free spectral range (FSR) of the cavity and limits the conversion process, thus limiting the bandwidth of the generated comb. FWM becomes less efficient when the comb modes are no longer in resonance with the cavity modes. Therefore, having the ability to control the dispersion of the cavity by controlling the thickness of the waveguide, [41], allows for better phase matching and FWM enhancement.

Resonance in microresonators occur when the optical path length of the resonator is exactly a whole number of wavelengths, or when the waves in the microresonator interfere constructively due to the accumulation of a phase shift that is an integer multiple of 2π [43]. The microresonators support multiple resonances, and the spacing between these resonances is the FSR, which is dependent on the length of the resonator.

Microresonators employ different geometries. For instance, the geometry used in the seminal work by Del’Haye et al., [44], was toroidal. This type of microresonator be-

longs to a certain subset known as whispering gallery mode (WGM) microresonators. This geometry confines light by total internal reflection around an air-dielectric interface and relies on the curvature of the surface to reflect the light [38]. This type of microresonator was demonstrated in reference [45] using microspheres having ultra-high Q factors (>100 million). Further examples of WGM microresonators are microdisks and microspheres [44].

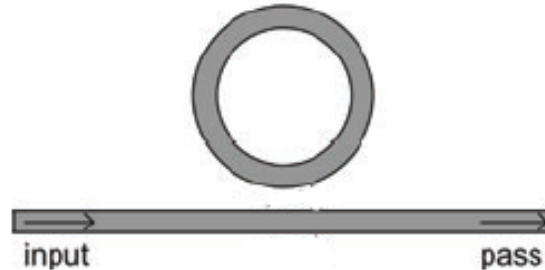


Fig. 1.4.: A cartoon depicting a microring resonator with a bus waveguide [43].

An example of a different type of microresonator geometry is the microring resonator, which is an optical waveguide that is looped back on itself [43], depicted in figure 1.4. In this geometry, evanescent coupling is leveraged to couple light between a bus waveguide and a ring resonator. The light will be stored in the ring resonator due to its high Q. This is the type of geometry employed in the work presented in chapter 3.

Microresonators also employ different materials. Examples of different materials are silica [44, 46–49], calcium fluoride [50–52], magnesium fluoride [53–55], fused quartz [56], and silicon nitride (SiN) [41, 57–59].

Silicon nitride waveguide resonators offer the possibility of being integrated onto photonic chips that can generate and transfer optical signals directly on chips. They are also typically compact, low-cost, and a convenient way to develop future telecommunication and optical interconnects. Silicon nitride is compatible with the CMOS fabrication standard. This offers the possibility for integration with other subsystems all in one chip [9]. Examples of these subsystems are multiplexers and modulators.

Due to their ultra-high repetition rates and compactness, they have become attractive as a multi-wavelength source for [38] optical communications, optical interconnects, astronomical spectrometers, and broad-band RF photonics. Therefore, it is the platform of choice for the microring resonators used in the work presented in chapter 3.

1.5 Dual Comb Spectroscopy

The single soliton physics in a SiN microring is of interest. To study the phase of such a phenomena, a dual comb electric field cross-correlation technique (EFXC) is employed. The measurements technique is based off of dual comb spectroscopy (DCS), which is why the following review, adapted from [60], is presented. This review focuses on DCS applied to linear spectroscopy as a broadband coherent system. But recently, DCS has been modified to characterize telecommunication components, fiber gratings, and microresonators [61–63]. Further modification to the DCS approach has allowed for the monitoring of active sources, such as static and fast-swept CW waveforms [64–66], pulsed or incoherent sources [67,68], and arbitrary optical waveforms [69–71]. All these techniques, including the dual comb EFXC, possess the underlying dual-comb/single-receiver architecture of DCS. And they are ultimately no more than a simple extension of standard heterodyne laser interferometry to frequency comb sources [60].

In DCS, the strengths of conventional broadband spectroscopy and tunable laser spectroscopy are combined into a single platform allowing for a broad range of the optical spectrum to be analyzed with the use of only one single photodetector [60]. DCS can provide comb-tooth-resolved spectra [72,73] and high signal-to-noise ratio (SNR) over broad optical bandwidths in the near-IR [74,75]. Since its first demonstrations, [76–79], DCS has an application portfolio including ultrabroadband near-IR spectroscopy [75], near-field microscopy for subwavelength spatial resolution [80], precision line centers [75,81,82], spectral LiDAR [83,84], and greenhouse gas monitor-

ing [85,86]. And most recently, DCS has been extended to nonlinear spectroscopy for stimulated Raman scattering based coherent anti-Stokes Raman spectroscopy [87,88] and two-photon spectroscopy [89].

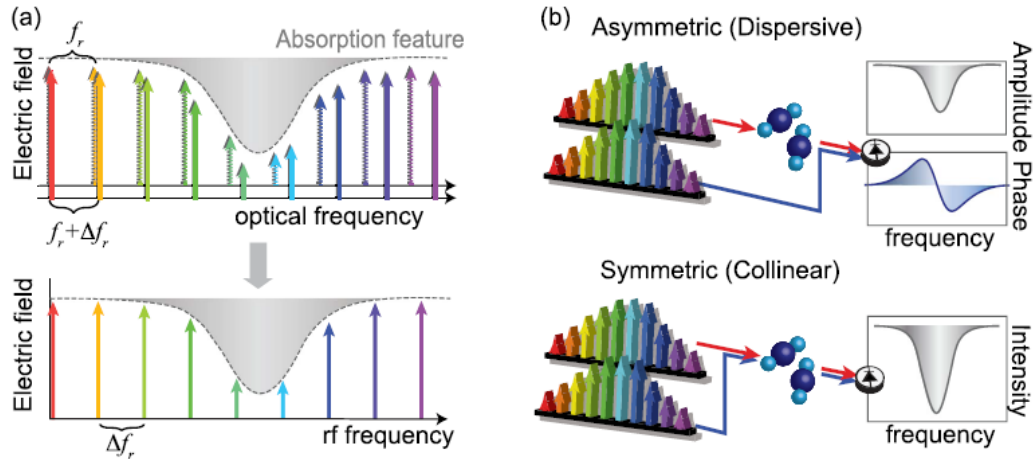


Fig. 1.5.: (a) Cartoon depicting the basic concept of dual comb spectroscopy (DCS). The goal of DCS is to map the optical information to the RF domain. (b) The two types of DCS, asymmetric and symmetric [60].

Figure 1.5 depicts the basic concept of DCS. Two frequency combs with different repetition rates are beat together at a photodiode. This beating generates an RF comb that is composed of distinguishable heterodyne beats between pairs of optical comb components. This RF comb can easily be characterized with RF electronics, and holds all necessary information of the optical comb spectra. Spectroscopy is performed by either having both optical beams pass through the sample (symmetric) or only one (asymmetric).

Figure 1.6 gives a frequency and time domain view of the DCS. Two combs are beat to produce an RF comb. The intensity and phase of the detected RF comb are proportional to the product of the electric fields of the two optical combs. In essence, DCS maps the optical combs to the RF domain. The repetition rate difference determines the time to acquire a single spectrum. In the time domain, a large burst corresponds to simultaneous arrival of two pulses and in the tails ringing corresponds

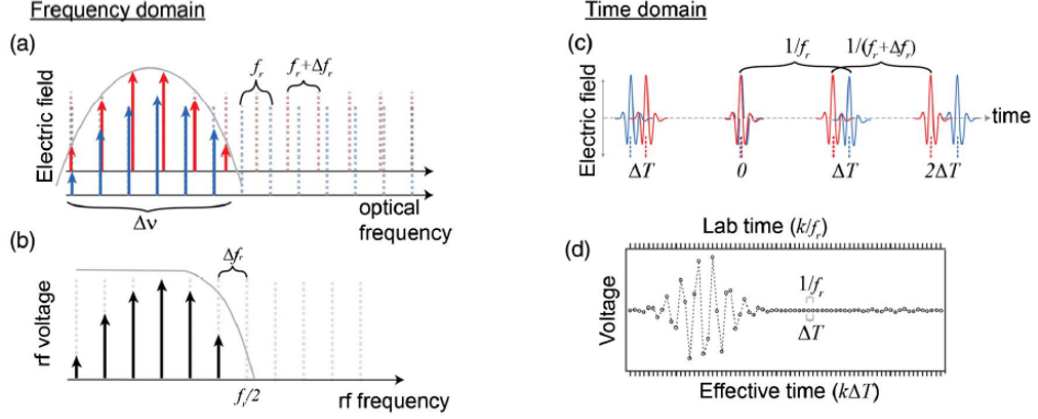


Fig. 1.6.: (a) Optical frequency domain picture of dual comb spectroscopy DCS. (b) RF domain picture of DCS. (c) Time domain visualization of the reference and signal pulses walking through each other. (d) Oscilloscope picture of DCS [60].

to the absorption information of the sample. It is important to note that absorption information is not of interest in this work, waveform reconstruction is. More elaboration presented in chapter 3.

1.6 Biphoton Frequency Combs

So far, we have dealt with what we can call “classical” combs. The last chapter of this dissertation will deal with their quantum counterpart. The last chapter deals with quantum entanglement, specifically entangled photons known as “biphotons”. There exist many degrees of freedom in which entanglement can be prepared, but entanglement in the frequency domain is chosen for its compatibility with current optical fiber networks and for its robustness against noise while propagating through the optical fiber [90]. Recently, colleagues in our research group, and in parallel researchers in the Nonlinear Photonics Group at the National Institute of Scientific Research in Montreal, showed the entanglement in a biphoton frequency comb (BFC) generated via FWM in a microresonator [91,92]. The BFC is a coherent superposition

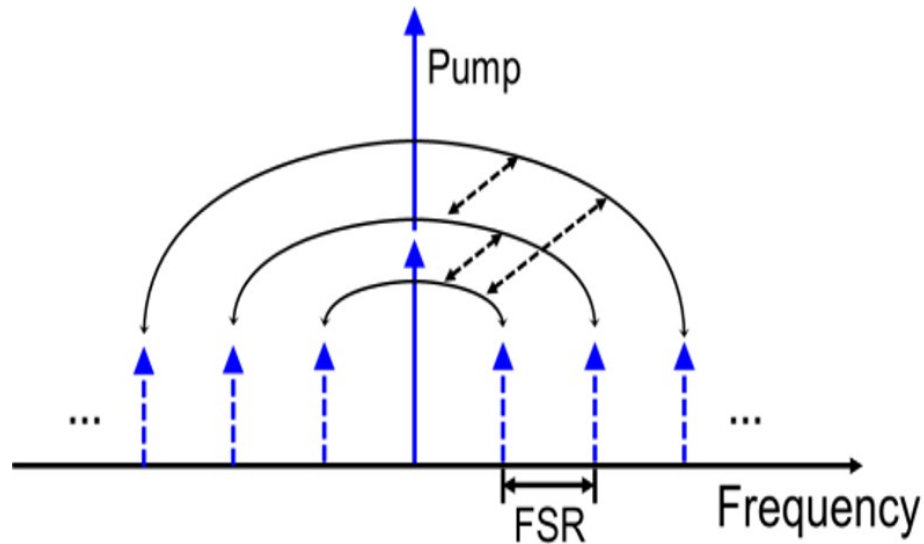


Fig. 1.7.: The general depiction of a biphoton frequency comb (BFC) [90]. A BFC is a coherent superposition of N -energy matched frequency bins.

of N -energy matched frequency bins, depicted in figure 1.7 and it is a specific state of frequency entangled biphotons.

Previous work [90–92] has shown methods for proving entanglement in a BFC. These methods make the use of commercially available electro-optic phase modulators to show the spectral coherence between frequency bin pairs, and thus the quantum entanglement in the BFC. The goal of these measurements is to create indistinguishable superposition states by projecting the frequency bins onto the sidebands generated via phase modulation, more on this in chapter 4. However, commercially available phase modulators are polarization dependent. Colleagues at the US Army Research Laboratory, collaborators of work presented in chapter 4, want to harness the power of hyperentanglement, entanglement in more than one degree of freedom, in the frequency and polarization degrees of freedom to reach the ultimate goal of creating a quantum network that is based on current fiber optic infrastructure. The problem that arises is that as light propagates through a fiber, its polarization scrambles. This is detrimental to performing phase modulation with the commercially available

electro-optic phase modulators. Therefore, to reach the goal of a fiber optic quantum network, a phase modulator capable of phase modulation irrespective of polarization state is needed. The final chapter of this dissertation introduces the polarization diversity phase modulator (PDPM), a device that can perform such polarization independent phase modulation.

1.7 Organization of Work

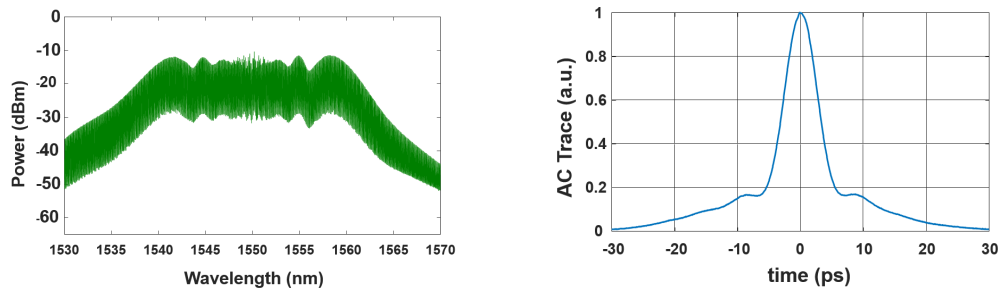
Chapter 2 will introduce the reader to the nonlinear optical loop mirror and how it is used to spectrally broaden frequency combs generated electro-optically. In chapter 3, the spectrally broadened EO comb is used as a reference in a dual comb EFXC measurement to characterize single soliton pulses generated in SiN microring resonators. In chapter 4, a polarization diversity phase modulator will be introduced to circumvent the intrinsic property of polarization dependence of commercial phase modulators. Finally, in chapter 5, the conclusion and an outlook of future work is presented.

2. SPECTRAL BROADENING OF HIGH REPETITION RATE OPTICAL FREQUENCY COMBS EMPLOYING A NONLINEAR OPTICAL LOOP MIRROR

In the previous chapter various methods for broadening the modest bandwidth of electro-optic frequency combs were presented. Various applications require more bandwidth, but they also require a flat spectrum. By having a flat spectrum it is meant that each comb line has the same intensity. In communication applications, data will be imparted on each frequency component (comb line). If the intensity of the lines are different, then this will lead to errors in the data transmission. Therefore, the goal of most spectral broadening experiments is to increase the bandwidth while preserving its flatness. This is a difficult task due to the spectral ripple, power variation among spectral lines, stemming from dispersion and other effects in the fiber propagation. Very impressive techniques were presented that allowed for excess of 100 nm bandwidths with very low spectral ripple. However, the complexity, and cost, of these techniques makes them difficult to implement. Therefore, in this chapter, the nonlinear optical loop mirror is presented. This all fiber device allows for removal of the third-order dispersion that is the culprit for spectral ripple formation. It is a simple setup, that when implemented successfully allowed for the broadening of an electro-optic frequency comb. Simulations are presented in which the number of phase modulators in the electro-optic frequency comb generator is varied. This allows for the determination of the best configuration to get the best balance between spectral flatness and broadening.

2.1 Spectral Broadening With the Aid of a Nonlinear Optical Loop Mirror

The goal of spectral broadening is to generate more spectral lines while preserving flatness. When launching a pulse into a nonlinear medium, HNLF for instance, the seed pulse should be transform limited, i.e., chirp free. Residual chirp on the seed pulse can lead to amplitude variations in the spectrum out of the nonlinear medium. These amplitude variations will be known as spectral ripple in this work, and an example of spectral ripple is shown in figure 2.1a. It has been shown that the major cause of spectral ripple is the residual third order phase on the seed pulse [93]. Third order phase appears as temporal wings; an example is shown in figure 2.1b.



(a) An example spectrum out of a length of highly nonlinear fiber (HNLF), depicting the spectral ripple associated with residual third order phase.

(b) An example autocorrelation (AC) trace showing the temporal wings associated with residual third order phase.

Fig. 2.1.: Example of broadened frequency comb with spectral ripple associated with residual third order phase. The residual third order phase manifests as temporal wings in the time domain.

The focus of the following chapter will be to introduce a method to remove the third order wings from the seed pulse and thereby obtain a flatter comb out of the nonlinear medium.

In 1988 Doran and Wood introduced the nonlinear optical loop mirror (NOLM) [94]. In its introduction, it garnered attention for applications in fast optical switching for signal processing and communications [94, 95] and as a means for mode locking a laser as a fast-saturable absorber [96]. But the application that makes the NOLM attractive for the work in this document is its capability of re-shaping optical pulses.

Smith, Doran, and Wigley introduced the pulse shaping concept [97]. In this work, optical pulses with temporal pedestals are launched into the NOLM comprised of fiber that has low and normal dispersion. Upon exiting the NOLM, the pulses are cleaned up i.e., the temporal pedestals are removed. But the NOLM's effectiveness in pedestal suppression does not have to only apply to applications in optical communications. It can be used to facilitate more effective spectral broadening, as was shown by Ataie et al. in 2014.

In reference [93], Ataie et al. use one NOLM and one nonlinear amplifying loop mirror (NALM) [98] to generate a comb with 120 nm bandwidth and with 2 dB of spectral flatness. The setup used in generating this impressive broadening is shown in figure 2.2.

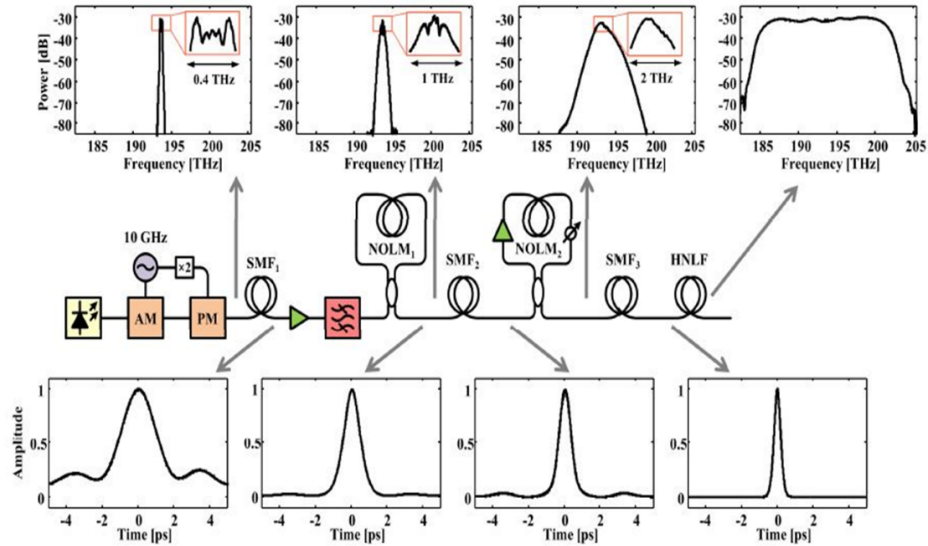


Fig. 2.2.: Experimental setup for spectral broadening employing one NOLM stage and one NALM stage. [93].

They generate an OFC electro-optically and compress the output pulse via a length of single mode fiber (SMF). This length of SMF will account for the second order dispersion, leaving residual third order on the pulse. After which, the pulse is sent to an erbium-doped fiber amplifier (EDFA) and an optical filter to remove any amplified spontaneous emission (ASE) introduced by the EDFA. The amplified pulse is launched into the NOLM, which is made up of a 2x2 power coupler, with 65 : 35 split ratio, and 60 m of specialty dispersion flattened HNLF (DF-HNLF). The pulse is cleaned up by the NOLM and then travels through another length of SMF before being launched into the NALM. The NALM is made up of a 50 : 50 2x2 power coupler, 50 m of HNLF, and an EDFA. At the output of the last DF-HNLF the 2 dB 120 nm wide spectrum is generated. In the same figure, the progression of the spectrum (top) and temporal pulse (bottom) is shown. The main takeaways should be how the pulse looks before and after the NOLM and NALM. The temporal wings or pedestals are removed after propagating through either device. The NOLM is an all-fiber way of suppressing the pedestals or wings that are a signature of third order phase. Suppressing these pedestals will lead to more effective spectral broadening. In the following section, the NOLM formulation will be presented.

2.2 Nonlinear Optical Loop Mirror Scattering Matrix Formulation

The NOLM, depicted in figure 2.3, is constructed with a 2x2 power coupler and a length of HNLF [94]. The output ports are connected together (via the length of HNLF), making the NOLM a Sagnac interferometer [95,99].

In the following section the NOLM scattering matrix formulation, presented in [18], will be outlined.

The 2x2 power coupler in the NOLM creates two counter-propagating fields in the HNLF. The counter-propagating fields will have different intensities and will therefore obtain different phases, via SPM. It needs to be noted that the intensities of the pulses need to be unbalanced. If the pulse intensities are the same, then the result will

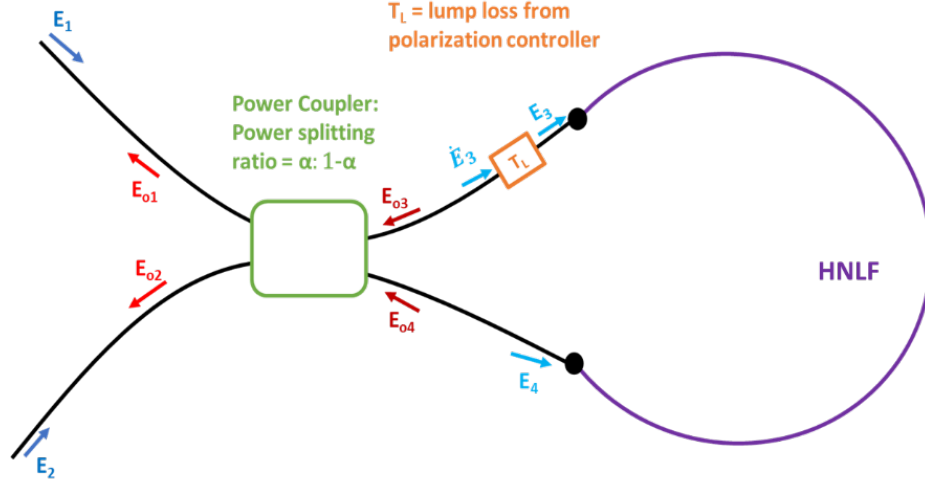


Fig. 2.3.: Cartoon depicting NOLM comprised of a 2x2 power coupler and a length of HNLF. The NOLM is a Sagnac interferometer.

be 100% reflection and, thus, the name loop mirror is appropriate. The unbalanced intensities can be generated by the power coupler, by having an amplifier in the loop (NALM), or by having some sort of lump loss in the loop. In the following scattering matrix formulation, the intensity imbalance will be introduced by a polarization controller in the loop that is needed to ensure proper interferometric interaction once the pulses come back together in the power coupler. The loss from the polarization controller will be represented as a lump loss (T_L).

$$\begin{pmatrix} \dot{E}_3 \\ E_4 \end{pmatrix} = \begin{pmatrix} \sqrt{\alpha} & j\sqrt{1-\alpha} \\ j\sqrt{1-\alpha} & -\sqrt{\alpha} \end{pmatrix} \begin{pmatrix} E_1 \\ E_2 \end{pmatrix} \quad (2.1)$$

Equation 2.1 represents the fields generated by the input field being incident on the power coupler. Note that α is the power splitting ratio and it can be thought of as $\alpha = r^2$ (where r is the reflectivity of the mirror). Also, it is important to note that E_2 is zero in these experiments, and it is enforced by having an isolator propagating light in one direction. Finally, \dot{E}_3 represents the field prior to experiencing loss from the polarization controller.

$$E_3 = \sqrt{T_L} \sqrt{\alpha} E_1 \quad (2.2)$$

Equation 2.2 represents the field after the lump loss of the polarization controller.

$$\begin{pmatrix} E_{o3} \\ E_{o4} \end{pmatrix} = \begin{pmatrix} 0 & e^{j\gamma L(1-\alpha)P} \\ e^{j\gamma L(T_L\alpha)P} & 0 \end{pmatrix} \begin{pmatrix} E_3 \\ E_4 \end{pmatrix} \quad (2.3)$$

Equation 2.3 represents the fields propagating through the HNLF. γ is the non-linearity of the fiber, and P is the optical peak power of the input field. Because of the lump loss from the polarization controller, it is evident that the phase acquired by the counter-propagating fields is different.

$$E_{o3} = \sqrt{T_L} E_4 e^{j\gamma L(1-\alpha)P} \quad (2.4)$$

Equation 2.4 represents the field going through the polarization controller and incurring its loss.

$$\begin{pmatrix} E_{o1} \\ E_{o2} \end{pmatrix} = \begin{pmatrix} \sqrt{\alpha} & j\sqrt{1-\alpha} \\ j\sqrt{1-\alpha} & -\sqrt{\alpha} \end{pmatrix} \begin{pmatrix} E_{o3} \\ E_{o4} \end{pmatrix} \quad (2.5)$$

Finally, equation 2.5 represents the fields incident upon the power coupler again. The output field that is of interest is E_{o2} . This is the output port that has the pulse with the temporal pedestals removed. Through port 1, E_{o1} , is the junk. This port will have the temporal wings that were removed from the pulse.

The transmission equation of the NOLM is given by equation 2.6.

$$T = \frac{P_{\text{out}}}{P_{\text{in}}} = \frac{|E_{o2}|^2}{|E_1|^2} = T_L [1 - 2\alpha(1-\alpha) \{1 + \cos((1-\alpha)T_L - \alpha)\phi\}] \quad (2.6)$$

The transmission equation is dependent on the power coupler splitting ratio (α), the lump loss (in our case from the polarization controller), and by ϕ , the nonlinear phase induced by SPM in the HNLF.

$$\phi = \gamma P_{\text{in}} L \quad (2.7)$$

The nonlinear phase in equation 2.7 depends on the nonlinearity of the HNLF (γ), the input peak power (P_{in}), and the length of the HNLF (L). The length and the γ are set by the parameters of the HNLF; the one variable is the input peak power. As the input power is increased, the phase difference increases from zero and the transmission also increases, reaching a first maximum when $\phi = \pi$. An example of the transmission from the NOLM is given in figure 2.4.

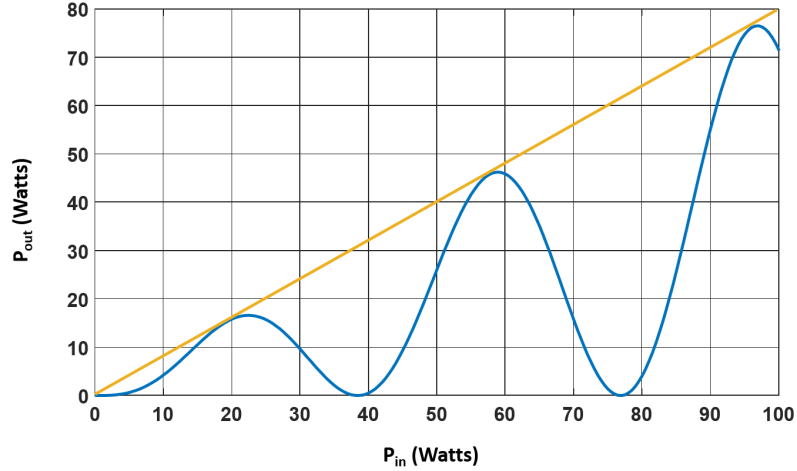


Fig. 2.4.: Plot of NOLM transmission; note the oscillatory behavior.

The transmission of the NOLM exhibits an oscillatory behavior, with multiple points where the transmission is at a maximum. For this transmission curve the length of HNLF was 147 m with a nonlinear coefficient of $10.8 \text{ (W} \cdot \text{km)}^{-1}$ with 87% transmission from the polarization controller. The transmission from the NOLM will be at a maximum when the input power is 20 W.

But where does the pulse-reshaping come into play? From reference [18], in the case that the intensity profile remains constant during propagation, the intensity and phase differences are time dependent. The consequence of this is a self-amplitude modulation (SAM) effect. SAM leads to the peak of the pulse experiencing transmission compared to the wings.

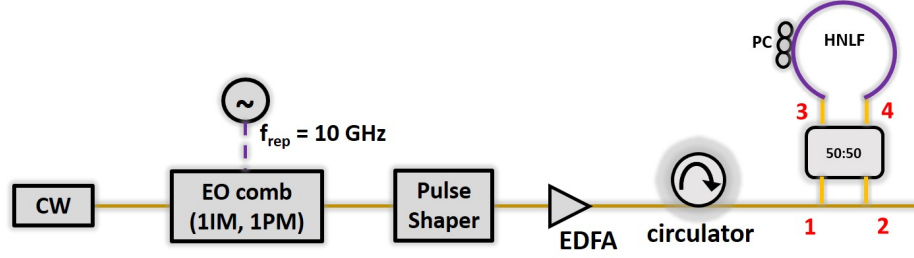
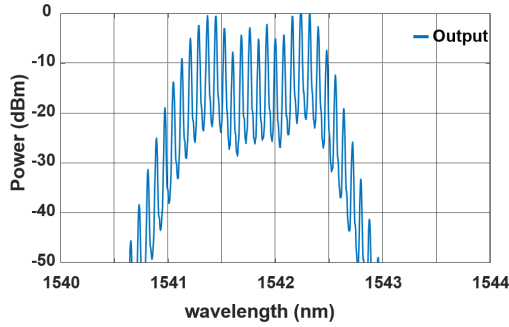


Fig. 2.5.: Experimental setup for removing residual third order wings via the NOLM.

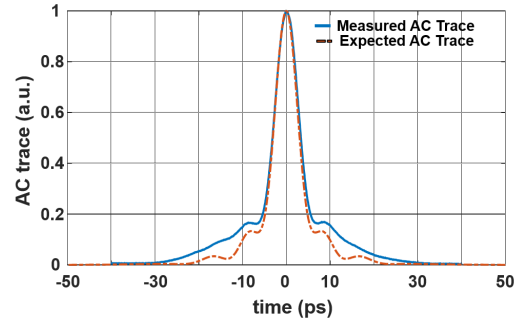
The experimental setup depicted in figure 2.5, consists of a CW laser, with center wavelength of 1542nm, used as the optical source for an EO comb generator comprised of one PM and one IM. A Fourier transform optical pulse shaper is used to compress the second order phase imparted by the PM prior to it being launched into the high-power EDFA. The pulse shaper is a commercially available device that allows for control of the phase and amplitude of spectral components [100]. The high-power amplifier is used to increase the power on the seed pulse and thereby increase transmission from the NOLM. The NOLM is made up of a 50 : 50 power coupler and 147 m of normal dispersion HNLF. The HNLF making up the NOLM has a dispersion of $D = -1.88$ ps/nm/km and a dispersion slope of $S = 0.016$ ps/nm²/km.

It should be noted that in this setup, the major contribution of noise is the EDFA. As the power is increased, more amplified spontaneous emission (ASE) is introduced, and this adds to the noise of the experimental setup. The major contribution of noise in the EO frequency comb generator is attributed to the RF oscillator used to generate the RF sinusoid that drives the electro-optic modulators [101]. The noise associated to this is low due to the quality of the RF oscillator used in the EO frequency comb generator (Agilent E8257D/67D).

The spectrum generated by the EO comb generator is shown in figure 2.6a. It generates approximately 20 lines at a rep-rate of 10 GHz. The pulse after second order dispersion compensation is shown in figure 2.6b. The full width at half maximum (FWHM) of the measured AC trace is 4.4 ps and it matches with theory. Notice the



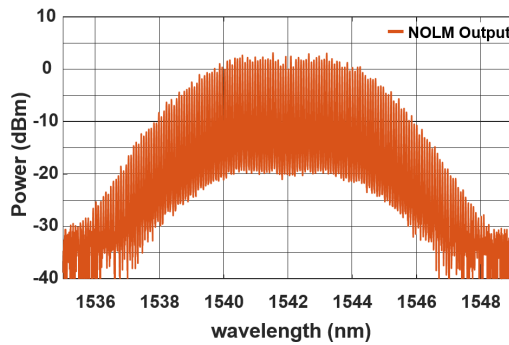
(a) Output spectrum of EO comb generator comprised of one IM and one PM.



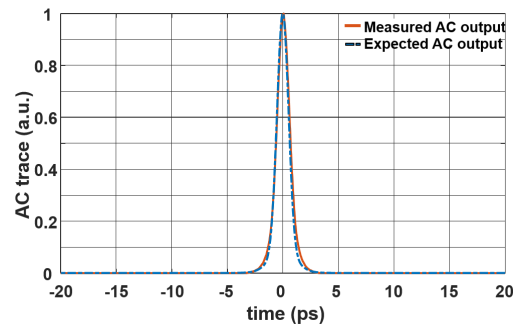
(b) Comparison of measured and expected AC trace of the compression out of EO comb generator. Only quadratic spectral phase was compensated for.

Fig. 2.6.: (a) OFC generated from 1 IM and 1 PM. (b) Comparison of AC trace of compressed pulse out of the EO comb generator. The compression is performed via a Fourier transform pulse shaper. Only linear chirp is compensated for.

pronounced third order wings on the temporal profile of the pulse. The responsibility of the NOLM will be to remove these wings.



(a) Output spectrum of NOLM



(b) Corresponding time domain trace out of the NOLM

Fig. 2.7.: (a) Spectrum out of the NOLM. (b) Corresponding time domain trace out of the NOLM; notice the removal of the third order dispersion wings.

The output of the NOLM is shown in figure 2.7a. The spectrum is slightly (8 nm wide, within 10 dB, compared to 3 nm wide at the input) broader than the input, but it shows a slightly Gaussian profile. More importantly, the temporal profile of the NOLM output no longer has the third order pedestals. The measured AC trace, shown in figure 2.7b, has a FWHM of 1 ps, and this matches with the expected AC trace. The NOLM did its job successfully.

The presented results were obtained by using one PM in the electro-optic comb generator. The question raised is, how many PMs is too much? The thought process is having more PMs will lead to a broader comb, as discussed in the comb generation section of this work, and having a broader comb to begin with may facilitate broadening in the long run. However, there is a concern as to how short of a pulse can be launched into the NOLM.

The other question that arises when analyzing the setup in figure 2.5 is, will using the pulse shaper to not only compensate for quadratic spectral phase but higher order spectral phase affect the performance of the NOLM? The pulse shaper can be used to ensure that the spectrum has a flat phase, i.e., all orders of spectral phase are compensated. Will this, along with changing the number of PMs, affect the performance of the NOLM? These are questions that were tackled with the assistance of an undergraduate researcher, Yiyun Zhang.

2.3 Simulations of Effect of Number of Phase Modulators on Nonlinear Optical Loop Mirror Performance

To answer these questions, simulations were done to determine what effect increasing the number of PMs has on the effectiveness of the NOLM. The simulations are based on the split step Fourier method (SSFM) [18,19]. In its simplest form the SSFM allows for the simulation of a pulse propagating through a fiber in which the effects of nonlinearities and dispersion can both be included. The process by which the simulation is performed is as follows:

1. The length of fiber is divided into multiple pieces of the same small length, Δz .
2. Dispersion is applied in the frequency domain.
3. An inverse Fourier transform is performed in order to switch the simulation domain into time.
4. Nonlinearities are applied.
5. Steps 2 through 4 are repeated for all lengths Δz from 0 until the entire length of the fiber is simulated.

The SSFM simulations were implemented using the open source MATLAB function `ssprop`, generated by the Photonics Research Laboratory of the University of Maryland. The user generates the seed pulse and the power associated with it. In this case the seed pulse is a simulated EO comb with either one, two, or three PMs. The function allows the user to input the length, nonlinearity, and dispersion of the fiber. The length of fiber that will be simulated is the HNLF making up the NOLM. In this case it is 147 m long. The dispersion provided by the vendor — β_2 and β_3 — are given in units of $\frac{\text{ps}^2}{\text{km}}$ and $\frac{\text{ps}^3}{\text{km}}$, respectively. The following explanation is adapted from [18]. These parameters are the Taylor expansion coefficients of the propagation constant $\beta(\omega)$. β_2 contributes a quadratic spectral phase and imparts a linear chirp on the output pulse. β_3 contributes a cubic spectral phase and an asymmetric distortion on the output pulse. For most cases, these two parameters are sufficient to describe pulse propagation in most dispersive media [18].

In the following simulations the number of PMs in the simulated EO comb generator are varied (one, two, or three). The value of phase that is compensated for prior to the NOLM is also varied. Either only the quadratic spectral phase is compensated for (arising from β_2), or all orders of spectral phase are compensated for (arising from β_2 , β_3 , and other orders of dispersion).

The first simulation performed is with 1 PM in the EO frequency comb generator, figure 2.8. The results presented here are of the output spectrum of the NOLM with

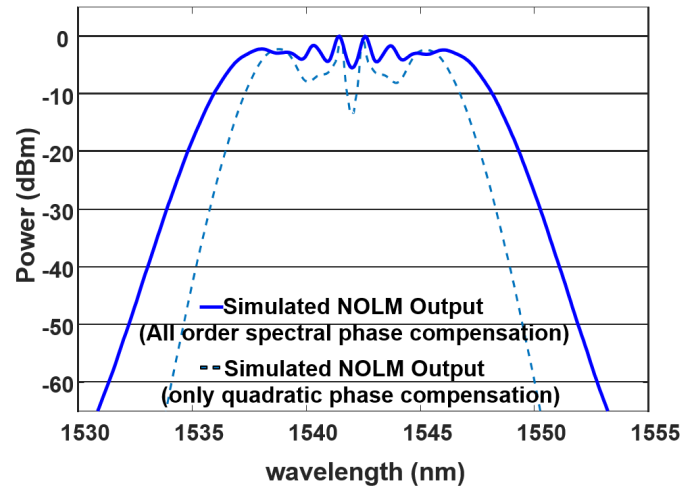


Fig. 2.8.: Simulated spectral results of one PM and one IM. The solid spectrum corresponds to compensating for all orders of spectral phase. And the dotted spectrum corresponds to compensating for only quadratic spectral phase.

all orders of spectral phase compensated for (solid) and with only quadratic phase compensated for (dashed). When the pulse shaper is only used to compensate for the quadratic phase, there is a simulated ripple of approximately 13.3 dB. When the pulse shaper is then used to compensate for all orders of spectral phase, the spectral ripple is reduced to 5.5 dB. It is important to note that this is simulated ripple.

The simulations show that adding a second PM adds to the spectral ripple, see figure 2.9. In the case when only quadratic spectral phase is compensated for, the spectral ripple out of the NOLM is 14 dB. In the case for all orders of spectral phase compensation, the spectral ripple is reduced to 7 dB.

The final configuration that was tested was the EO comb generator with 3 PMs, see figure 2.10. With only quadratic spectral phase accounted for, the spectral ripple out of the NOLM is 10.6 dB. With all orders of spectral phase accounted for, the NOLM output has 12.5 dB of spectral ripple.

The summary of simulation results is presented in figure 2.11. The main point of the simulation results is that the more PMs used in the EO comb, the worse the

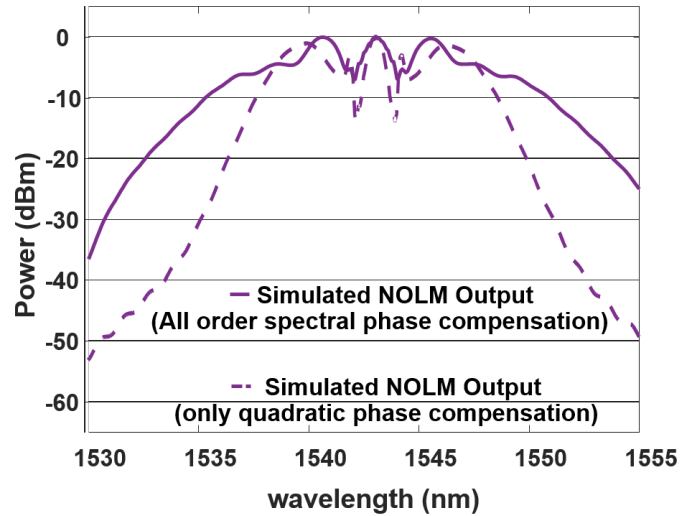


Fig. 2.9.: Simulated spectral results of two PMs and one IM. The two different spectra correspond to either compensation of all orders of spectral phase (solid) or only quadratic spectral phase compensation (dotted).

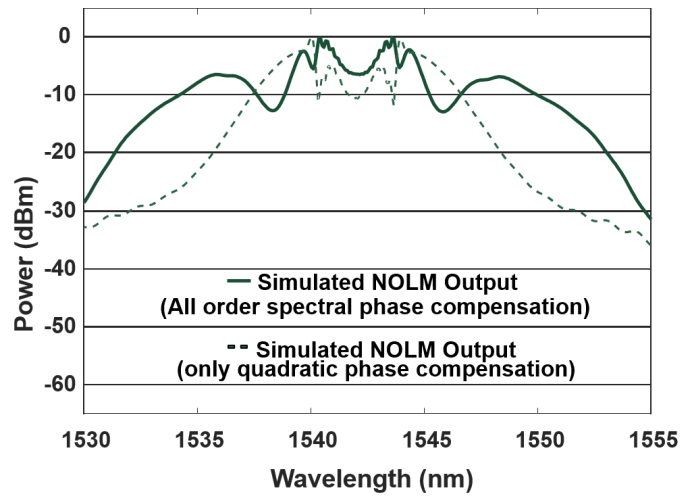


Fig. 2.10.: Simulated spectral results of three PMs and one IM. The two different spectra correspond to either compensation of all orders of spectral phase (solid) or only quadratic spectral phase compensation (dotted).

spectral ripple out of the NOLM is. There is no clear indication as to why this is.

EO COMB	Simulated NOLM Input			Simulated NOLM Output			
Use pulse shaper to compensate for only quadratic spectral phase							
	τ (ps)	P-3dB: $\Delta\lambda$	P-10dB: $\Delta\lambda$	τ (ps)	P-3dB: $\Delta\lambda$	P-10dB: $\Delta\lambda$	Spectral Ripple
1 PM	4.78	2 nm	2 nm	0.68	10 nm	12 nm	13.3 dB
2 PM	2.91	3 nm	4 nm	0.56	12 nm	14 nm	14.0 dB
3 PM	2.11	4 nm	4 nm	0.53	10 nm	12 nm	10.6 dB
Use pulse shaper to compensate all orders of spectral phase							
	τ (ps)	P-3dB: $\Delta\lambda$	P-10dB: $\Delta\lambda$	τ (ps)	P-3dB: $\Delta\lambda$	P-10dB: $\Delta\lambda$	Spectral Ripple
1 PM	4.10	2 nm	2 nm	0.55	12 nm	14 nm	5.5 dB
2 PM	2.20	2 nm	3 nm	0.40	16 nm	21 nm	7.0 dB
3 PM	1.44	4 nm	4 nm	0.35	16 nm	22 nm	12.5 dB

Fig. 2.11.: Summary of simulation results. The lowest spectral ripple is from using only one PM. However, two PMs seems like a good compromise for low ripple and broad spectrum.

The two fiber parameters of the HNLF in the NOLM used in the simulations are dispersion and nonlinearity, and they remain the same for every simulation.

However, it is clear that using one or two PMs still meets the goal of this work. To reiterate, the goal is to achieve a broadened spectrum with spectral ripple less than 10 dB. Therefore, in the next section, an EO comb generator with two PMs and a NOLM will be used to characterize single-soliton Kerr combs generated in silicon nitride microring resonators.

Acknowledgement of Collaboration

The work on the construction and characterization of the NOLM was performed by the author of the document. The simulations were a collaboration between the author and an undergraduate researcher, Yiyun Zhang.

3. CHARACTERIZATION OF SINGLE-SOLITON KERR COMBS VIA DUAL COMB ELECTRIC FIELD CROSS-CORRELATION

In the previous chapter, it was shown that the NOLM can be used to remove third order dispersion wings associated with spectral ripple formation. In this chapter, the NOLM will be employed to generate a frequency comb with spectral ripple less than 10 dB and with a bandwidth of 40 nm. This comb will be used to retrieve the phase of a single-soliton Kerr comb generated in an anomalous dispersion silicon nitride microresonator. The phase is retrieved via dual comb interferometry via electric-field cross-correlation. The single-soliton Kerr comb is sampled via the drop-port of the silicon nitride microresonator, allowing for access to a direct replica of the intracavity pump field. The single-soliton Kerr comb inherently offers high repetition-rates and low power. This makes it difficult and time consuming to characterize the pulse via typical measurement techniques that require high pulse energies due to the measurements relying on optical nonlinearities. The dual comb interferometry technique presented in this chapter is an all-linear method allowing for rapid (μs) phase retrieval of a low power ($20 \mu\text{W}$) soliton Kerr comb. The measurement technique relies on the spectral broadening of an EO comb and the pre-characterization of its spectral phase. The methods for performing these tasks are presented in this chapter. First, an explanation of soliton formation in microresonators is presented, as well as an explanation of the measurement technique. The results presented in this chapter have been adapted from the various publications this work has appeared in [102, 103].

3.1 Achieving Mode-Locking in Microresonators

There exist two routes to frequency comb generation [57, 59, 104]. The combs generated by these two different routes are differentiated by either type I or type II classification.

The type I comb is characterized by being less noisy during the generation process and offers coherent comb generation. Its counterpart, the type II comb, is noisier during the generation process and suffers from degraded coherence. This reduced coherence is attributed to the imperfect frequency division process of the non-degenerate FWM involved in the comb generation. However, this does not mean that type II combs are of no value. In the following section, the generation of mode-locked pulses (solitons) from these type II combs will be discussed.

3.1.1 Bright soliton formation in anomalous dispersion microresonators

Studies have been performed on generating short coherent pulses in microresonators from type I and type II combs, [57], in both normal [54], and anomalous [105, 106] dispersion cavities. In anomalous dispersion cavities, several works have shown the possibility of passively mode-locked combs analogous to soliton formation [105–110]. Solitons in optical fibers in the anomalous dispersion regime are pulses that can propagate without distortion under the joint effect of nonlinearity and dispersion [18]. The solitons formed inside the microresonator cavities are known as dissipative solitons, due to their reliance on the Kerr effect and the continual out-coupling. These are formed from the balance of cavity dispersion and nonlinearity, and input power and cavity loss. This balance leads to a broad bandwidth and low-noise comb operation [111]. It is important to note that these mode-locked like pulses are generated from the chaotic type II comb. Soliton formation has been theoretically presented via simulations employing the standard Lugiato-Lefever model [112]. Solitons are one of many possible solutions to the Lugiato-Lefever equation.

The first demonstration of solitons in anomalous dispersion microresonators was published in 2014 [106]. In this work, correlations between the mode-locked generation and the transmission spectra and response of comb power were presented, see figure 3.1.

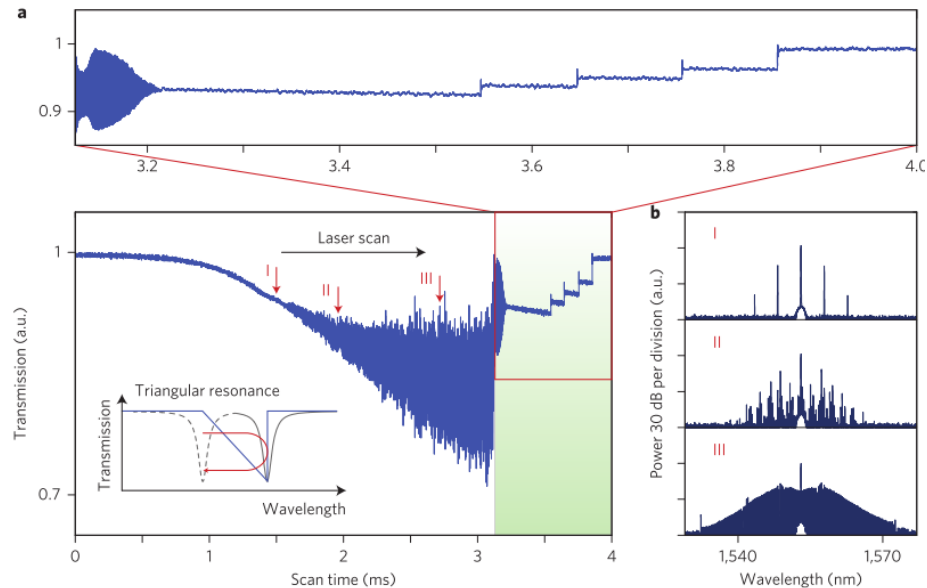


Fig. 3.1.: The signature of soliton generation. The transitions from a noisy chaotic state to N solitons. Further red detuning eventually leads to the single soliton regime [106].

As the wavelength of the pump is tuned from blue to red, more light is coupled into the cavity, and there is an increase in intra-cavity power. This increase in power leads to a modification of the refractive index in the resonator, which then leads to modification of the cavity resonance. This modified resonance has a high and low energy state, the high energy state being the state that produces soliton formation. With this increasing power, primary sidebands and then secondary sidebands are generated via the cascaded FWM process. Continuing to increase the intra-cavity power leads to an important occurrence, an abrupt jump to a minimal fluctuations state in the optical power. Further pushing the pump detuning to the red causes the cavity to step through further drops in the intra-cavity power. These steps are the

signatures of the transition from N-soliton states to the next N-1 soliton state until, eventually, reaching the single soliton state.

3.1.2 Pump line phase offset of single soliton Kerr comb

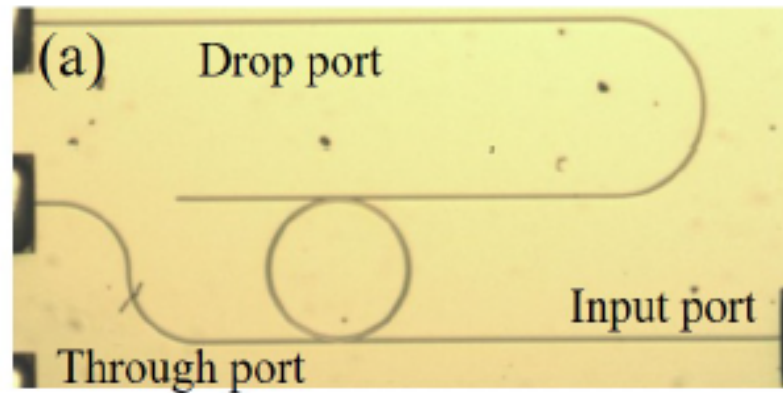


Fig. 3.2.: Microscopic image of microresonator with through and drop ports.

In reference [111], the time domain characteristics of single soliton Kerr frequency comb were studied. These studies were based on second harmonic generation (SHG) intensity autocorrelation, employing a microring resonator with drop-port geometry, shown in figure 3.2.

Figure 3.3a shows the soliton spectrum after an EDFA. The spectrum of the soliton is broader, but due to the limited bandwidth of the EDFA, only part of the spectrum is analyzed. Figure 3.3b shows the measured AC trace (blue) and the simulated AC trace (red). These measurements are in good agreement. This soliton measurement is consistent with previous measurements in crystalline microresonators [106,113] and integrated photonics based microresonators [105,108].

The phase relationship between the pump line and the generated comb is the main topic of interest in this work. The phase of the pump line exhibits an offset, and this has been shown theoretically [114]. But for the first time ever, the pump phase offset inside the microring cavity in the single soliton regime was measured [111].

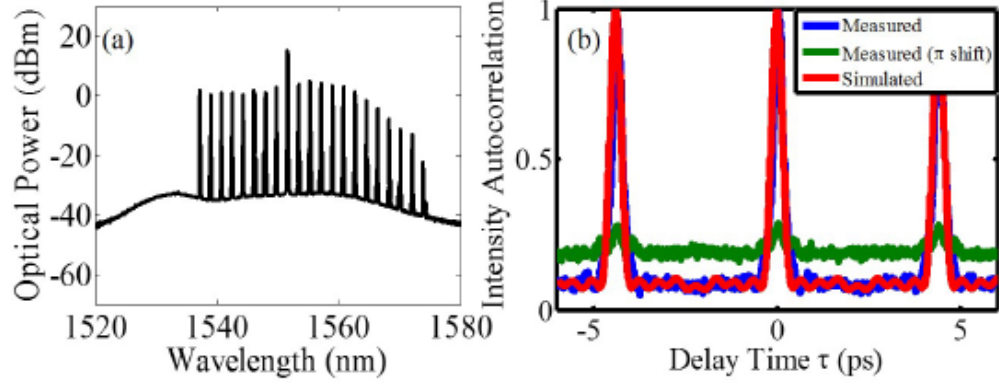


Fig. 3.3.: (a) Optical spectra after EDFA and pulse shaper for pump wavelength of 1551.27nm (b) Autocorrelation data (blue) and simulation (red) based on measured spectrum assuming flat phase. Autocorrelation data with π phase shift applied to the pump (green).

By applying a π phase shift on the pump line and analyzing the retrieved autocorrelation trace, the relationship of the pump line to its neighboring comb lines was established. The π phase shift significantly degrades the autocorrelation (green trace). This degradation reveals that the pump line is largely out of phase with the rest of the comb after applying the π phase shift, thus revealing that the spectral phase of the pump line is close to the generated comb, even though the pump line is more intense than the adjacent lines.

By employing a drop-port geometry, several advantages are obtained when compared to the through-port geometry. These include direct analysis of the intra-cavity field, increase in optical signal to noise ratio of the spectrum, a smoother spectrum, and a less intense pump line (45 dB for through port, and 15 dB for drop port) [105, 106, 108, 113]. And finally, for the first time, the pump-line phase offset is measured to be approximately 0.42 radians in the single soliton regime.

3.2 Dual Comb Electric Field Cross-Correlation Measurement for Study on Pump Line Phase Offset in Soliton Kerr Combs

As was detailed in the previous section, the pump line phase offset was demonstrated experimentally via intensity SHG autocorrelation [111]. This measurement corroborated the theoretical model that predicted this phase offset [114].

These measurements provide the basis for a new method. The SHG pump phase offset measurements, although informative, were difficult to implement. This is because conventional methods of characterizing the phase profile of ultrafast pulses often rely on optical nonlinearity and thus, these methods usually apply to optical waveforms that have relatively high peak power and low duty cycle. In the case of Kerr combs, or solitons generated in microresonators, these waveforms are often characterized by low average power and very high repetition-rates, making them difficult to be characterized via conventional methods. A new method for characterizing the phase profile of low average power and high repetition-rate waveforms is presented [102,103]. This new method allows for all linear phase retrieval of Kerr solitons through a technique called dual comb electric field cross-correlation (EFXC), which reduces the demand on signal power and offers rapid data acquisition. The first iteration of this new technique was used to characterize the phase profile of Kerr solitons, and was demonstrated at CLEO 2018 [102]. After fine tuning the setup and paying closer attention to the noise associated with the measurement technique, the second iteration was published in reference [103] and is the focus of this chapter. This new measurement technique is closely related to the dual comb EFXC demonstrated in [70] for the characterization of optical arbitrary waveforms.

3.2.1 Dual comb interferometry via electric field cross-correlation

The dual comb EFXC technique allows for the independent sweeping of phase and group delays without any mechanical stages. Spectral phase can be retrieved from

the data acquired in tens of microseconds [70]. This method is related to absorption measurements in [73], and in linear optical sampling in [61].

The following introduction to EFXC was adopted from [18, 70]. EFXC measures the interference between two fields: a signal field a_s , the field that is to be measured, and a reference field a_r . These fields are interfered in the time domain as a function of relative delay, τ . Traditionally, the delay is swept using a mechanical stage.

$$\langle P_o(\tau) \rangle = \frac{1}{2} \left[U_s + U_r + \int \{ a_s(t) a_r^*(t - \tau) e^{j\omega_o\tau} + c.c. \} dt \right] \quad (3.1)$$

Equation 3.1 is the expression for the resulting time-average power obtained at the output of a slow photo-detector as a function of delay [18]. In this expression, U_s and U_r are the pulse energies, and ω_o is the carrier frequency. The point to emphasize is that an unknown signal pulse can be fully recovered from a known and well-characterized reference pulse [70].

In the dual comb EFXC scheme, two frequency combs with a difference in repetition rate, Δf_{rep} , are used. This Δf_{rep} causes the two pulses to walk through each other in time $\frac{1}{\Delta f_{\text{rep}}}$. By controlling the difference in rep-rate, the group-delay sweep can be controlled. To control the phase-delay sweep, the difference in center frequencies, Δf_{center} , can also be swept, thus being able to control the group and phase-delay independently.

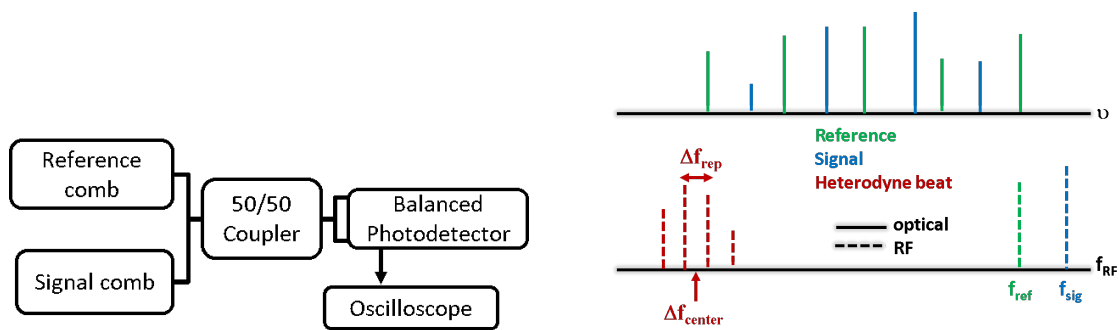
In the spectral domain, the conventional EFXC time average power can be retrieved by performing a Fourier transform on equation 3.1.

$$F[\langle P_o(\tau) \rangle] = \dots + \frac{1}{2} \{ A_s(\omega - \omega_o) A_r^*(\omega - \omega_o) + A_s^*(-\omega - \omega_o) A_r(-\omega - \omega_o) \} \quad (3.2)$$

In equation 3.2, the non-interferometric terms are omitted. In this implementation the first and second terms inside the brackets correspond to $+\Delta f_{\text{center}}$ and $-\Delta f_{\text{center}}$, respectively. In the analysis, only the $+\Delta f_{\text{center}}$ is considered. This corresponds to a series of RF comb lines that are separated by Δf_{rep} . These discrete lines, referred to as the RF comb from now on, demonstrate the preservation of phase coherence.

From this RF comb, the phase of the signal comb can be retrieved. To do so, the reference comb must be pre-characterized. In this work, a pulse shaper is used to phase compensate individual frequency components [23] and thus obtain a transform limited pulse, i.e., flat spectral phase. The RF comb is retrieved by performing a Fourier transform on the photo-detected signal. The phase is then extracted by performing post processing.

Particulars of the dual comb interferometry measurements



(a) Generalized setup for dual comb EFXC measurement.

(b) (top) Beating of two combs in the optical domain, (bottom) leading to an RF comb after photo-detection. There is a mirrored version of the RF comb that is omitted for simplicity.

Fig. 3.4.: Cartoons depicting the (a) setup and (b) spectra of the dual comb EFXC.

The generalized experimental setup for the dual comb EFXC measurements is shown in figure 3.4a. The reference and signal combs are interfered in a 50 : 50 coupler and then detected by a balanced photo-detector (BPD). The signal out of the BPD is detected in an oscilloscope, and post processing allows for the retrieval of the phase of the signal comb. In these experiments, the reference comb is an EO comb spectrally broadened with the aid of a nonlinear optical loop mirror (NOLM). The reference comb is characterized via line-by-line pulse shaping, analogous to [57].

Figure 3.4b depicts the optical to RF mapping of the dual comb EFXC technique. This figure is analogous to figure 1.6a, except in this measurement there is no absorption as spectroscopy is not the goal of this work, waveform reconstruction is. The signal comb (blue), with rep-rate f_{sig} , is beat with a reference comb (green) having a rep-rate of f_{ref} . The beating occurs in the 50 : 50 coupler, and this beating is mapped onto the RF domain. This RF comb is separated by Δf_{rep} , the difference in rep-rate between the two combs.

$$I_{\text{RF}} \propto E_{\text{sig}} E_{\text{ref}} \cos [(\omega_{\text{sig}} - \omega_{\text{ref}}) t + \varphi_{\text{sig}} - \varphi_{\text{ref}}] \quad (3.3)$$

The current, for one particular set of reference and signal comb lines, out of the BPD is expressed in equation 3.3. ω_{sig} and ω_{ref} correspond to the angular frequency of the signal and reference comb line, respectively. One important note that is not pictured in figure 3.4b is that the difference in carrier frequencies, Δf_{center} , of the two combs determines where in the RF domain the RF comb is mapped to.

$$\varphi_{\text{RF}} = \varphi_{\text{sig}} - \varphi_{\text{ref}} \quad (3.4)$$

The phase of the RF comb is expressed in equation 3.4, and it is the difference between the signal phase and reference phase. By characterizing the reference comb to have flat spectral phase i.e., $\varphi_{\text{ref}} = 0$, the RF phase is then simply $\varphi_{\text{RF}} = \varphi_{\text{sig}}$. This allows the phase of the signal comb to be reconstructed by finding the phase of the RF comb.

3.2.2 Signal comb - single-soliton Kerr comb sampled through drop port of silicon nitride microresonator

The signal comb is a Kerr soliton generated from a silicon nitride microresonator (radius 100 μm and loaded-Q 2.4 million), depicted in figure 3.5. The ring resonator employs drop-port geometry, allowing for the direct sampling of the intra-cavity field and avoids interference from the strong pump line [111]. The spectrum has a secant

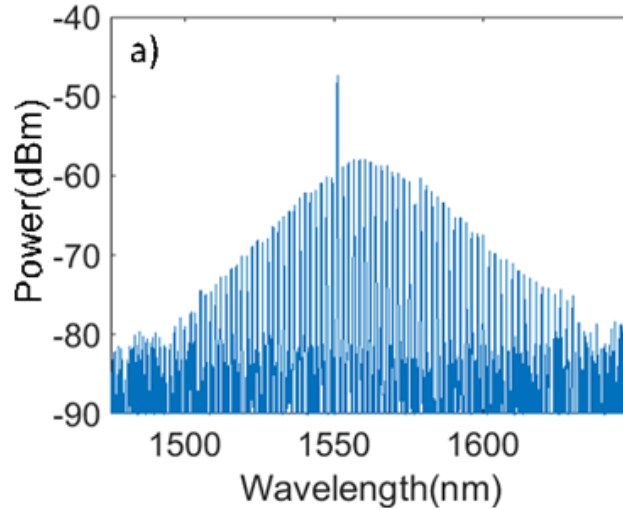


Fig. 3.5.: Single soliton generated in SiN microring resonator depicted in figure 3.2. This spectrum is taken from the drop port. Note the slight offset of the pump line arising from Raman interactions. The free spectral range (FSR) is 227.5 GHz.

hyperbolic shape, indicative of the presence of a soliton. Note the pump line is slightly offset from the center of the spectrum; this is predicted by theory and attributed to Raman interactions. The repetition rate of the Kerr soliton, referred to as the signal comb from now on, is 227.5 GHz. By ensuring that the coupling between the drop port and the ring resonator is low, this prevents degradation of the Q inside the cavity. However, this also lowers the output power, and in this case, it is 20 μW .

3.2.3 Reference comb - spectrally broadened electro-optic frequency comb

The reference pulse setup for the second iteration of measurements is shown in figure 3.6.

A tunable laser source (TLS) is used, offering freedom to change the center wavelength of the EO comb. An erbium doped fiber amplifier (EDFA) is used to pre-amplify the CW laser. In this iteration of experiments, the number of phase modulators in the EO comb generator was increased to two. A pulse shaper is used to

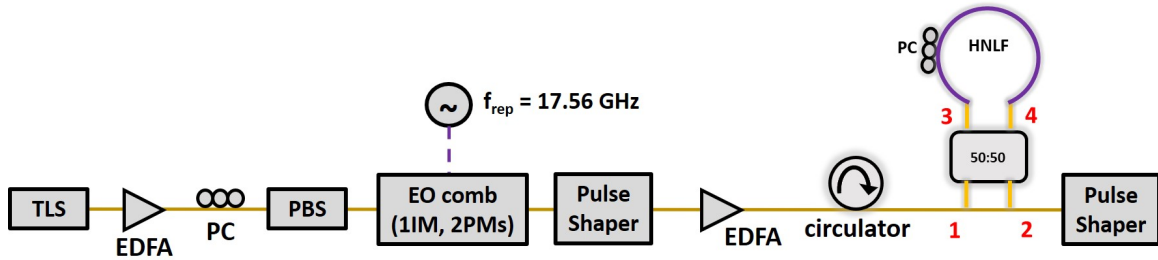


Fig. 3.6.: Experimental setup for spectrally broadening electro-optic frequency comb for use as reference comb in the dual comb interferometry measurements.

compress the output of the EO comb generator i.e. compensate spectral phase so as to achieve a band-width limited pulse. However, in this case the pulse shaper was used to shape the output spectrum of the generator and to perform line-by-line phase compensation [57]. The pulse was amplified via a second EDFA and then launched into the NOLM (the same NOLM presented in chapter 2). Because the first pulse shaper was used to apodize the waveform and to perform all-order phase control, and the second EDFA has more than sufficient amplification, the NOLM itself generated sufficient broadening to fill the working bandwidth of the second pulse shaper - normally 40 nm. The NOLM in this case can be thought of as a broadening stage that reduces the spectral ripple. If only a length of HNLF was used, the spectral ripple would be worse. Finally, a second pulse shaper is used to prepare the reference pulse for the dual comb EFXC measurements.

Figure 3.7 shows the output of the EO comb generator. The number of lines has doubled when compared to the previous iteration, due to doubling the number of PMs. Note the rabbit ears on the spectrum. These ears are due to the deviation from quadratic phase, imparted by the PM, at the edges of the spectrum. Removing these ears reduces the demand on the NOLM, and thus more broadening occurs. This is analogous to shaping the comb to have a Gaussian profile prior to broadening in

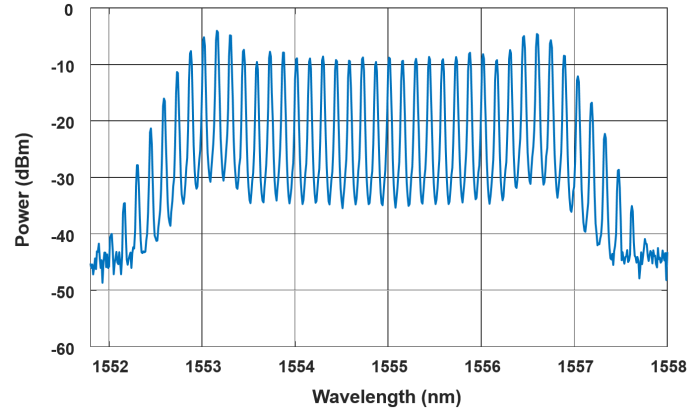
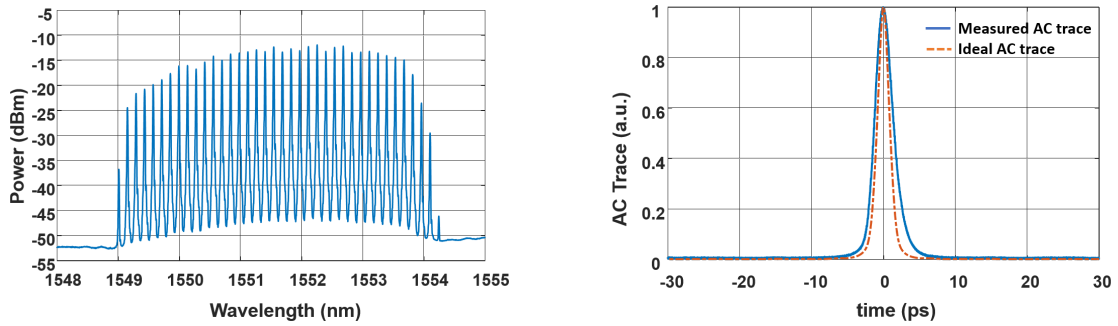


Fig. 3.7.: Spectrum of electro-optic frequency comb generated from two phase modulators and one intensity modulator.

order to take advantage of optical wave breaking, see chapter 1. The spectrum after apodization is shown in figure 3.8a.



(a) Apodized electro-optic frequency comb spectrum. Notice removal of rabbit ears.

(b) Comparison of measured and expected AC trace of compressed pulse out of the EO comb. All orders of spectral phase were compensated for in the pulse compression.

Fig. 3.8.: Apodized EO comb and corresponding compressed AC trace.

The first pulse shaper is used to perform line-by-line pulse compression, the same method that is used to characterize the reference pulse prior to the dual comb EFXC measurement. Figure 3.8b shows the pulse after the pulse compression procedure.

After compression, the measured AC trace is close to the ideal AC trace. Note that the ideal AC trace is obtained by performing a Fourier transform on the spectrum out of the NOLM, assuming a flat phase, and convolving this result with itself. Notice that at this point there isn't any third order phase pedestals. Therefore, the demand on the NOLM will be reduced and this translates to more broadening. The AC trace has a FWHM of approximately 2 ps.

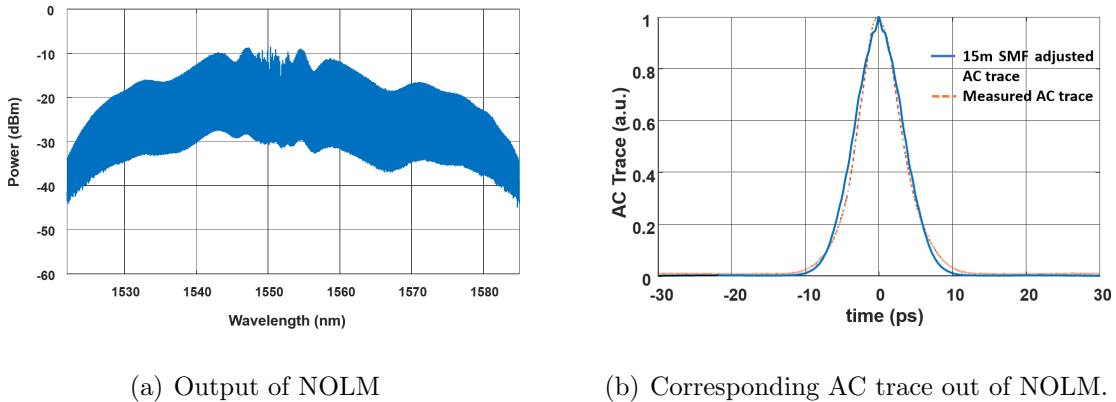
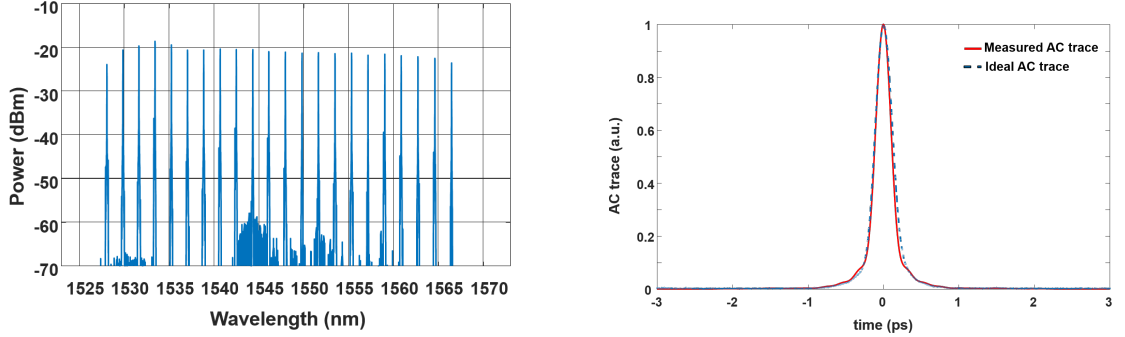


Fig. 3.9.: The output of the nonlinear optical loop mirror.

Figure 3.9a shows the spectrum out of the NOLM. Because of the effectiveness of the apodization and line-by-line pulse compression prior to the NOLM, the output spectrum of the NOLM is wide enough to fill the bandwidth of the pulse shaper (last pulse shaper in figure 3.6) used in characterizing the reference pulse for the dual comb EFXC measurements. Figure 3.9b shows the measured AC trace. It is important to note that to obtain this measured AC trace, the output of the NOLM propagates through 15 m of SMF. This length of fiber is enough to temporally broaden the pulse. To confirm that this is the case, the spectral phase imparted by 15 m of SMF was simulated onto the NOLM spectrum. Then this was compared to the measured AC trace. If this is the reason why the pulse is broader, then the measured AC trace and this new adjusted AC trace will match. Figure 3.9b shows the adjusted AC trace matches with the measured AC trace. This pulse is now sent into the second pulse

shaper to characterize the reference pulse for dual comb EFXC measurements. The ideal AC trace has a FWHM of approximately 200 fs.



(a) Filtered reference spectrum. Only every 13th line interacts with the signal.

(b) Comparison of measured and expected AC trace of reference pulse. All orders of spectral phase were compensated for in the pulse compression.

Fig. 3.10.: The reference pulse used in the dual comb interferometry measurements.

$$f_{\text{sig}} = 13 \times f_{\text{ref}} + \Delta f_{\text{rep}} \quad (3.5)$$

Before generating the transform limited reference pulse in this iteration of the measurement, the spectral lines that will not interact with the spectral lines of the signal are filtered out. From equation 3.5, every 13th line from the EO comb interacts with a line from the signal comb. By removing the reference lines that don't interact with the signal, this will reduce the noise in the setup and raise the signal-to-noise ratio of the measurement. This makes the $f_{\text{ref}} = 227.5$ GHz and thus equal to f_{sig} . Note that $\Delta f_{\text{rep}} = 160$ MHz for these measurements. The spectrum after filtering is shown in figure 3.10a. The line-by-line procedure was performed on the output of the NOLM. The line-by-line phase compensation returned a close to bandwidth limited pulse as is shown in figure 3.10b. The measured AC trace is close to the ideal case. This then, is the reference pulse that is used in the dual comb EFXC measurements. The duration of the measured AC trace is approximately 240 fs.

3.2.4 Retrieving phase of single-soliton Kerr comb via dual comb interferometry

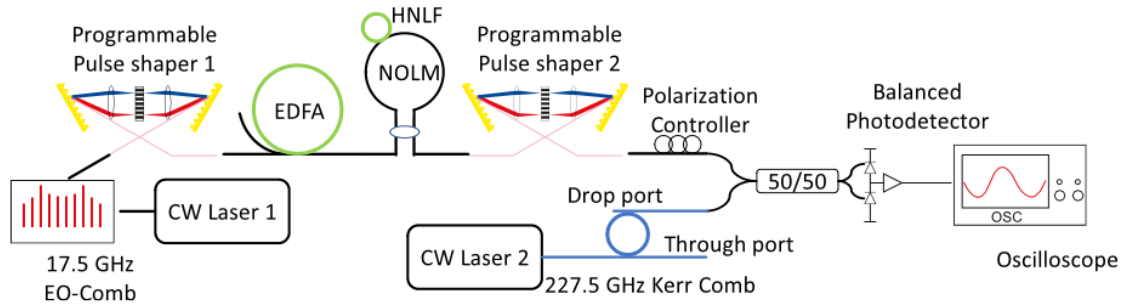


Fig. 3.11.: The experimental setup for performing dual comb interferometry for characterization of single-soliton Kerr-comb [103].

The experimental setup for performing the dual comb interferometry measurement (dual comb EFXC) is depicted in figure 3.11 [103]. The dual comb interferometry is performed with signal comb power of $20 \mu\text{W}$ and a reference comb power of 1 mW . The resulting interferogram is detected with a balanced photo detector with 20 GHz bandwidth and it is recorded with a digital serial analyzer with 20 GHz analog bandwidth and 12.5 Gs/s sampling rate. The 20 ns sample of the interferogram is shown in figure 3.12a [103]. Due to the dispersion of the 7.5 m of fiber needed to send the Kerr comb from the output of the drop port to the $50 : 50$ coupler, depicted in figure 3.11, the soliton contributions broaden and blend due to the dispersion and are not clearly visible. However, this dispersion effect does not prevent an RF comb from being visualized. By performing a Fourier transform on the entire $3.2 \mu\text{s}$ duration interferogram the RF comb's power spectrum is shown in figure 3.12c. The RF comb power spectrum shows 23 lines, which corresponds to an optical bandwidth of 5 THz ,

limited to the passband of the second pulse shaper used in the compression of the broadened reference comb. The RF comb line corresponding to the pump line of the Kerr comb has an SNR exceeding 40 dB, while the other lines have SNRs ranging between 17 and 30 dB.

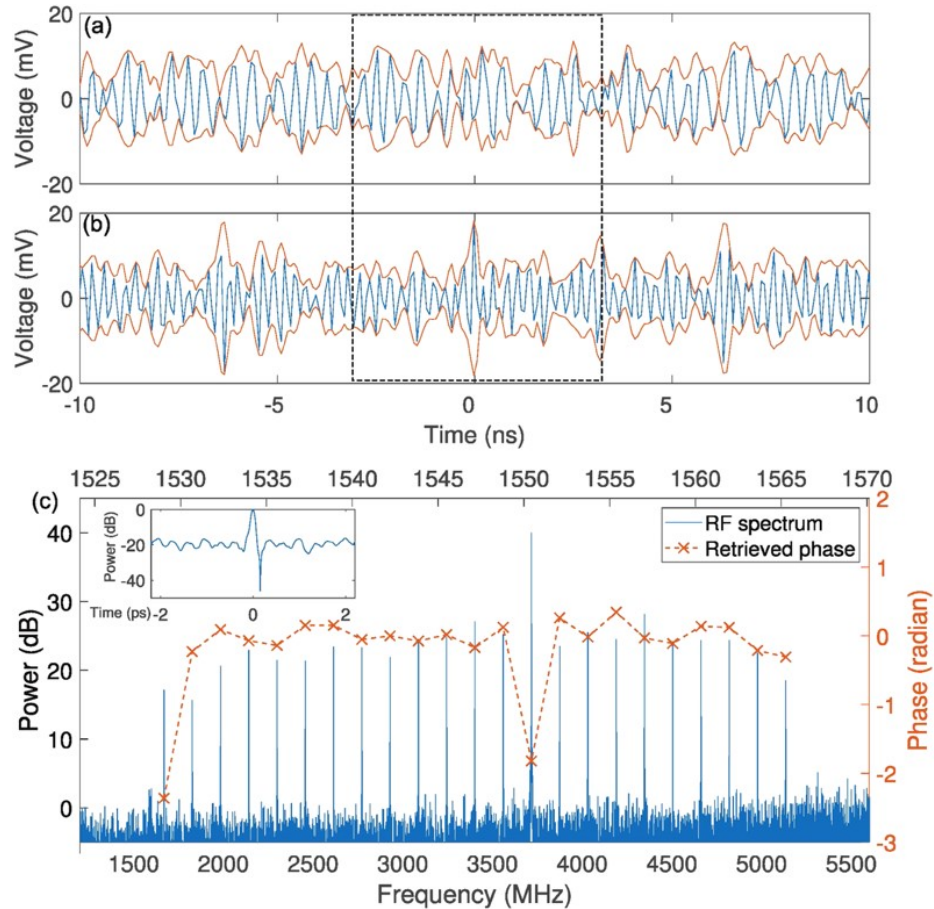


Fig. 3.12.: (a) A portion of the measured time domain interferogram. (b) The reconstructed interferogram after compensating for fiber dispersion. The dashed box in (a) and (b) represent one period of the interferogram and the orange lines are the envelope of the interferogram. (c) The blue trace is the power spectrum of the interferogram. The orange trace is the retrieved phase of the different optical modes. The pump line exhibits a phase offset. The inset in (c) is the reconstructed intracavity waveform using the retrieved comb phase [103].

By subtracting the phase corresponding to the fiber and performing an inverse Fourier transform, the “corrected” interferogram is shown in 3.12b. Now the soliton-like peaks begin to appear. In figure 3.12b, the envelopes are shown and were obtained via Hilbert transform.

The relatively large background arises due to the truncation of the spectrum of the reference comb. An SNR of approximately 4 is estimated from the variations of the envelope across different periods for the interferogram in figure 3.12b. This value is consistent with the ratio of the power in the comb lines of figure 3.12c to the integrated noise power. Also, due to the beat and repetition frequencies not being integer multiples, the interferogram itself varies.

In figure 3.12c, the spectral phase is plotted alongside the power spectrum of the RF comb, after the dispersion correction. The phase of the pump line is shifted by approximately -1.8 rad with respect to the other lines whose phase is approximately flat (within ± 0.19 rad). In the time domain, the soliton has a positive phase shift with respect to the background; this is consistent with theory [106,115]. The 1528 nm comb line (shortest wavelength in our measurement) also exhibits a phase shift. The explanation for this phenomena may be attributed to perturbations from the mode interaction [116,117].

Having this phase information, we can reconstruct time domain profile of the soliton. The inset of figure 3.12c shows the reconstructed time domain profile of the soliton. To perform the reconstruction, it was assumed that the comb line outside of the pulse shaper 2 passband have zero phase and follow a sech^2 fit. The pump line phase shift can be related to the dip at the tail of the pulse. For the interested reader, reference [103] addresses this phenomena using LLE simulations.

The results presented in this section demonstrate that the all-linear dual comb interferometry allows for characterization of the soliton Kerr comb at low powers with a high acquisition speed that clearly reveals the phase shift of the soliton with respect to the pump line.

3.2.5 Study on pump line phase offset of single-soliton Kerr comb

Due to the rapid nature of the measurement, it allows for the study of the dependence of the pump phase offset on pumping conditions. Measurements of the pump line phase offset are of interest as they will allow for understanding the time domain characteristics of the single-soliton Kerr comb. The inset in figure 3.12c, shows the reconstructed time profile of the single-soliton in the cavity. Note that there is a background level of -20 dB (or approximately 1 %). The intracavity field can be thought of as a superposition of two components; a CW background resulting from pump light being continually coupled into the cavity and the soliton state [106]. This is different than the soliton in optical fiber, in that the time domain profile of the fiber soliton does not have this CW background [18]. Performing the study on the pump line phase offset allows for better understanding of the time domain profile of the cavity soliton under different pumping conditions.

By averaging the retrieved phase of 100 independently captured interferograms, the pump phase offset at a given pumping condition can be measured. The measurement results are shown in figure 3.13 for on-chip pump powers of 350 and 400 mW for the full range of wavelengths at which a stable single soliton can be generated. The error bars are 0.08 rad and are taken from the standard deviation among retrieved phase with linear and constant terms removed.

When the pump power is fixed at 400 mW, the phase offset is observed to change from -1.8 rad to -1.2 rad as the pump wavelength is increased. The magnitude of the pump phase offset is larger as the pump power is increased. From the power spectrum of the Kerr comb and the data of the pump phase offset study, the time domain behavior can be estimated.

By using the power spectra and the pump phase offsets, the behavior of the soliton in the time domain can be estimated. The ratio of the soliton peak power to the background increases from 100 at small detuning by a factor of two as the detuning is increased. The soliton phase with respect to the background is positive

and the magnitude of the soliton phase offset with respect to the background shows trends similar to that of figure 3.13. In this case the magnitude of the soliton phase offset decreases as the detuning increases. All these trends are consistent with the approximate analytical solution presented in [106, 115].

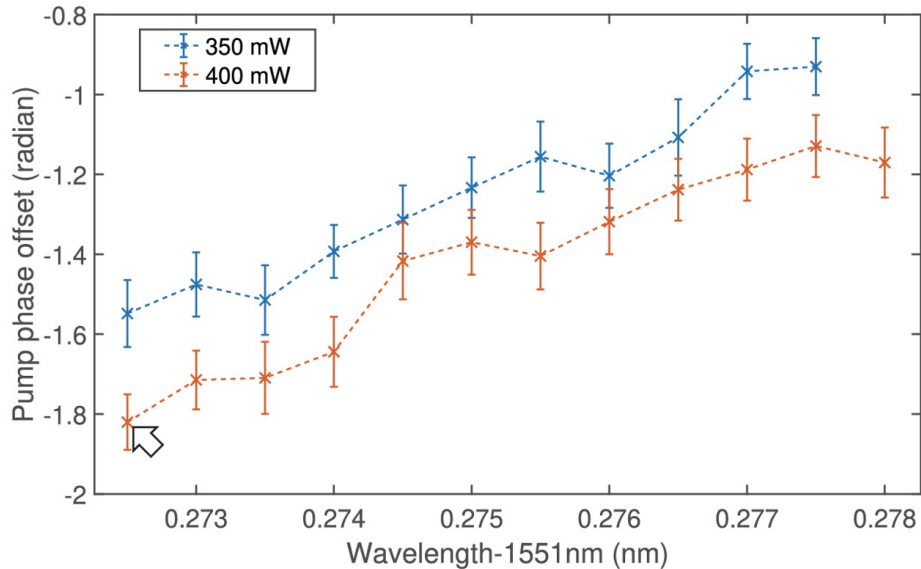


Fig. 3.13.: Results of pump line phase offset study with increasing pump wavelength. The data point indicated by the arrow corresponds to the data presented in figure 3.12c.

For the first time, a study on the pump-line phase offset as a function of both wavelength and power is presented. This study advances fundamental understanding of single solitons in Kerr combs. By using the dual comb EFXC method employed in [102], the pump-line phase offset study was performed with low power needed from the signal comb. It was found that the pump line has a negative phase offset with respect to the rest of the spectrum. This phase offset becomes more negative as the pump power increases or as the pump detuning is decreased.

In this chapter, the electro-optic frequency comb broadened via the aid of a non-linear optical loop mirror was used to retrieve the phase of a single-soliton Kerr comb. The phase was retrieved via dual comb interferometry that required the

pre-characterization of the phase of the spectrally broadened electro-optic frequency comb. The broadening and pre-characterization techniques were presented. The results of the dual comb interferometry measurements show that the pump line has a negative phase offset with respect to the rest of the spectrum that becomes more negative as the pump power is increased or pump-detuning is decreased. This measurement technique allows for the rapid characterization of waveforms with high repetition rates and low power.

Acknowledgement of Collaboration

The author was tasked with providing and characterizing the broadened reference comb. Bohao Liu was responsible for the preparation of the reference pulse i.e., ensuring a flat spectral phase. Ziyun Kong and Chengying Bao are the leads of the project and their responsibility was the oversight of the collaboration. Specifically, Ziyun was tasked with the retrieval of the phase and pumpline phase offset, and Chengying generated the single soliton for the work presented in [102]. Jose Jaramillo and Cong Wang were responsible for the generation of the single soliton in the pumpline phase offset study.

4. POLARIZATION DIVERSITY PHASE MODULATOR FOR MEASURING FREQUENCY-BIN ENTANGLEMENT OF BI-PHOTON FREQUENCY COMBS IN A DEPOLARIZED CHANNEL

In this chapter the polarization diversity phase modulator (PDPM) is introduced. This device allows for phase modulation to be performed, irrespective of the polarization state of input light, thus allowing for the circumvention of the inherent problem of commercial electro-optic phase modulators being polarization dependent. The ultimate goal is to create a quantum network based on current optical fiber technology, and be able to show frequency-bin entanglement and distribute entanglement over fiber. However, as light propagates through the fiber, its polarization will scramble, making it detrimental to use commercial electro-optic phase modulators for the purpose of showing and distributing entanglement in optical fiber. In this chapter, the effectiveness of the PDPM in performing polarization independent phase modulation with classical light and entangled photons is demonstrated. In the case of entangled photons (biphotons) in the frequency degree of freedom, the PDPM is used in projective measurements to prove the entanglement in a specific biphoton state known as the biphoton frequency comb (BFC). The robustness of the PDPM is demonstrated by showing that the efficiency at which the projective measurements are carried out is unaffected by the polarization state of the entangled photons. Finally, the results of actively stabilizing the PDPM are shown, ensuring that the polarization of the light exiting the PDPM is stable. The work presented in this chapter was adapted from the various publications this work has appeared in [118–120].

4.1 Motivation

Entanglement in the frequency degree of freedom is compatible with modern fiber-optic networks but has largely been untapped as a resource for quantum communication. Recently, our colleagues at the Oakridge National Laboratory outlined ways to perform quantum information processing in the spectral domain using only Fourier transform pulse shapers and phase modulators (PMs) [121]. Although the spectral domain has been widely untapped for entanglement preparation, it is chosen for its compatibility with standard telecommunication equipment, compatibility with current fiber optic technology, and for its robustness against noise in fiber propagation [122]. Fourier transform pulse shapers are used to act on each frequency individually and the electro-optic phase modulators are used to move the photons across different frequencies. Colleagues at the US Army Research Laboratory (ARL) want to harness the power of hyperentanglement (entanglement in more than one degree of freedom) in the frequency and polarization degrees of freedom in order to achieve the ultimate goal of a quantum network based on current optical fiber technology. Polarization-entangled photons are a popular choice for quantum networking protocols owing to their compatibility with standard telecommunications equipment.

Recently, on-chip microresonators have been shown to be an excellent source for generating frequency-bin entangled photon pairs [91, 92]. One state that is of particular interest is the biphoton frequency comb (BFC) which is a coherent superposition state of N -energy matched comb line pairs. The general state of the BFC can be written as equation 4.1, α_k is a complex number that represents the joint amplitude and joint phase of the k^{th} comb line pair [90].

$$|\Psi\rangle_{\text{BFC}} = \sum_{k=1}^N \alpha_k |k, k\rangle_{\text{SI}} \quad (4.1)$$

Recent work has shown that electro-optic phase modulation can be used to mix frequencies from different modes to generate indistinguishable superposition states in frequency and carry out projective measurements that are sensitive to the phase

on comb line pairs [90–92], confirming high-dimensional frequency-bin entanglement. However, phase modulators, whether they are based on the linear electro-optic effect in χ^2 materials [123, 124], the carrier dispersion effect in silicon [125], or resonant cavities [126], are sensitive to the polarization of light. Therefore, harnessing hyperentanglement in the polarization and frequency degrees of freedom, for use over fiber-optic networks, requires a polarization diversity scheme capable of measuring frequency-bin entanglement regardless of photon polarization.

4.2 Polarization Diversity Phase Modulator

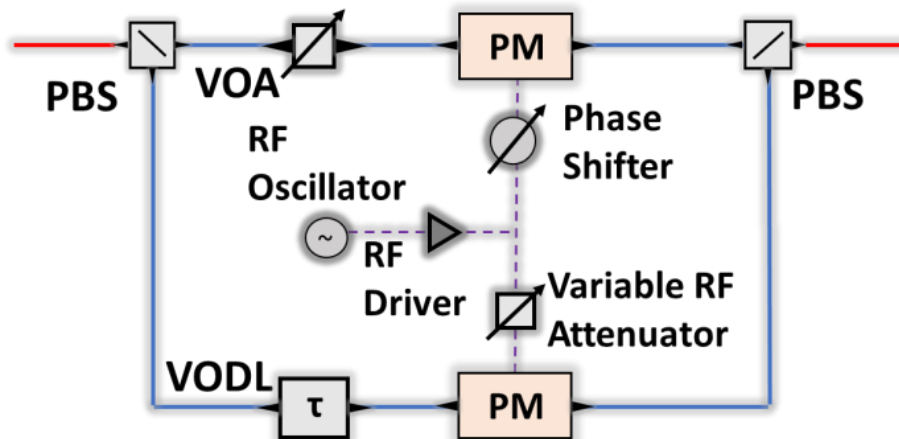


Fig. 4.1.: Schematic of the polarization diversity phase modulator (PDPM) – single-mode and polarization-maintaining fiber are depicted in red and blue, respectively. PBS - polarization beam splitter, VOA - variable optical attenuator, VODL - variable optical delay line, PM - phase modulator.

The experimental setup that is used to achieve polarization-independent phase modulation is shown in figure 4.1. The polarization diversity phase modulator (PDPM) is comprised of two fiber-based polarization beam splitters (PBSs) and two PMs. Light enters the PDPM through the PBS on the left (insertion loss (IL) of 0.2 dB), and is split into orthogonal polarization components ('s' and 'p') that propagate along

separate channels. Both channels of the device use polarization-maintaining fiber, and the light in each channel is modulated independently by a different PM (IL = 2.7 and 3.7 dB). A second fiber PBS (IL = 0.4 dB) recombines light from the two channels to return a phase modulated version of the arbitrarily polarized input signal [118].

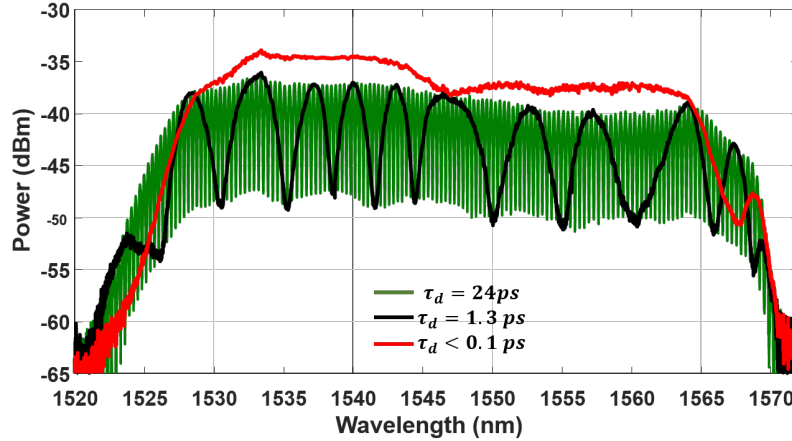


Fig. 4.2.: Progression of spectral ripple removal, signifying balancing the lengths of the arms of the PDPM.

To carry out polarization-independent phase modulation on frequency-bin entangled photons, the two paths through the PDPM need to be sufficiently indistinguishable so that path information cannot be gleaned from the system [127, 128]. The path length and optical loss through the two arms of the PDPM need to be nearly identical. Also, the RF drive to the two PMs in terms of modulation index and RF delay need to be matched too.

A variable optical attenuator (VOA, min. IL = 1.5 dB) was tuned until the optical loss through each arm was the same. To determine the path length difference between the arms of the PDPM, broadband light was launched into the PDPM, so that at least some light entered each arm. The output of the PDPM was sampled with a polarizer (oriented at 45° relative to the polarization in PDPM channels) and sent to an optical spectrum analyzer (OSA). The path length difference between the arms was estimated from the spacing of the spectral fringes [18]. The two polarization modes

propagating in the different arms of the interferometer will accrue different phases in a manner analogous to polarization mode dispersion (PMD) [129, 130], when the interferometer is unbalanced. Any difference in path length between the arms of the interferometer will manifest as ripple in the output spectrum. By varying the delay introduced by the variable optical delay line (VODL, IL = 1.0 dB), the path length difference is minimized by eliminating ripple in the output spectrum. A progression of the spectral ripple elimination is shown in figure 4.2. The green spectrum shows a delay of approximately 24 ps, after varying the VODL, the delay is reduced to 1.3 ps (black) until finally reaching a delay less than 0.1 ps (red). We were able to set the relative delay to zero with a precision of $\approx 60 fs$, limited by slow delay fluctuations in the ambient environment. Although there are fluctuations in polarization of photons exiting the PDPM, this does not affect the efficacy of the frequency-bin entanglement measurement as long as polarization-independent single photon detectors are used. However, work at the end of this chapter outlines the results of active stabilization in order to ensure the polarization of light out of the PDPM is stable. Another reason for setting the path length difference to zero, is that it allows for a larger working bandwidth for the PDPM. When the path length difference is set to approximately zero, the ripple is removed in the spectrum, see figure 4.2, and more wavelengths can be launched into the PDPM for phase modulations. Otherwise, one must choose the wavelength of the input light to be aligned with one of the maxima in the spectral ripple, thus reducing the bandwidth of the PDPM.

Each PM in the PDPM has its own modulation efficiency, or modulation index, (V_π). Consequently, when both modulators are driven with the same RF waveform and continuous wave (CW) optical test signal, frequency combs with slightly different spectra are generated. To ensure that both PMs impart identical phase shifts, an RF attenuator was used to adjust the power delivered to the PM with higher modulation efficiency. To minimize the RF delay between the driving waveforms, the output of the PDPM was sampled in a manner similar to that described above. Any delay between the RF driving waveforms induces a linear spectral phase shift, which manifests as

asymmetry in the comb spectrum. An RF phase shifter was used to reduce the RF delay between the driving waveforms.

As currently constructed, the PDPM has an IL of 5.6 dB. However, one of the larger sources of loss stems from the fact that the PMs in the PDPM have different ILs (2.7 and 3.7 dB). Matching their losses to the lower value would save a dB in the overall system loss.

4.3 Frequency Bin Entanglement Measurements

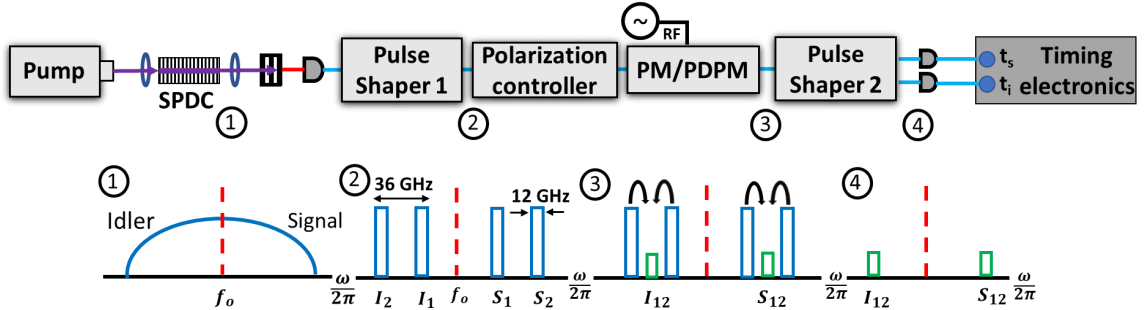


Fig. 4.3.: Experimental setup for measuring frequency-bin entanglement in a BFC. Note that either a standalone phase modulator (PM) or polarization diversity phase modulator (PDPM) is used to mix frequencies in this arrangement.

After matching both arms of the PDPM, the polarization diversity scheme was used to characterize frequency-bin entanglement in a BFC in a manner similar to that presented in references [90–92], where different frequency modes are mixed using electro-optic phase modulation. If, for example, the frequency of phase modulation equals one-half the frequency spacing between the frequency bin pairs i.e. the free spectral range (FSR) of the BFC, one can project adjacent signal and idler pairs on top of each other, thereby creating indistinguishable superposition states at frequencies halfway between the original modes (I_{12} and S_{12} in figure 4.3). By varying the joint phase on one of the BFC comb line pairs, it is possible to vary the overall amplitude

of this superposition state and, therefore, the probability of detecting coincidences at intermediate frequencies I_{12} and S_{12} . The result is a sinusoidal variation in the number of coincidences, an interference trace, as a function of the joint phase on one of the comb line pairs [92]. To claim 2-dimensional frequency-bin entanglement, the visibility of the interference trace must exceed the 71% classical limit [131]. This limit is attributed to Collins et. al. (reference [131]) in which a method for inferring a Bell state violation in terms of the visibility of an interference trace is presented. Bell states, or inequalities, are maximally entangled states, [132], and violation of these states (inequalities) can be seen as a witness of useful entanglement [133].

The setup for carrying out the projective measurements and visualizing the frequency-bin entanglement across comb line pairs is shown in figure 4.3. A CW laser pumps a periodically poled lithium niobate (PPLN) waveguide, which generates a broadband (5 THz) spontaneous parametric downconversion (SPDC) spectrum. A BFC is carved from this continuous spectrum by a pulse shaper (Pulse Shaper 1, IL = 6 dB) that is set to yield a BFC with an FSR of 36 GHz, and each frequency mode has a bandwidth of 12 GHz. A polarization controller was placed after the pulse shaper and used to vary the polarization of the BFC at the input of the PDPM (or standalone PM). The PDPM (or standalone PM) was driven at half the FSR of the BFC (18 GHz) in order to overlap adjacent frequency modes. A second pulse shaper (Pulse Shaper 2, IL = 6 dB) was used to route the output of the PDPM (or standalone PM) and send signal and idler photons at the intermediate frequencies to a pair of InGaAs single photon detectors. An event timer was used to tag single photon events and generate a histogram of two-photon coincidences.

The losses through the elements in figure 4.3 add up to around 18 dB. However, photonic integration can play a significant role in lowering the component and system losses. For example, a channel in a pulse shaper can be realized with a pair of filters and a phase shifting element between. In a silicon photonics platform, such a device could have an IL less than 0.45 dB [134]. Furthermore, there have been impressive advances in the last year with regard to low loss PMs [10]. Consequently, low loss

PDPMs (≈ 2.0 dB) and pulse shapers (≈ 0.5 dB) could be realized based on current advances in microfabrication. Photonic integration also makes it possible to achieve phase stability between the arms of the PDPM at no additional cost.

To quantify the effectiveness of the polarization diversity scheme, the performance of the PDPM was compared with that of a standalone PM. Both devices were first characterized using linearly polarized classical light from a CW laser. A deterministic polarization controller (DPC) was used to vary the state of linear polarization at the input port of a standalone PM. The results are illustrated in figure 4.4A. The PM efficiently scatters light into the +1 sideband when the state of polarization is aligned with the slow axis (SA in figure 4.4A) of the PM fiber input. This is the direction that is aligned with the r_{33} electro-optic coefficient of lithium niobate. As the polarization is tuned toward the fast axis of the PM fiber input (FA in figure 4.4A), some of the light in the PM is now orthogonal to the r_{33} coefficient and passes through the device undergoing substantially reduced phase modulation (factor of 0.14 of original). These experiments were repeated with the PDPM, and the results are shown in figure 4.4D. The polarization diversity scheme functions as expected, and the normalized optical power in the +1 sideband varies from 0.986 to 1 ($\sigma = 0.004$). It should be noted that in these experiments the DPC used to control the polarization was a commercially available component (Thorlabs DCP5500) with an insertion loss of approximately 1.1dB.

The projective measurements were then carried out on a BFC with only two comb-line pairs. In this case, equation 4.1 simplifies to

$$|\Psi\rangle_{\text{BFC}} = \frac{1}{\sqrt{2}} [|1, 1\rangle_{\text{SI}} + e^{i(\phi_{\text{S2}} + \phi_{\text{I2}})} |2, 2\rangle_{\text{SI}}] \quad (4.2)$$

For each device - PDPM and standalone PM - interference traces were generated by recording coincidence and count rates as a function of the joint phase ($\phi_{\text{S2}} + \phi_{\text{I2}}$) on $|2, 2\rangle_{\text{SI}}$. For each value of the joint phase, coincidences were recorded over three equal time intervals (5 min intervals for the PDPM and 2 min intervals for the standalone PM). The average number of coincidences and their standard deviation over these

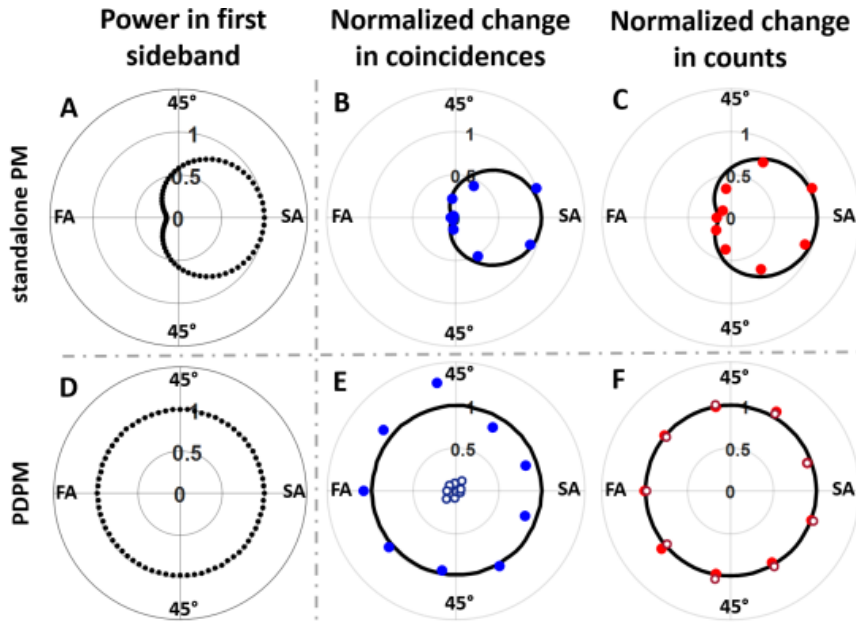


Fig. 4.4.: (A), (D) show the change in power scattered into the +1 sideband, as a function of polarization, for a standalone PM and the PDPM, respectively. (B)-(C) show the change in coincidence and count rates for frequency-bin entanglement measurements using a standalone PM. (E)-(F) are analogous to (B)-(C) but for the PDPM and include data for two values of the joint phase – $\phi_{S_2} + \phi_{I_2} = 0$ (solid) and $\phi_{S_2} + \phi_{I_2} = \pi$ (hollow). Results are plotted on an azimuthal slice of the Poincaré sphere corresponding to linearly polarized light. (SA – slow axis and FA – fast axis)

three intervals were calculated after subtracting accidentals. Due to the high system losses enumerated above (18 dB including pulse shapers and PDPM plus the 1.1 dB loss from the DPC), as well as the low efficiency of our detectors (10% and 20%), the rate of accidentals was three to four times that of coincidences. The full interference traces, for nine different values of the joint phase, are shown in figure 4.5. For the standalone PM, two-photon interference traces were generated for three different polarization states of the BFC - 0° , 90° , and an orientation roughly between these states. These angles are defined relative to the slow axis of the PM fiber input, which is polarization-maintaining. As the polarization of the BFC is tuned away

from 0° , the number of counts at the overlap frequencies (I_{12} and S_{12}) is expected to fall, as the component of the wavefunction aligned with the r_{33} EO coefficient gets smaller and smaller. As expected, the number of coincidences falls off at a sharp rate, resulting in lower fringe amplitude. When the BFC is aligned with the FA of the PM fiber input (dotted lines in figure 4.5A), the count rate (red) is reduced to 0.28 of that when the BFC is aligned with the SA (solid lines in figure 4.5A). The recorded coincidences (blue) from the BFC are reduced to a factor of 0.07, compared to when the BFC is aligned with the SA. For the PDPM, an interference trace was recorded for the case where photons are equally likely to end up in either arm of the device (dashed lines in figure 4.5B). To see if there was any residual polarization dependence, an interference trace was then recorded for a case where all the photons passed through only one arm of the device (solid lines in figure 4.5B). A drift in the setup over the long acquisition time (around 3 hours) may be responsible for some of the differences between the traces in figure 4.5B. However, the polarization diversity scheme is clearly more robust to changes in BFC polarization. The count and coincidence rates for the PDPM are lower compared to that of the standalone PM (BFC polarization at 0), because the polarization diversity scheme has a higher IL.

Having established that the PDPM can be used to visualize strong two-photon interference in a BFC, regardless of polarization, we now quantify its performance and contrast it with that of a standalone PM. For these measurements, the BFC polarization was varied using a DPC while keeping the joint phase on $|2, 2\rangle_{SI}$ set to 0, the value at which coincidences are expected to be at a maximum. The results are presented in figure 4.4B and 4.4C, and show that the count and coincidence rates are sensitive to BFC polarization. For measurements with the PDPM, the count and coincidence rates are relatively immune to changes in BFC polarization (figures 4.4E and 4.4F). The results from classical measurements (figures 4.4A and 4.4D) were used to determine the expected change in the count and coincidence rates as a function of BFC polarization. The counts are expected to track with the power scattered into the

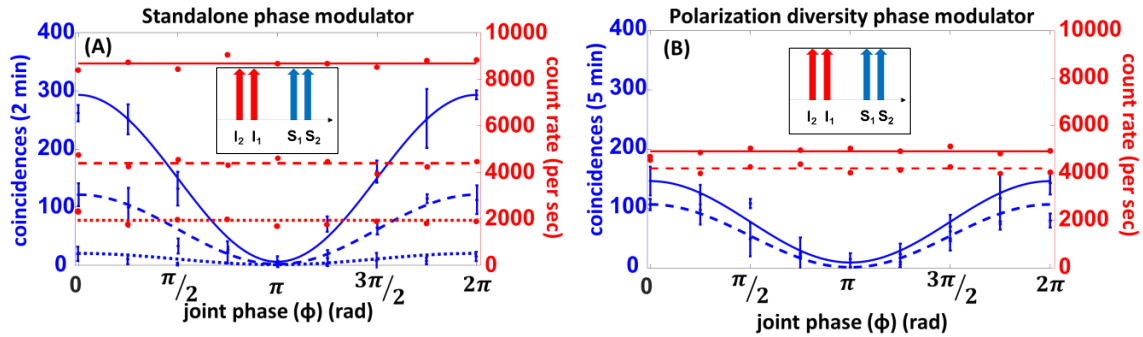


Fig. 4.5.: Results from frequency-bin entanglement measurements. (A) Coincidences (blue) and counts (red) when using the standalone PM for three different orientations of the polarization - 0° (solid), 90° (dotted), and an intermediate state (dashed). (B) Coincidences and counts when using the PDPM for two cases - one where photons are equally likely to be in either arm (dashed) and the other where photons go entirely through one arm (solid). The insets show the relative orientation between the polarization of signal and idler bins.

+1 sideband in classical experiments. Coincidences, on the other hand, are expected to fall off quadratically with respect to the drop in power in the +1 sideband. Based on these relationships, the expected change in the normalized count and coincidence rates is plotted (black lines) alongside the actual change in count and coincidence rates. There is good agreement between the data from classical measurements and that from two-photon interferometry. Finally, the measurements using the PDPM were repeated, but with the joint phase on $|2, 2\rangle_{\text{SI}}$ set to π (hollow markers in figures 4.4E and 4.4F). Coincidences at the intermediate frequencies are expected to be at a minimum for this value of the joint phase (see figure 4.5), which is what was observed. These measurements were made to establish that the coincidences in figure 4.4E are the result of two-photon interference and not the result of leakage from the original signal and idler bins. It is important to note that a CW laser out-of-band was co-propagated with the entangled photons such that there was enough optical power for

the DPC to change the state of polarization. And to ensure that this out-of-band optical power would not damage single photon detectors, spectral filters (wavelength division multiplexers) were connected at the output of the entire system such that the out-of-band CW power was suppressed. Each spectral filter has 0.47 dB of insertion loss and an isolation of 35 dB.

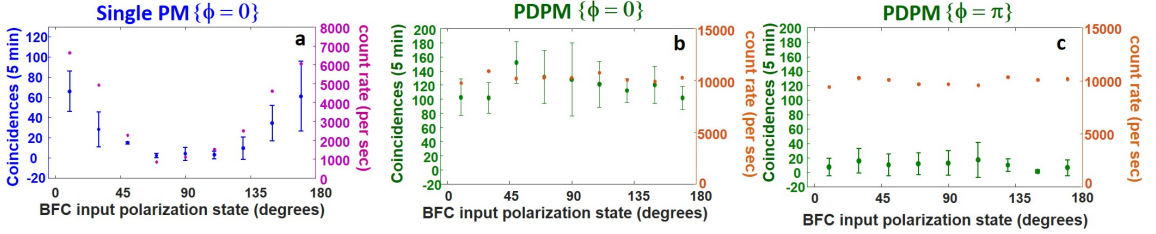


Fig. 4.6.: The figures, going from left to right, contrast the performance of a standalone PM with the PDPM. Data for the PDPM is presented for two values of the joint phase ($\phi = \phi_{S_2} + \phi_{I_2}$) on S_2I_2 . Data for the the $\phi = \pi$ point was recorded to clearly establish that the coincidences recorded in (b) are the result of two-photon interference and not leakage from neighboring frequency-bins. (a) Coincidences and count rate, as a function of BFC polarization, in two-photon interference experiments when using standalone PM. (b)-(c) analogous to (a) but for the PDPM.

Figure 4.6 shows the same results as figure 4.4 B-C (standalone phase modulator) and 4.4 E-F (PDPM) but presented in a different plot. The plots show the results of the frequency-bin entanglement measurements for 9 different (linear) polarizations of the BFC. Changes in the BFC polarization state had a dramatic effect on the number of coincidences and counts recorded when a standalone PM was used to measure frequency-bin entanglement (figure 4.6a). For the PDPM, the polarization independence was depicted in figure 4.6b. Varying the polarization has little effect on the recorded coincidences and count rate. Finally, to ensure that the coincidences and counts recorded for the PDPM were not from leakage from neighboring frequency-bins, the joint phase on S_2I_2 was set to π , figure 4.6c. At this point, the coincidences

are close to zero, while the count rate remains constant, thereby showing that the data in 4.6b is valid.

4.4 Cross-Polarized Signal and Idler Photon Pairs

Thus far, projective measurements were performed on co-polarized signal-idler pairs. However, it is important that any polarization diversity scheme be sufficiently robust to also handle instances where the entangled photons are orthogonally polarized with respect to one another. Since a standalone PM can only modulate one polarization component at a time, we expect that its ability to efficiently mix frequencies of orthogonally polarized signal-idler pairs will be limited.

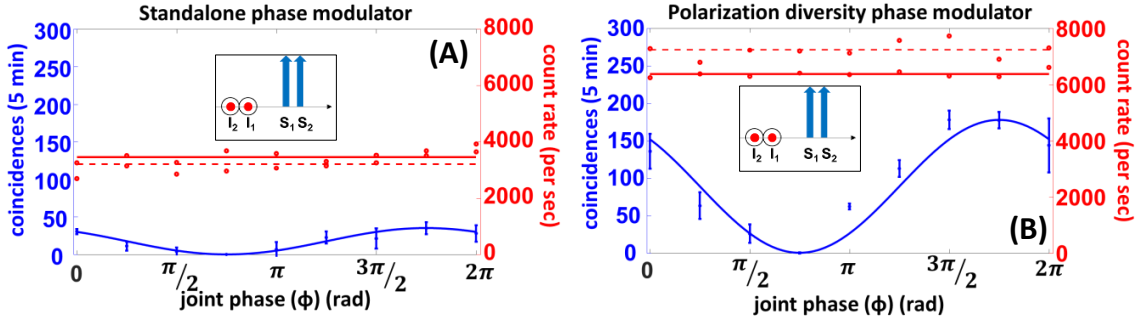


Fig. 4.7.: Frequency-bin entanglement measurements on orthogonally polarized signal-idler pairs using (A) a standalone PM and (B) the PDPM. Dashed and solid red lines correspond to the signal and idler count rates, respectively. The insets show the relative orientation between the polarization of signal and idler bins.

To prepare orthogonally polarized signal-idler pairs, we took advantage of frequency dependent polarization rotation in a birefringent fiber. The SPDC spectrum was carved into a BFC consisting of signals and idlers 1.3 THz apart from each other, with the S_1S_2 and I_1I_2 spacing kept at 36 GHz. The resulting BFC was launched at 45° relative to the slow axis of a 28 cm section of polarization-maintaining fiber (with an estimated differential group delay of 1.73 ps/m). The signal-idler spacing

was chosen so that the number of Poincaré sphere rotations undergone by the signal and idler polarizations differed by one-half rotation at the output of the section of polarization maintaining fiber. The 1.3 THz frequency spacing is chosen to ensure that the polarization between the signal and idler pairs is rotated and not the polarization between S_1S_2 (and similarly I_1I_2). Interference traces similar to those recorded in figure 4.5 were then generated, but with the signal and idler polarizations orthogonal to one another. Figure 4.7 shows that the amplitude of the two-photon trace generated using a standalone PM is very low since a standalone PM is unable to efficiently mix the frequencies of both signal and the idler photons simultaneously. The PDPM is clearly not limited in this regard.

4.5 Co- and Cross-Polarized Signal and Idler Photon Pairs in a Depolarized Biphoton Frequency Comb

Since propagation over fiber may scramble the polarization of light, in the previous sections the polarization diversity phase modulator (PDPM) was used to carry out projective measurements in the frequency domain for arbitrary, but static, states of polarization; this work was presented in reference [118]. We now demonstrate these projective measurements in the presence of fluctuations in the polarization state, as well as for the case of cross-polarized signal-idler pairs. This work was presented at CLEO 2019 [119] and presented below.

To demonstrate the robustness of the PDPM, frequency-bin entanglement in a biphoton frequency comb (BFC) under two important scenarios was measured. First note that the BFC was passed through a polarization scrambler to simulate either fast fluctuations in the state of photon polarization that may result from fiber-optic channel impairments or a stream of polarization-encoded qubits [128]. Second, to determine whether the PDPM is compatible with hyperentangled photons in the polarization and frequency degrees of freedom [135], the projective measurements in the frequency domain were carried out for both co- and cross-polarized signals and idler

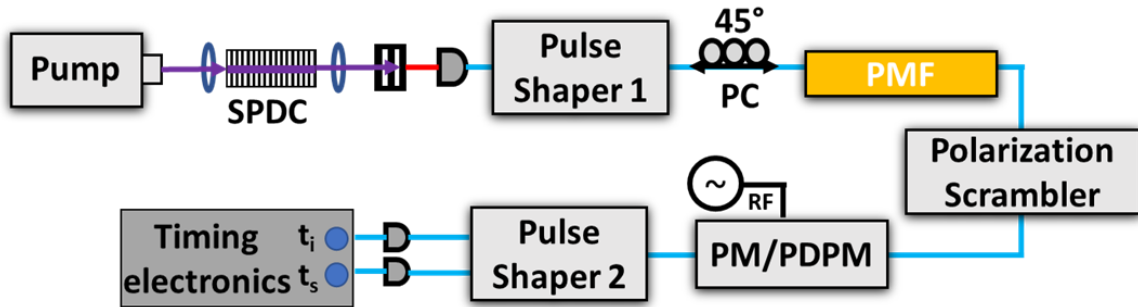


Fig. 4.8.: Experimental setup for state preparation and measurement of frequency-bin entanglement. PC – polarization controller and PMF – polarization maintaining fiber.

frequencies. These measurements are similar to those presented in figure 4.7, however in this case, new superconducting nanowire single photon detectors (SNSPDs) (Quantum Opus) were used. This allowed for more efficient measurements, however, these new detectors are also polarization sensitive.

The setup for carrying out the projective measurements in the frequency domain is shown in figure 4.8. The setup is the same as presented in figure 4.3, with polarization control introduced in the form of a polarization controller (PC) and length of polarization maintaining fiber (PMF), and the polarization scrambler was used to emulate propagation in a fiber optic network. In these measurements co- and cross-polarized frequency-bin pairs are achieved by switching the launch condition into the section polarization-maintaining fiber (to 0° or 45°), which were then scrambled prior to entering the standalone PM or PDPM for entanglement measurements [91, 92, 136]. It is also important to note the effect the polarization scrambler has on the polarization of the frequencies in the BFC.

Figure 4.9 shows the effect of the polarization scrambler on the polarization of the frequency-bins pairs. The scrambler effectively rotates the global polarization of the BFC. The effect of this on a standalone PM is described. This case is more inter-

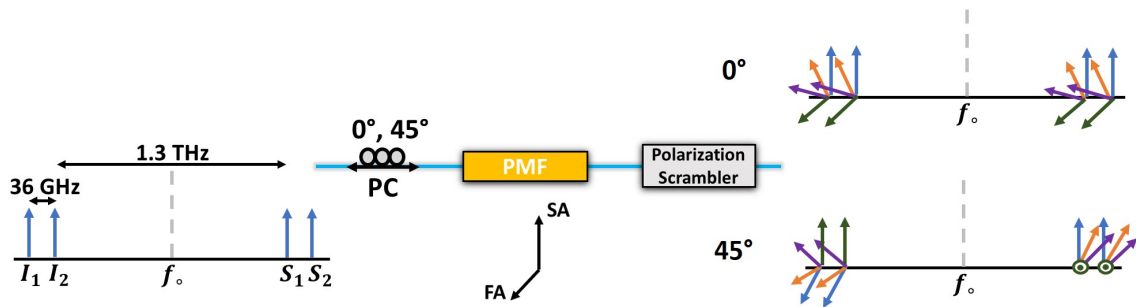


Fig. 4.9.: The effect of the polarization scrambler on the polarization state of the frequency-bin pairs when the launch condition is changed from 0° to 45° . PC – polarization controller and PMF – polarization maintaining fiber. The polarization scrambler effectively rotates the global polarization of the BFC.

esting, because the efficiency of the standalone PM in the projective measurements is dependent on the polarization state of the BFC. The PDPM is not affected by the polarization state of the BFC. In the case when the frequency-bin pairs are co-polarized (0° launch condition), the scrambler will rotate the polarization such that the frequency-bins are completely aligned with the slow-axis (blue arrows) of the PM (slow-axis being where the r_{33} component is completely aligned with the incoming light) and rotate to the point where they are completely aligned with the fast-axis of the PM (green arrows). In this case, there will be some coincidences whenever some of the light is aligned with the slow-axis of the PM (blue, orange, and purple arrows). In the case when the frequency-bin pairs are cross-polarized (45° launch condition), only one frequency-bin pair will be aligned with the slow-axis of the PM (green and blue arrows). The scrambler will rotate the polarization of the frequency-bin pairs such that some of the polarization of both the frequency-bins will be aligned with the slow-axis (purple and orange arrows). This is the case when coincidences will be recorded, until the cross-polarization is achieved again. The cross-polarized case is expected to return less coincidences.

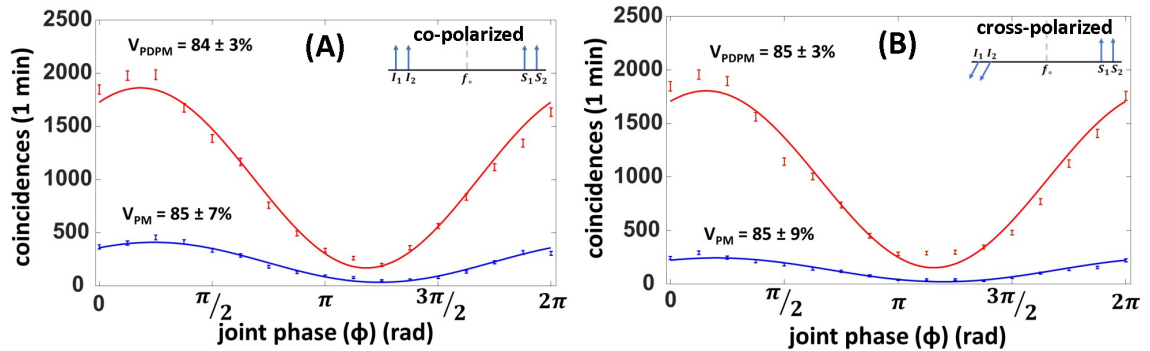


Fig. 4.10.: Interference traces and visibilities from measurements of frequency-bin entanglement in a BFC. The performance of a standalone PM (blue) was compared with that of the PDPM (red). The experiments were carried out for both co- (A) and cross-polarized (B) signal idler pairs.

The results from projective measurements are shown in figures 4.10A and 4.10B. Coincidences were recorded over 60 seconds and the results are reported without background subtraction. In all cases, the visibility of the fringes exceeded the classical limit of 71% [131], signifying frequency-bin entanglement across comb line pairs $|1, 1\rangle_{\text{SI}}$ and $|2, 2\rangle_{\text{SI}}$ [90]. From both figures it is clear that the ability of the PDPM (red traces) to carry out projective measurements in the frequency domain is unaffected by whether the signal-idler pairs are co- or cross-polarized. Equivalent traces for the standalone phase modulator is shown in blue. The fringe amplitude is lower in both figures, indicating that fluctuations in the state of polarization introduced by the polarization scrambler reduce the efficiency with which entanglement measurements can be made. Furthermore, the maximum coincidences retrieved for the co-polarized case were 457, while those for the cross-polarized case were 290. Therefore, the relative orientation between signal and idler affects the efficiency with which a standalone phase modulator can measure entanglement.

In sum, it was demonstrated that the polarization scrambling and the polarization state of the BFC mix together to reduce the efficiency at which the standalone PM

can perform the projective measurements. In contrast, the polarization diversity phase modulator can carry out projective measurements with good efficiency despite fluctuations in the state of polarization and irrespective of the relative orientation between signal and idler photons. This is a necessary step for harnessing frequency-bin entanglement for quantum communications protocols over fiber-optic networks.

4.6 Active Stabilization of Interferometer

Fluctuations in the path difference between the arms of the PDPM were observed, having a bound of approximately 60 fs. These fluctuations are not detrimental in the measurements of frequency-bin entanglement using the PDPM in the case when polarization insensitive single photon detectors are used. However, the fluctuations likely modify the polarization state of the exiting photons with respect to their state upon entering the PDPM. Therefore, active stabilization of the arms via a piezoelectric phase shifter is presented.

4.6.1 Interferometer active stabilization technique

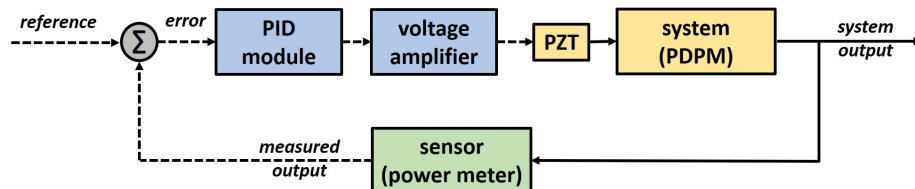


Fig. 4.11.: Block diagram of the feedback control loop for actively stabilizing the PDPM.

To actively stabilize the interferometer (PDPM), a proportional-integral-derivative (PID) control algorithm is used to actively control the voltage level on a piezo-electric fiber phase shifter (General Photonics FPS-002) that, in turn, allows for fine control of the path length difference.

The PID algorithm is a closed loop system that uses a sensor to read a signal. The desired output is obtained by calculating three responses (or variables) P (for proportional), I (for integration parameter), and D (for derivative parameter). The sum of the three responses are used to compute the output [137].

Figure 4.11 shows the block diagram of the feedback control loop used to actively stabilize the PDPM. Starting at the output of the block diagram (“system output”), the optical output of the system (PDPM) is sent to a sensor (power meter). The sensor transforms the optical signal to an electrical signal that is then compared to the reference or set point. The difference between the reference and the sensor output is the error signal that is sent to the PID module (New Focus - LB1005-S High-Speed Servo Controller), and its output is sent to a voltage amplifier. The voltage amplifier is connected electrically to the PZT and this amplified voltage allows for the active control of the phase shift imparted by the PZT. The PZT is connected optically to the system (in one arm of the PDPM) and the loop starts again after the voltage was updated by the PID module.

It is important to confirm that the PID control loop can keep up with the fluctuations in the path length of the PDPM. To be convinced that the response speed of the feedback loop is fast enough, the path length fluctuations were measured by photo-detecting the light exiting the PDPM after being sampled by a polarizer. This sampling by a polarizer allows for the orthogonal polarization components to interfere, thus demonstrating the phase accrued between the orthogonal polarization components due to the constant path length fluctuations in the arms of the PDPM. The top plot in figure 4.12 shows the path length fluctuations. This data was recorded over 500 seconds and sampled every 0.5 ms. The bottom plot of figure 4.12 shows the power spectrum of the path length fluctuations. The spectrum reveals that the path length fluctuations are concentrated between DC and 0.2 Hz, thus demonstrating that the speed of the fluctuations are several seconds. All the components in the feedback loop are fast enough to keep up with these fluctuations. The PZT has a bandwidth of 20 kHz, the power meter allows the user to choose either a 25 Hz or 100 kHz

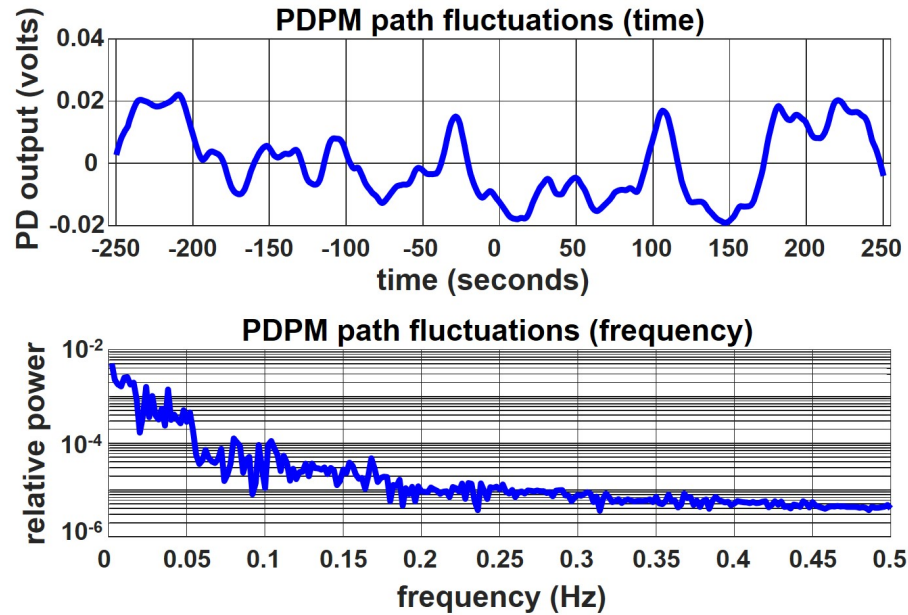


Fig. 4.12.: Measured path length fluctuations through the PDPM when the interferometer is not stabilized. The top plot shows the photodetector (PD) voltage as a function of time. The data was recorded over 500 seconds and sampled every 0.5 ms. The bottom plot shows the spectrum of the path length fluctuations, the spectrum shows that the fluctuations are in the order seconds.

bandwidth, and the PID module has a bandwidth of 10 MHz. The response speed is set by the slowest component in the feedback loop. In the following measurements, the response speed of the feedback loop is set to 40 ms, set by the bandwidth level of the power meter (25 Hz).

4.6.2 Stabilization of classical light out of interferometer

The necessity for active stabilization stems from the polarization of light fluctuating out of the interferometer that is not stabilized. The polarization fluctuation stems from the phase between the “s” and “p” orthogonal polarization components traveling in the interferometer. When the interferometer is not actively stabilized,

fluctuations in temperature and strain on the optical fiber will induce path length differences. These path length differences in turn induce a phase between the orthogonal polarization states that when sampled with a polarization controller (aligned to 45° with respect to the slow-axis) and an analyzer, interfere. This interference can be visualized by detecting the output of the analyzer via a photodetector or power-meter. The goal is to actively compensate for these interferometer fluctuations so as to have a stable output out of the analyzer and thus demonstrate polarization stability out of the interferometer.

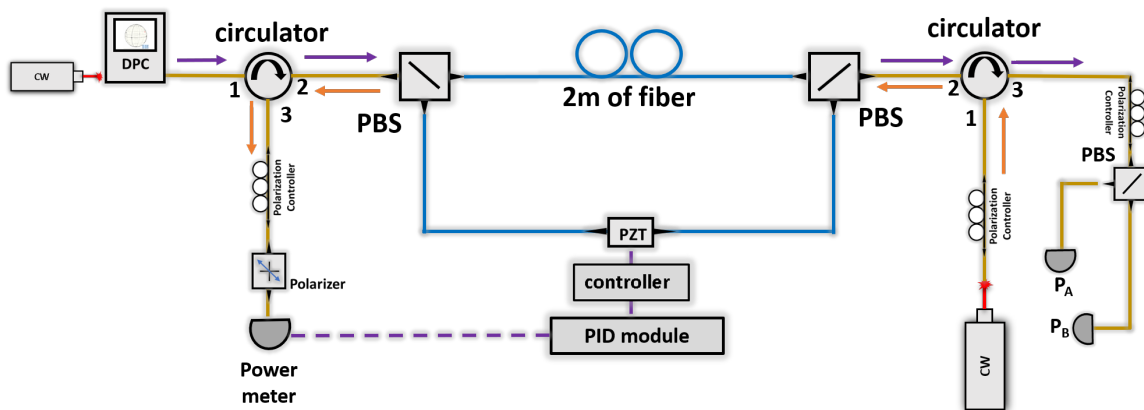


Fig. 4.13.: Setup to achieve and show active stabilization of classical light in an interferometer. DPC - deterministic polarization controller, PBS - polarization beam splitter, CW - continuous wave laser, PZT - piezo electric transducer (fiber phase shifter), PID - proportional integration derivative. $\lambda_{CW_1} = 1555$ nm and $\lambda_{CW_2} = 1545$ nm.

Figure 4.13 shows the setup used to first demonstrate the capability of actively stabilizing a test interferometer. As a first iteration, active stabilization is performed on a stripped down interferometer with the necessary optics to backwards propagate (orange path) a laser (CW_1 with center $\lambda = 1555$ nm) in order to perform the stabilization. Circulators are used to ensure proper propagation of light into and out of the interferometer.

The input circulator, in this case, takes into port 1 the classical light (CW_2 with center $\lambda = 1545$ nm) out of the deterministic polarization controller (DPC) and sends it out of port 2 and into the first polarization beam splitter (PBS). This is the “forward path” and is denoted by the purple arrows. This light continues into the interferometer and out of the second PBS. It continues its course into port 2 of the output circulator until it exits port 3. After this, the light is sent into a test PBS in which the polarization stability is tested when the interferometer is and is not actively stabilized. To visualize this, two power meters are connected to the two output ports of the test PBS (P_A and P_B).

Continuing with figure 4.13, attention is now turned to the “backwards path” denoted by the orange arrows. This is the path taken by the stabilization laser (CW_1). This is the laser that is detected by the sensor that is then used by the PID module to actively control the PZT voltage and actively stabilize the interferometer. Starting at port 1 of the output circulator, the light travels out of port 2 and into the output PBS of the interferometer. The light is launched such that each arm has equal power i.e. the polarization controller connected to port 1 of the output circulator is varied until achieving a polarization state of 45° with respect to the slow axis. The light continues through the interferometer and out of the input PBS where the two orthogonal polarization states are recombined. The light travels into port 2 and out of port 3 of the input circulator. The light is then sampled by a polarizer (also typically called an “analyzer”) so as to visualize the effect of the phase between the orthogonal polarization states. A polarization controller (PC) is used to ensure sampling of both orthogonal polarization through the interferometer, thus inducing their interference that is indicative of the phase difference between the orthogonal polarizations. This sampled light is then detected by a power meter and the electrical signal is sent to the PID module. When the interferometer is not stabilized, the environmental fluctuations imparted onto the fibers of the interferometer will cause a phase difference between the two polarizations. This is visualized by a large variation in optical power detected by the power meter. The goal is to reduce these large

power fluctuations and have a steady reading of output power, signifying that the path length differences are compensated. This elimination of path length difference is indicative of eliminating the phase between the polarization states, and therefore having a constant polarization state of output light.

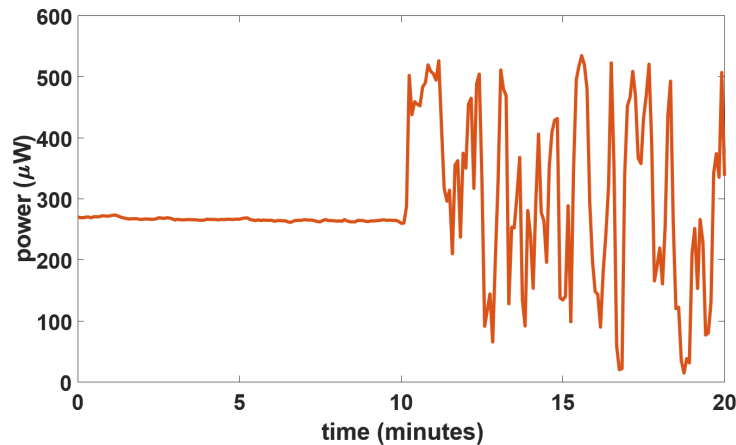


Fig. 4.14.: 20 minute measurement of the output power of the stabilization laser (backwards path - orange arrows). This shows the interferometer being stabilized for the first 10 minutes and not being stabilized for last 10 minutes. For the data with stabilization on, the standard deviation of the fluctuations is $2.57 \mu\text{W}$, and for the stabilization off data the standard deviation is $150.36 \mu\text{W}$.

Figure 4.14 shows the output power of the stabilized laser (backwards path - orange arrows) when the interferometer is stabilized (the first 10 minutes) and when the stabilization is turned off (last 10 minutes). When the stabilization is on, the mean is $265.75 \mu\text{W}$ with a standard deviation of $2.57 \mu\text{W}$. When the stabilization is turned off, the mean is $305.43 \mu\text{W}$ with a standard deviation is $150.36 \mu\text{W}$. This figure clearly shows the polarization stability of the stabilization laser when the stabilization is on. This allows for the demonstration of polarization stability of the classical light propagating in the forward path of the interferometer.

Figure 4.15 shows the effect on the polarization of the classical light (CW_2) propagating in the forward direction (purple arrows). A power meter is connected at each

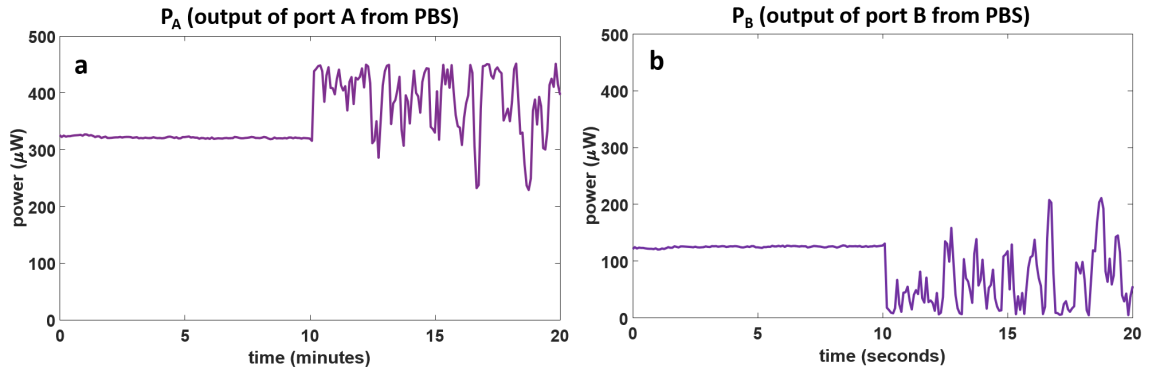


Fig. 4.15.: 20 minute measurement of optical power of classical light (forward propagation - purple arrows). This shows the interferometer being stabilized for the first 10 minutes and not being stabilized for last 10 minutes. The polarization setting on the DPC is set to a polarization ensuring light through both arms of the PDPM and causes this power imbalance between output ports of the test PBS. a - port A of the test PBS, b - port B of the test PBS.

of the output ports of the test PBS, in order to visualize the effect on the orthogonal polarization states out of the interferometer. In this case, the polarization of the incoming CW_2 light is set to a polarization setting via the DPC such that there is light in both arms of the PDPM. The stabilization of the interferometer is on for the first ten minutes and off for the last ten minutes. For port A of the test PBS the mean for stabilization on is $320.82 \mu\text{W}$ with a standard deviation of $1.75 \mu\text{W}$ and for stabilization off the mean is $388 \mu\text{W}$ with a standard deviation of $55.69 \mu\text{W}$. For port B of the test PBS the mean for stabilization on is $124.63 \mu\text{W}$ with a standard deviation of $1.56 \mu\text{W}$ and for stabilization off the mean is $62.45 \mu\text{W}$ with a standard deviation of $51.72 \mu\text{W}$. This clearly shows the effect, and importance, of the stabilization of the interferometer on the classical light into the interferometer.

Finally, to show the robustness of the stabilized interferometer, the polarization of classical light at the input of the interferometer is varied from -90° to $+90^\circ$ (measured

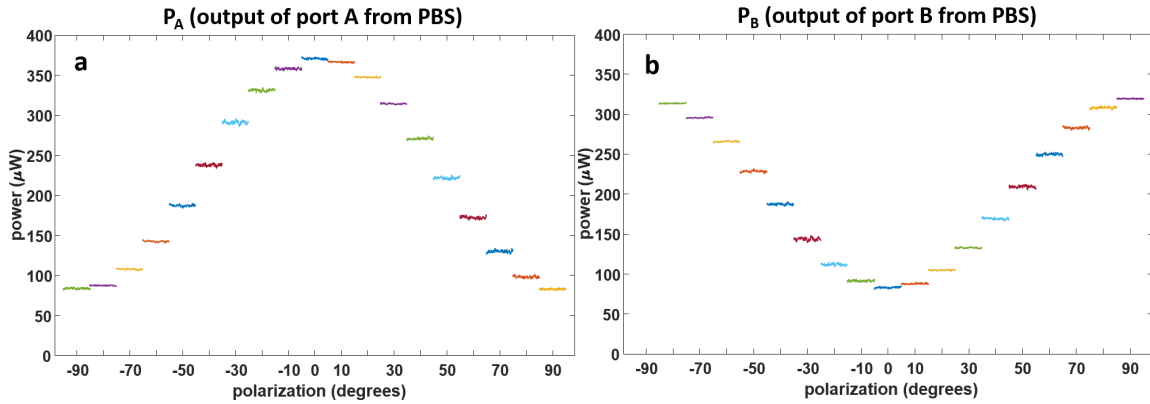


Fig. 4.16.: Polarization stability of the classical light through the test interferometer as its polarization is swept from -90° to $+90^\circ$ in 10° increments. Power is recorded out of each port of the test PBS for 10 minutes at each polarization setting. a – port A of the test PBS. b – port B of the test PBS.

at the input of the PDPM via the DPC) at 10° increments via the DPC. The output ports the test PBS, connected to the port 3 of the output circulator, are connected to power meters and the power is tracked as the input polarization is varied. Figure 4.16 shows the power of the output ports of the test PBS. At each polarization, the power was recorded for 10 minutes and each measurement has a less than 1% variation in power.

4.6.3 Stabilization of classical light through the polarization diversity phase modulator

In the second iteration of the classical stabilization measurements, the PDPM was rebuilt and actively stabilized with classical light. The major concern here is, what happens to the stabilization when the phase modulators are turned “on” (driven with an amplified RF sinusoid)? Figure 4.17 shows the experimental setup for actively stabilizing the PDPM with RF control (RF variable attenuator and RF phase shifter).

In this case, the RF parameters – delay and modulation index – are balanced for each PM in the PDPM. Optical balancing was also performed by matching the insertion loss in each arm and the optical path length between the arms.

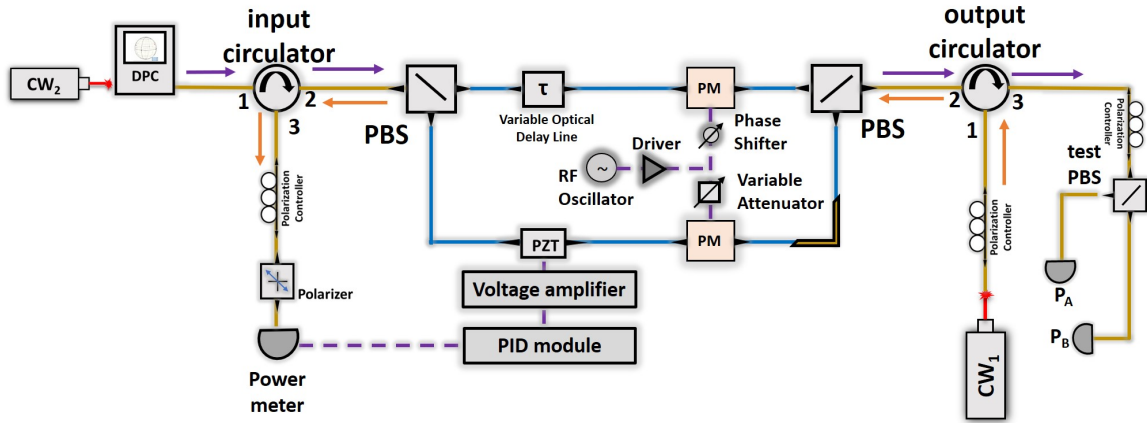


Fig. 4.17.: Experimental setup for active stabilization of the PDPM. The RF components necessary to balancing the PDPM electrically are now incorporated. This setup is used to demonstrate that the polarization transformation observed in figure 4.21 is due to the RF delay mismatch between the PMs.

The stabilization performed in this iteration employs the same experimental principle outlined in the previous section, and depicted in figure 4.13. A stabilization laser ($CW_1 - \lambda_{CW_1} = 1555 \text{ nm}$) propagates backwards (orange arrows) through the PDPM and is sampled by a polarizer. This sampled light is the error signal used by the PID module to actively stabilize the PDPM. The polarization stability achieved by the active stabilization is confirmed by analyzing the polarization of classical light ($CW_2 - \lambda_{CW_2} = 1545 \text{ nm}$) out of the PDPM in the forward (purple arrows) propagation direction by monitoring the power out of the output ports of a test PBS. In all results shown in this section, the PMs are “on” (driven with RF sinusoid – RF frequency = 18 GHz and RF power = 27 dB), unless otherwise stated.

To visualize how the polarization of the light varies when the interferometer is not stabilized, the stabilization laser (CW_1), after propagating through the PDPM, is sampled by a polarization controller and polarizer. This will allow for interference of the orthogonal polarization components and thus give an insight into the phase between the orthogonal polarization components. Figure 4.18 shows the effect of having the PDPM stabilized (first ten minutes of trace) and not having the PDPM stabilized (last ten minutes). For the first ten minutes, the mean is $246.32 \mu\text{W}$ with a standard deviation $0.032 \mu\text{W}$. For the last ten minutes, the mean is 250.11 with a standard deviation of $152.36 \mu\text{W}$.

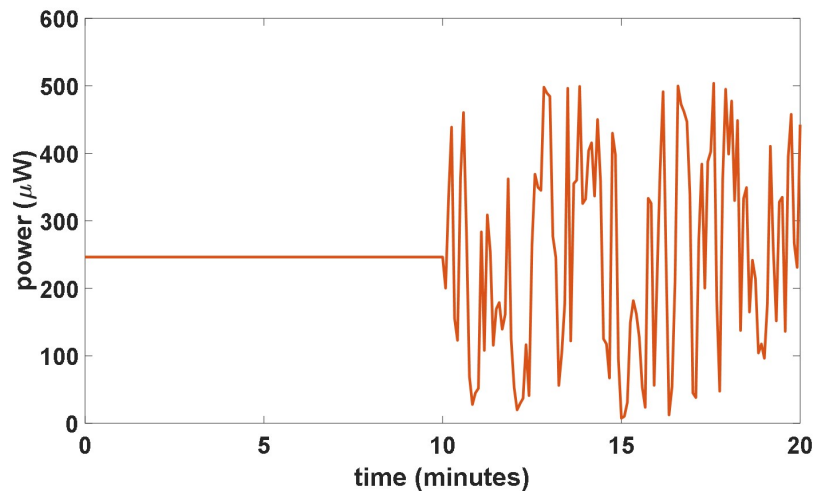


Fig. 4.18.: 20 minute measurement of stabilization laser output. The first ten minutes are with stabilization on (and RF delay balanced), and the last ten minutes are with stabilization off. For the data with stabilization on, the standard deviation of the fluctuations is $0.032 \mu\text{W}$, and for the stabilization off data the standard deviation is $152.36 \mu\text{W}$.

The same 20 minute long measurement is performed for the forward propagation path, using classical light (CW_2). Figure 4.19 shows the polarization stability of the classical laser by monitoring the power out of ports of the test PBS in the forward direction. Clearly, when the stabilization of the PDPM is on, the polarization does

not fluctuate as it does when the PDPM is not stabilized. For port A of the test PBS, with stabilization on – mean is $495.60 \mu\text{W}$ and standard deviation is $1.51 \mu\text{W}$, with stabilization off – mean is $367.14 \mu\text{W}$ and standard deviation is $90.78 \mu\text{W}$. For port B of the test PBS, with stabilization on – mean is $47.85 \mu\text{W}$ and standard deviation is $1.38 \mu\text{W}$, with stabilization off – mean is $169.77 \mu\text{W}$ and standard deviation is $85.50 \mu\text{W}$.

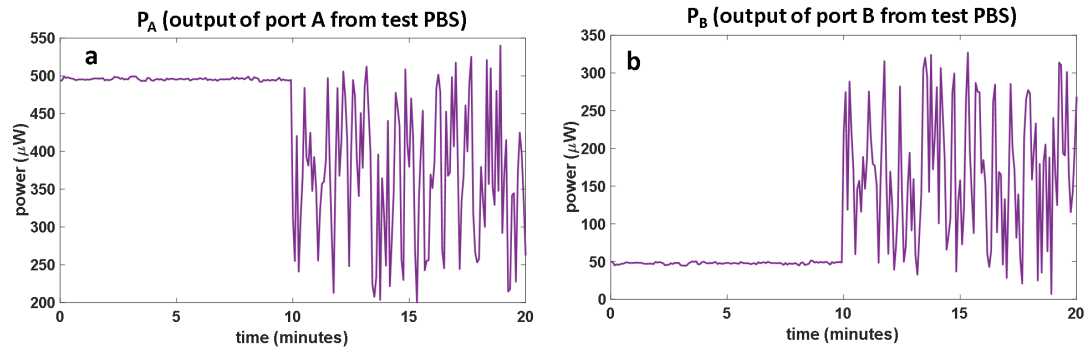


Fig. 4.19.: 20 minute measurement of the polarization stability of the classical light in the forward propagation direction (purple arrow). a - port A of the test PBS. b - port B of the test PBS.

To further demonstrate the polarization stability, the polarization of the classical light (CW_2) in the forward direction was varied from -60° to $+60^\circ$ in 10° increments (this polarization was measured and varied via the DPC at the input of the PDPM). Figure 4.20 shows the outputs of the test PBS in the forward propagation direction as the polarization of the light is varied. At each polarization point, 5 minute traces are recorded. It is clear that, with the stabilization on, the polarization is stable at each setting. This answers the question as to what effect the PMs being on has on the active stabilization. The stabilization is performed successfully just as before with the test interferometer. To re-iterate, this stabilization was performed with the PMs on and the RF delay and modulation index balanced for each individual PM in the

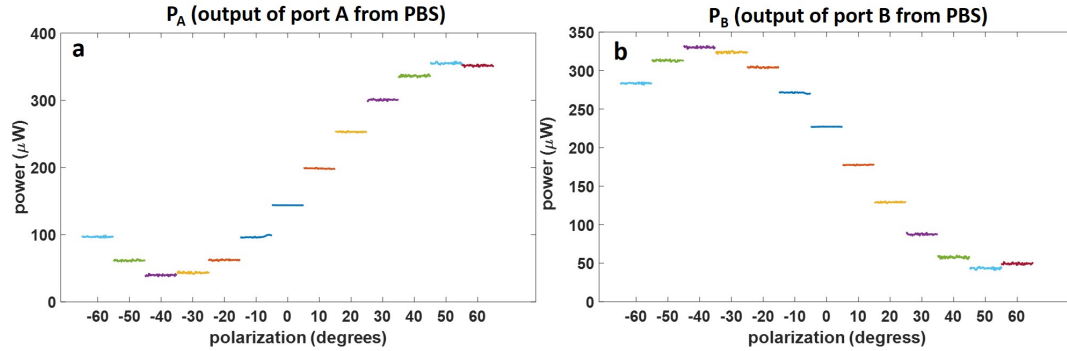


Fig. 4.20.: Polarization stability of the classical light through the PDPM with the PMs on and RF delay balanced as its polarization is swept from -60° to $+60^\circ$ in 10° increments (measured and controlled with the DPC at the forward input of the PDPM). Power is recorded out of each port of the test PBS for 5 minutes at each polarization setting. a – port A of the test PBS. b – port B of the test PBS. The extinction between the output ports of the test PBS is increased when the RF delay is balanced.

PDPM. One interesting observation occurred when the RF delay was not balanced. The next section details the observation.

4.6.4 Effect of RF delay imbalance on the polarization state of light exiting the PDPM

In previous sections of this chapter, methods for balancing the PDPM both optically and electrically were outlined. During the projective measurements previously presented, the RF delay between the PMs in the PDPM was always balanced. Therefore, the effect of RF delay mismatch has never been tested. However, although stabilization was successfully achieved, an interesting observation was stumbled upon when the RF delay was imbalanced between the PMs of the PDPM.

The polarization of the classical light (CW_2) was varied from -50° to $+50^\circ$ via the DPC connected at the input of the PDPM. The output of the PDPM was connected to the test PBS and the power out of its output ports was monitored. This time, to reiterate, the RF delay between the PMs was imbalanced. Figure 4.21 shows the results of these classical light polarization stability measurements. The power out of both ports of the test PBS (port A and port B) is recorded for 5 minutes at each polarization setting and the polarization is kept constant at each setting.

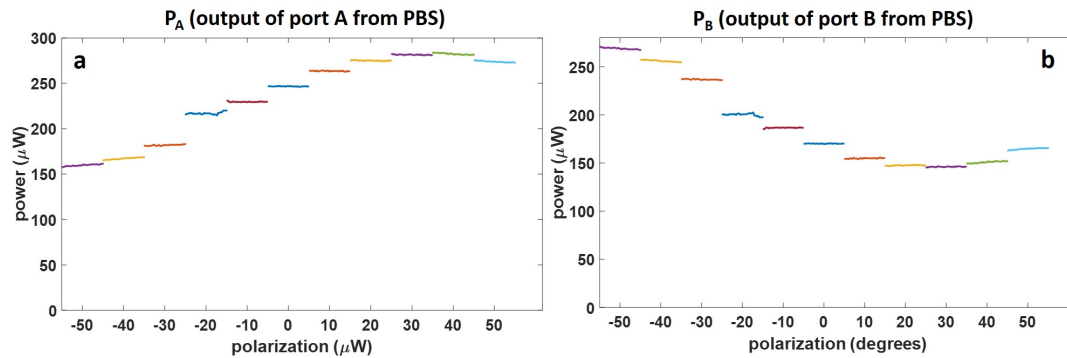


Fig. 4.21.: Polarization stability of the classical light through the PDPM with the PMs on and RF delay (purposefully) imbalanced. Polarization is swept from -50° to $+50^\circ$ in 10° increments (measured and controlled via DPC at input of PDPM). Power is recorded out of each port of the test PBS for 5 minutes at each polarization setting. a – port A of the test PBS. b – port B of the test PBS. Notice that in this iteration, there exists less extinction between the two output ports of the test PBS.

Comparing the results between output ports of the test PBS in the case when the RF delay is balanced, figure 4.20, to the case when the RF delay is imbalanced, figure 4.21, a reduction in extinction is observed. In the case when the RF delay is balanced depicted in figure 4.20, for port A the maximum power recorded (on average over the 5 minute measurement) was $355.04 \mu\text{W}$ and the minimum power recorded was $39.74 \mu\text{W}$. For port B the maximum power recorded was $330.23 \mu\text{W}$ and the minimum power recorded was $43.40 \mu\text{W}$. In the case when the RF delay is imbalanced,

shown in figure 4.21, the maximum power recorded out of port A was $268.84 \mu\text{W}$, and the minimum power recorded was $146.02 \mu\text{W}$. For port B the maximum power recorded was $282.47 \mu\text{W}$, and the minimum power recorded was $159.79 \mu\text{W}$. From these recorded power values, it is clear that the power extinction out of the test PBS is greater when the RF delay is balanced.

It is hypothesized that when the RF delay is different between the individual PMs of the PDPM, the RF sinusoids reach their respective PMs at different times. This means that light in the different paths of the PDPM incur a phase difference due to this delay in the RF signal. When the light recombines at the output of the PDPM, the phase between the light in each path is manifested as a polarization transformation out of the PDPM. This polarization transformation is attributed to the reduced power extinction out of the test PBS, depicted in figure 4.21. If the RF delay between the individual PMs is balanced, then the phase difference will not be incurred, and the phase transformation manifested as a reduction in extinction between the ports of the PBS, will not occur, see figure 4.20.

It was previously stated that in order to preserve indistinguishability between the paths of the PDPM, the optical insertion loss and path lengths must be balanced, and so too the modulation indices and RF delay between the individual PMs must be balanced. This is done so that no information can be observed as to what path the photons take through the PDPM. Therefore, a balanced PDPM, both optically and electrically, is the default state at which the PDPM will be operated. The RF delay dependent polarization transformation evident in figure 4.21 is an interesting phenomenon that allowed for the understanding of what effect the RF delay has on the output polarization state. Whether this unbalanced RF state is detrimental to the frequency-bin entanglement measurement is not known. The next step is for the actively stabilized PDPM to be used in the projective measurements to show frequency-bin entanglement in a BFC.

It was shown, in this chapter, that the PDPM can perform phase modulation irrespective of the polarization state of classical light, figure 4.4, irrespective of the

polarization state of entangled photons, figure 4.6, and irrespective of the polarization state between the frequency-bin pairs of the BFC, figure 4.7 and 4.10. Finally, active stabilization of the PDPM was demonstrated by propagating a stabilization laser (CW laser) backwards through the PDPM and using a PID controller to minimize an error signal. This was performed to ensure the polarization stability of the output photons. The next step is to perform frequency-bin entanglement measurements with the actively stabilized PDPM, and to demonstrate that the power of the PDPM lies in its ability to perform phase modulation on bi-photons hyperentangled in polarization and frequency.

Acknowledgement of Collaboration

The author was tasked with the classical stabilization of the PDPM. The other aspects of this work were a collaborative effort with colleague Navin Lingaraju.

5. CONCLUSION

5.1 Brief Summary

In this dissertation electro-optic phase modulation was used to generate high repeat electro-optic frequency combs. The goal of the work was to broaden these so-called EO combs in the spectral domain. Chapter 1 of this work offers a brief review of methods for achieving this spectral broadening. In chapter 2, the nonlinear optical loop mirror (NOLM) is introduced. The NOLM is an all fiber device that allows for broadening the spectrum of the electro-optic frequency comb to a bandwidth of 40 nm with a spectral ripple, power variation among spectral lines, to be less than 10 dB. In chapter 3, this broadened electro-optic frequency comb was used as a reference comb in dual comb interferometry measurements to characterize the single-soliton Kerr-frequency comb generated in a silicon-nitride microresonator. This dual comb interferometry technique allowed for rapid characterization of the single soliton with low average power out of the ring resonator. In chapter 4, electro-optic phase modulation is used to show the entanglement in a biphoton frequency comb. The fact that commercial standalone phase modulators are polarization dependent was demonstrated, and to circumvent this, the polarization diversity phase modulator (PDPM) was introduced. The polarization diversity of the PDPM was demonstrated both classically and in the quantum regime. The final aspect of the PDPM project, in this work, was to actively stabilize the interferometer to ensure polarization stability out of the PDPM.

5.2 Future Outlook

Chapter 2 is matured results, and there are no experiments that can be done to move this forward. However, it is the hope of the author of this dissertation that colleagues at the lab will find this useful and continue to use it in future experiments, specifically with work related to measurements introduced in chapter 3.

An interesting extension of the dual comb interferometry technique presented in chapter 3 is characterizing dark pulses generated in normal dispersion microresonators, an example spectrum being shown in figure 5.1. In 2015, Xue et al. demonstrated mode-locking transitions, as those reported for bright soliton generation, and the generation of dark pulses in a normal dispersion SiN ring resonator [138].

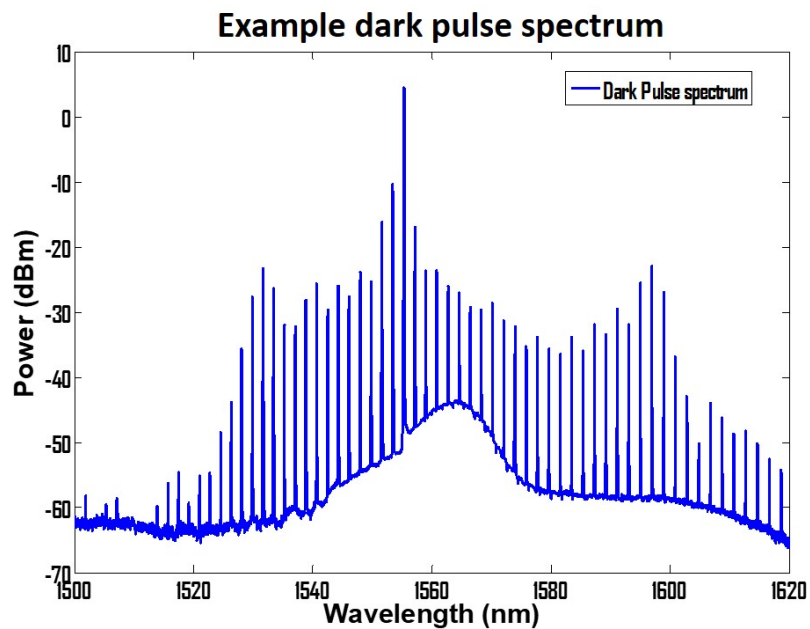


Fig. 5.1.: Example of dark pulse spectrum generated from a normal dispersion microresonator.

The goal is to measure the phase of the dark pulse, the same way the phase of the single bright soliton was retrieved in [102]. This would require only a slight modification to the setup presented in chapter 3, the modification being the center

wavelength and rep-rate of the reference pulse. But this again shows the versatility of broadened EO comb.

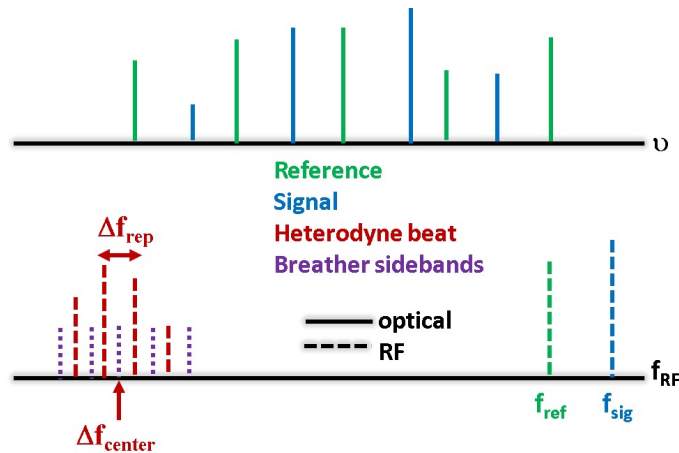


Fig. 5.2.: We expect to visualize the breathing dynamics of the dark breather by observing (purple) sidebands on the retrieved RF comb from the Dual Comb EFXC measurement.

An extension of the dark pulses in normal dispersion is the dark breather. Breathers are localized waves that are periodic in time and space. They have been reported in optical fibers [139], but Kerr combs are also attractive for the studying of breathers, due to microresonators providing an essentially infinite propagation distance in which breathers can be sampled every round trip. And, the wide frequency spacing offered by the Kerr combs allows for ease of separation of individual comb lines to study their breathing dynamics [140].

Capturing the breathing dynamics is the goal for the next iteration of the dual comb EFXC measurements. The measurements will allow us to reconstruct the time domain waveform of the breather. This is of interest as no one has demonstrated this experimentally. And to confirm that breathing is being observed, the RF comb returned by the measurements will be analyzed for the presence of sidebands; a cartoon of this is depicted in figure 5.2. These sidebands will be adjacent to the beating lines (RF comb lines) and spaced 280 MHz away i.e. at the breathing frequency.

In regard to the PDPM presented in chapter 4, because it can operate on photons irrespective of their polarization state, the PDPM can potentially be used in schemes where information is encoded in both the polarization and frequency-bin degrees of freedom (DoF). For example, such encoding has been carried out using the polarization and transverse spatial modes DoF [141]. To date, such demonstrations have not been carried out using polarization and frequency-bin – both of which being compatible with optical fiber. Our group has previously implemented communication protocols where information was encoded in the frequency DoF of entangled photons using Fourier transform pulse shapers [142]. With the PDPM, we plan to build on this work by encoding information in both polarization and frequency-bin. In such an arrangement, the PDPM would measure the relative phase between frequency bins without altering neither their polarization nor any information encoded in this DoF. The PDPM could also be used in more complex schemes in which one needs to carry out projective measurements in the frequency domain on photons that are also entangled in polarization.

Lastly, colleagues at ARL want these PDPMs to be in a “plug and play” box for future delivery. Therefore, smaller, and preferably more affordable, components will need to be used. One of these components is the lock-box used in the current active stabilization technique. An alternative to this, is using an FPGA (Red-Pitaya) with a built in PID controller. This task will be given to an undergraduate summer research scholar that our lab will have the privilege of mentoring. These are the last projects the author will focus on, as his time here comes to an end.

REFERENCES

REFERENCES

- [1] T. Udem, R. Holzwarth, and T. W. Hänsch, “Optical frequency metrology,” *Nature*, vol. 416, no. 6877, p. 233, 2002.
- [2] D. J. Jones, S. A. Diddams, J. K. Ranka, A. Stentz, R. S. Windeler, J. L. Hall, and S. T. Cundiff, “Carrier-envelope phase control of femtosecond mode-locked lasers and direct optical frequency synthesis,” *Science*, vol. 288, no. 5466, pp. 635–639, 2000.
- [3] R. Holzwarth, T. Udem, T. W. Hänsch, J. Knight, W. Wadsworth, and P. S. J. Russell, “Optical frequency synthesizer for precision spectroscopy,” *Physical review letters*, vol. 85, no. 11, p. 2264, 2000.
- [4] S. A. Diddams, D. J. Jones, J. Ye, S. T. Cundiff, J. L. Hall, J. K. Ranka, R. S. Windeler, R. Holzwarth, T. Udem, and T. Hänsch, “Direct link between microwave and optical frequencies with a 300 thz femtosecond laser comb,” *Physical Review Letters*, vol. 84, no. 22, p. 5102, 2000.
- [5] N. R. Newbury, “Searching for applications with a fine-tooth comb,” *Nature photonics*, vol. 5, no. 4, pp. 186–188, 2011.
- [6] J. Ye and S. T. Cundiff, *Femtosecond optical frequency comb: principle, operation and applications*. Springer Science & Business Media, 2005.
- [7] A. Bartels, D. Heinecke, and S. A. Diddams, “10-ghz self-referenced optical frequency comb,” *Science*, vol. 326, no. 5953, pp. 681–681, 2009.
- [8] S. T. Cundiff and A. M. Weiner, “Optical arbitrary waveform generation,” *Nature Photonics*, vol. 4, no. 11, p. 760, 2010.
- [9] V. Torres-Company and A. M. Weiner, “Optical frequency comb technology for ultra-broadband radio-frequency photonics,” *Laser & Photonics Reviews*, vol. 8, no. 3, pp. 368–393, 2014.
- [10] J. Hecht. (2012) Photonic frontiers: Frequency combs: Frequency combs make their way to the masses. [Online]. Available: <https://www.laserfocusworld.com/articles/print/volume-48/issue-01/features/frequency-combs-make-their-way-to-the-masses.html>
- [11] J. L. Hall, “Nobel lecture: Defining and measuring optical frequencies,” *Reviews of Modern Physics*, vol. 78, no. 4, p. 1279, 2006.
- [12] T. W. Hänsch, “Einstein lecture—passion for precision,” *Annalen der Physik*, vol. 15, no. 9, pp. 627–652, 2006.
- [13] E. Gordon and J. Rigden, “The fabry-perot electrooptic modulator,” *Bell Labs Technical Journal*, vol. 42, no. 1, pp. 155–179, 1963.

- [14] T. Kobayashi, T. Sueta, Y. Cho, and Y. Matsuo, "High-repetition-rate optical pulse generator using a fabry-perot electro-optic modulator," *Applied Physics Letters*, vol. 21, no. 8, pp. 341–343, 1972.
- [15] T. Kobayashi, H. Yao, K. Amano, Y. Fukushima, A. Morimoto, and T. Sueta, "Optical pulse compression using high-frequency electrooptic phase modulation," *IEEE journal of quantum electronics*, vol. 24, no. 2, pp. 382–387, 1988.
- [16] M. Fujiwara, M. Teshima, J.-i. Kani, H. Suzuki, N. Takachio, and K. Iwatsuki, "Optical carrier supply module using flattened optical multicarrier generation based on sinusoidal amplitude and phase hybrid modulation," *Journal of light-wave technology*, vol. 21, no. 11, pp. 2705–2714, 2003.
- [17] Y. Liu, A. J. Metcalf, R. Wu, L. Fan, L. T. Varghese, M. Qi, A. M. Weiner *et al.*, "Bandwidth scaling of a phase-modulated continuous-wave comb through four-wave mixing in a silicon nano-waveguide," *Optics letters*, vol. 39, no. 22, pp. 6478–6481, 2014.
- [18] A. Weiner, *Ultrafast optics*. John Wiley & Sons, 2011, vol. 72.
- [19] G. P. Agrawal, *Fiber-optic communication systems*. John Wiley & Sons, 2012, vol. 222.
- [20] K. R. Tamura, H. Kuhota, and M. Nakazawa, "Fundamentals of stable continuum generation at high repetition rates," *IEEE journal of quantum electronics*, vol. 36, no. 7, pp. 773–779, 2000.
- [21] Y. Ozeki, S. Takasaka, M. Sakano, and S. Namiki, "Repetition rate variable and wavelength-tunable picosecond optical pulse source employing square-wave-driven intensity modulator and comb-like profiled fiber," *IEEE photonics technology letters*, vol. 17, no. 12, pp. 2736–2738, 2005.
- [22] I. Morohashi, T. Sakamoto, H. Sotobayashi, T. Kawanishi, I. Hosako, and M. Tsuchiya, "Widely repetition-tunable 200 fs pulse source using a mach-zehnder-modulator-based flat comb generator and dispersion-flattened dispersion-decreasing fiber," *Optics letters*, vol. 33, no. 11, pp. 1192–1194, 2008.
- [23] C.-B. Huang, S.-G. Park, D. E. Leaird, and A. M. Weiner, "Nonlinearly broadened phase-modulated continuous-wave laser frequency combs characterized using dpsk decoding," *Optics express*, vol. 16, no. 4, pp. 2520–2527, 2008.
- [24] Z. Jiang, C.-B. Huang, D. E. Leaird, and A. M. Weiner, "Optical arbitrary waveform processing of more than 100 spectral comb lines," *Nature Photonics*, vol. 1, no. 8, p. 463, 2007.
- [25] R. W. Boyd, *Nonlinear optics*. Academic press, 2003.
- [26] A. M. Clarke, D. G. Williams, M. A. Roelens, and B. J. Eggleton, "Reconfigurable optical pulse generator employing a fourier-domain programmable optical processor," *Journal of Lightwave Technology*, vol. 28, no. 1, pp. 97–103, 2010.
- [27] A. J. Metcalf, C. D. Fredrick, R. C. Terrien, S. B. Papp, and S. A. Diddams, "30 ghz frequency comb spanning 160 thz in the near-infrared," in *Lasers and Electro-Optics (CLEO), 2017 Conference on*. IEEE, 2017, pp. 1–1.

- [28] S. Pitois, C. Finot, J. Fatome, B. Sinardet, and G. Millot, "Generation of 20-ghz picosecond pulse trains in the normal and anomalous dispersion regimes of optical fibers," *Optics Communications*, vol. 260, no. 1, pp. 301–306, 2006.
- [29] F. Parmigiani, C. Finot, K. Mukasa, M. Ibsen, M. A. Roelens, P. Petropoulos, and D. J. Richardson, "Ultra-flat spm-broadened spectra in a highly nonlinear fiber using parabolic pulses formed in a fiber bragg grating," *Optics Express*, vol. 14, no. 17, pp. 7617–7622, 2006.
- [30] W. Tomlinson, R. H. Stolen, and A. M. Johnson, "Optical wave breaking of pulses in nonlinear optical fibers," *Optics letters*, vol. 10, no. 9, pp. 457–459, 1985.
- [31] C. Finot, B. Kibler, L. Provost, and S. Wabnitz, "Beneficial impact of wave-breaking for coherent continuum formation in normally dispersive nonlinear fibers," *JOSA B*, vol. 25, no. 11, pp. 1938–1948, 2008.
- [32] V. Supradeepa and A. M. Weiner, "Bandwidth scaling and spectral flatness enhancement of optical frequency combs from phase-modulated continuous-wave lasers using cascaded four-wave mixing," *Optics letters*, vol. 37, no. 15, pp. 3066–3068, 2012.
- [33] G. A. Seffler and K.-I. Kitayama, "Frequency comb generation by four-wave mixing and the role of fiber dispersion," *Journal of lightwave technology*, vol. 16, no. 9, pp. 1596–1605, 1998.
- [34] T. Yang, J. Dong, S. Liao, D. Huang, and X. Zhang, "Comparison analysis of optical frequency comb generation with nonlinear effects in highly nonlinear fibers," *Optics express*, vol. 21, no. 7, pp. 8508–8520, 2013.
- [35] B. P.-P. Kuo, E. Myslivets, N. Alic, and S. Radic, "Wavelength multicasting via frequency comb generation in a bandwidth-enhanced fiber optical parametric mixer," *Journal of Lightwave Technology*, vol. 29, no. 23, pp. 3515–3522, 2011.
- [36] E. Myslivets, B. P. Kuo, N. Alic, and S. Radic, "Generation of wideband frequency combs by continuous-wave seeding of multistage mixers with synthesized dispersion," *Optics express*, vol. 20, no. 3, pp. 3331–3344, 2012.
- [37] X. Yang and P. Petropoulos, "An ultra-flat frequency comb generated using nonlinear broadening and adaptive pulse shaping," in *Optical Fiber Communication Conference*. Optical Society of America, 2012, pp. OW4H–5.
- [38] T. J. Kippenberg, R. Holzwarth, and S. A. Diddams, "Microresonator-based optical frequency combs," *Science*, vol. 332, no. 6029, pp. 555–559, 2011.
- [39] B. Stern, X. Ji, Y. Okawachi, A. L. Gaeta, and M. Lipson, "Fully integrated ultra-low power kerr comb generation," *arXiv preprint arXiv:1804.00357*, 2018.
- [40] J. Liu, A. S. Raja, M. Karpov, B. Ghadiani, M. H. Pfeiffer, N. J. Engelsen, H. Guo, M. Zervas, and T. J. Kippenberg, "Ultralow-power photonic chip-based soliton frequency combs," *arXiv preprint arXiv:1805.00069*, 2018.
- [41] J. S. Levy, A. Gondarenko, M. A. Foster, A. C. Turner-Foster, A. L. Gaeta, and M. Lipson, "CMOS-compatible multiple-wavelength oscillator for on-chip optical interconnects," *Nature photonics*, vol. 4, no. 1, p. 37, 2010.

- [42] K. J. Vahala, "Optical microcavities," *Nature*, vol. 424, no. 6950, pp. 839–846, 2003.
- [43] W. Bogaerts, P. De Heyn, T. Van Vaerenbergh, K. De Vos, S. Kumar Selvaraja, T. Claes, P. Dumon, P. Bienstman, D. Van Thourhout, and R. Baets, "Silicon microring resonators," *Laser & Photonics Reviews*, vol. 6, no. 1, pp. 47–73, 2012.
- [44] P. Del'Haye, A. Schliesser, O. Arcizet, T. Wilken, R. Holzwarth, and T. J. Kippenberg, "Optical frequency comb generation from a monolithic microresonator," *Nature*, vol. 450, no. 7173, p. 1214, 2007.
- [45] V. B. Braginsky, M. L. Gorodetsky, and V. S. Ilchenko, "Quality-factor and nonlinear properties of optical whispering-gallery modes," *Physics Letters A*, vol. 137, no. 7-8, pp. 393–397, 1989.
- [46] I. H. Agha, Y. Okawachi, M. A. Foster, J. E. Sharping, and A. L. Gaeta, "Four-wave-mixing parametric oscillations in dispersion-compensated high-Q silica microspheres," *Physical Review A - Atomic, Molecular, and Optical Physics*, vol. 76, no. 4, pp. 1–4, 2007.
- [47] P. Del'Haye, O. Arcizet, A. Schliesser, R. Holzwarth, and T. J. Kippenberg, "Full stabilization of a microresonator-based optical frequency comb," *Physical Review Letters*, vol. 101, no. 5, pp. 1–4, 2008.
- [48] L. Razzari, D. Duchesne, M. Ferrera, R. Morandotti, S. Chu, B. E. Little, and D. J. Moss, "CMOS-compatible integrated optical hyper-parametric oscillator," *Nature Photonics*, vol. 4, no. 1, pp. 41–45, 2010. [Online]. Available: <http://dx.doi.org/10.1038/nphoton.2009.236>
- [49] P. Del'Haye, T. Herr, E. Gavartin, M. L. Gorodetsky, R. Holzwarth, and T. J. Kippenberg, "Octave spanning tunable frequency comb from a microresonator," *Physical Review Letters*, vol. 107, no. 6, pp. 1–4, 2011.
- [50] A. A. Savchenkov, A. B. Matsko, V. S. Ilchenko, I. Solomatine, D. Seidel, and L. Maleki, "Tunable optical frequency comb with a crystalline whispering gallery mode resonator," *Physical Review Letters*, vol. 101, no. 9, pp. 1–4, 2008.
- [51] I. S. Grudinin, N. Yu, and L. Maleki, "Generation of optical frequency combs with a CaF₂ resonator," *Optics Letters*, vol. 34, no. 7, p. 878, 2009. [Online]. Available: <https://www.osapublishing.org/abstract.cfm?URI=ol-34-7-878>
- [52] A. A. Savchenkov, A. B. Matsko, W. Liang, V. S. Ilchenko, D. Seidel, and L. Maleki, "Kerr combs with selectable central frequency," *Nature Photonics*, vol. 5, no. 5, pp. 293–296, 2011.
- [53] W. Liang, A. A. Savchenkov, A. B. Matsko, V. S. Ilchenko, D. Seidel, and L. Maleki, "Generation of near-infrared frequency combs from a MgF₂ whispering gallery mode resonator," *Optics letters*, vol. 36, no. 12, pp. 2290–2292, 2011.
- [54] C. Y. Wang, T. Herr, P. Del'Haye, A. Schliesser, J. Hofer, R. Holzwarth, T. W. Hänsch, N. Picqué, and T. J. Kippenberg, "Mid-infrared optical frequency combs at 2.5 μm based on crystalline microresonators," *Nature Communications*, vol. 4, 2013.

- [55] I. S. Grudinin, L. Baumgartel, and N. Yu, “Frequency comb from a microresonator with engineered spectrum,” *Optics express*, vol. 20, no. 6, pp. 6604–6609, 2012.
- [56] S. B. Papp and S. A. Diddams, “Spectral and temporal characterization of a fused-quartz-microresonator optical frequency comb,” *Physical Review A*, vol. 84, no. 5, p. 053833, 2011.
- [57] F. Ferdous, H. Miao, D. E. Leaird, K. Srinivasan, J. Wang, L. Chen, L. T. Varghese, and A. M. Weiner, “Spectral line-by-line pulse shaping of on-chip microresonator frequency combs,” *Nature Photonics*, vol. 5, no. 12, p. 770, 2011.
- [58] M. A. Foster, J. S. Levy, O. Kuzucu, K. Saha, M. Lipson, and A. L. Gaeta, “Silicon-based monolithic optical frequency comb source,” *Optics Express*, vol. 19, no. 15, pp. 14 233–14 239, 2011.
- [59] T. Herr, K. Hartinger, J. Riemensberger, C. Wang, E. Gavartin, R. Holzwarth, M. L. Gorodetsky, and T. Kippenberg, “Universal formation dynamics and noise of kerr-frequency combs in microresonators,” *Nature Photonics*, vol. 6, no. 7, p. 480, 2012.
- [60] I. Coddington, N. Newbury, and W. Swann, “Dual-comb spectroscopy,” *Optica*, vol. 3, no. 4, p. 414, 2016. [Online]. Available: <https://www.osapublishing.org/abstract.cfm?URI=optica-3-4-414>
- [61] I. Coddington, W. C. Swann, L. Nenadovic, and N. R. Newbury, “Rapid and precise absolute distance measurements at long range,” *Nature Photonics*, vol. 3, no. 6, pp. 351–356, 2009.
- [62] V. Michaud-Belleau, J. Roy, S. Potvin, J.-R. Carrier, L.-S. Verret, M. Charlebois, J. Genest, and C. N. Allen, “Whispering gallery mode sensing with a dual frequency comb probe,” *Optics Express*, vol. 20, no. 3, p. 3066, 2012. [Online]. Available: <https://www.osapublishing.org/abstract.cfm?URI=oe-20-3-3066>
- [63] N. Kuse, A. Ozawa, and Y. Kobayashi, “Static FBG strain sensor with high resolution and large dynamic range by dual-comb spectroscopy,” *Optics Express*, vol. 21, no. 9, p. 11141, 2013. [Online]. Available: <https://www.osapublishing.org/oe/abstract.cfm?uri=oe-21-9-11141>
- [64] J. L. Peng, T. A. Liu, and R. H. Shu, “Optical frequency counter based on two mode-locked fiber laser combs,” *Applied Physics B: Lasers and Optics*, vol. 92, no. 4, pp. 513–518, 2008.
- [65] F. R. Giorgetta, I. Coddington, E. Baumann, W. C. Swann, and N. R. Newbury, “Fast high-resolution spectroscopy of dynamic continuous-wave laser sources,” *Nature Photonics*, vol. 4, no. 12, pp. 853–857, 2010. [Online]. Available: <http://dx.doi.org/10.1038/nphoton.2010.228>
- [66] I. Coddington, F. R. Giorgetta, E. Baumann, W. C. Swann, and N. R. Newbury, “Characterizing fast arbitrary cw waveforms with 1500 thz/s instantaneous chirps,” *IEEE Journal on Selected Topics in Quantum Electronics*, vol. 18, no. 1, pp. 228–238, 2012.

- [67] S. Boudreau and J. Genest, "Referenced passive spectroscopy using dual frequency combs." *Optics express*, vol. 20, no. 7, pp. 7375–87, 2012. [Online]. Available: <http://www.osapublishing.org/viewmedia.cfm?uri=oe-20-7-7375&seq=0&html=true>
- [68] A. Klee, J. Davila-Rodriguez, C. Williams, and P. J. Delfyett, "Characterization of semiconductor-based optical frequency comb sources using generalized multiheterodyne detection," *IEEE Journal on Selected Topics in Quantum Electronics*, vol. 19, no. 4, 2013.
- [69] V. Durán, S. Tainta, and V. Torres-Company, "Ultrafast electrooptic dual-comb interferometry," *Optics Express*, vol. 23, no. 23, p. 30557, 2015. [Online]. Available: <https://www.osapublishing.org/abstract.cfm?URI=oe-23-23-30557>
- [70] F. Ferdous, D. E. Leaird, C.-B. Huang, and A. Weiner, "Dual-comb electric-field cross-correlation technique for optical arbitrary waveform characterization." *Optics letters*, vol. 34, no. 24, pp. 3875–7, 2009. [Online]. Available: <http://www.ncbi.nlm.nih.gov/pubmed/20016643>
- [71] A. Klee, M. Bagnell, and P. J. Delfyett, "Self - referenced Spectral Phase Retrieval of Dissimilar Optical Frequency Combs via Multiheterodyne Detection," vol. 2, pp. 491–492, 2012.
- [72] T. Yasui, Y. Kabetani, E. Saneyoshi, S. Yokoyama, and T. Araki, "Terahertz frequency comb by multifrequency-heterodyning photoconductive detection for high-accuracy, high-resolution terahertz spectroscopy," *Applied Physics Letters*, vol. 88, no. 24, pp. 86–89, 2006.
- [73] I. Coddington, W. C. Swann, and N. R. Newbury, "Coherent multiheterodyne spectroscopy using stabilized optical frequency combs," *Physical Review Letters*, vol. 100, no. 1, pp. 11–14, 2008.
- [74] A. M. Zolot, F. R. Giorgetta, E. Baumann, J. W. Nicholson, W. C. Swann, I. Coddington, and N. R. Newbury, "Direct-comb molecular spectroscopy with accurate, resolved comb teeth over 43 THz." *Optics letters*, vol. 37, no. 4, pp. 638–40, 2012. [Online]. Available: <http://www.ncbi.nlm.nih.gov/pubmed/22344132>
- [75] S. Okubo, K. Iwakuni, H. Inaba, K. Hosaka, A. Onae, H. Sasada, and F. L. Hong, "Ultra-broadband dual-comb spectroscopy across 1.0-1.9 μm ," *Applied Physics Express*, vol. 8, no. 8, 2015.
- [76] F. Keilmann, C. Gohle, and R. Holzwarth, "Time-domain mid-infrared frequency-comb spectrometer," vol. 29, no. 13, pp. 1542–1544, 2004.
- [77] A. Schliesser, M. Brehm, F. Keilmann, and D. W. van der Weide, "Frequency-comb infrared spectrometer for rapid, remote chemical sensing." *Optics express*, vol. 13, no. 22, pp. 9029–9038, 2005.
- [78] T. Yasui, E. Saneyoshi, and T. Araki, "Asynchronous optical sampling terahertz time-domain spectroscopy for ultrahigh spectral resolution and rapid data acquisition," *Applied Physics Letters*, vol. 87, no. 6, pp. 1–4, 2005.

- [79] S. Lee and B. Widiyatmoko, "Ultrahigh scanning speed optical coherence tomography using optical frequency comb generators," *Japanese Journal of ...*, vol. 40, no. 8, pp. 878–880, 2001. [Online]. Available: <http://adsabs.harvard.edu/abs/2001JaJAP..40..878L>
- [80] M. Brehm, A. Schliesser, and F. Keilmann, "Spectroscopic near-field microscopy using frequency combs in the mid-infrared," *Optics Express*, vol. 14, no. 23, p. 11222, 2006. [Online]. Available: <https://www.osapublishing.org/oe/abstract.cfm?uri=oe-14-23-11222>
- [81] E. Baumann, F. R. Giorgetta, W. C. Swann, A. M. Zolot, I. Coddington, and N. R. Newbury, "Spectroscopy of the methane ν_3 band with an accurate mid-infrared coherent dual-comb spectrometer," *Physical Review A - Atomic, Molecular, and Optical Physics*, vol. 84, no. 6, 2011.
- [82] A. M. Zolot, F. R. Giorgetta, E. Baumann, W. C. Swann, I. Coddington, and N. R. Newbury, "Broad-band frequency references in the near-infrared: Accurate dual comb spectroscopy of methane and acetylene," *Journal of Quantitative Spectroscopy and Radiative Transfer*, vol. 118, pp. 26–39, 2013. [Online]. Available: <http://dx.doi.org/10.1016/j.jqsrt.2012.11.024>
- [83] M. Godbout, J.-D. Deschênes, and J. Genest, "Spectrally resolved laser ranging with frequency combs," *Opt Express*, vol. 18, no. 15, pp. 15 981–15 989, 2010. [Online]. Available: <http://www.ncbi.nlm.nih.gov/pubmed/20720982>
- [84] S. Boudreau, S. Levasseur, C. Perilla, S. Roy, and J. Genest, "Chemical detection with hyperspectral lidar using dual frequency combs," *Optics Express*, vol. 21, no. 6, p. 7411, 2013. [Online]. Available: <https://www.osapublishing.org/oe/abstract.cfm?uri=oe-21-6-7411>
- [85] F. Zhu, A. Bicer, R. Askar, J. Bounds, A. A. Kolomenskii, V. Kelesides, M. Amani, and H. A. Schuessler, "Mid-infrared dual frequency comb spectroscopy based on fiber lasers for the detection of methane in ambient air," *Laser Physics Letters*, vol. 12, no. 9, p. 95701, 2015. [Online]. Available: <http://dx.doi.org/10.1088/1612-2011/12/9/095701>
- [86] F. R. Giorgetta, G. B. Rieker, E. Baumann, W. C. Swann, L. C. Sinclair, J. Kofler, I. Coddington, and N. R. Newbury, "Broadband Phase Spectroscopy over Turbulent Air Paths," *Physical Review Letters*, vol. 115, no. 10, pp. 1–5, 2015.
- [87] T. Ideguchi, B. Bernhardt, G. Guelachvili, T. W. Hänsch, and N. Picqué, "Raman-induced Kerr-effect dual-comb spectroscopy," *Optics Letters*, vol. 37, no. 21, pp. 4498–4500, 2012.
- [88] T. Ideguchi, S. Holzner, B. Bernhardt, G. Guelachvili, N. Picqué, and T. W. Hänsch, "Coherent Raman spectro-imaging with laser frequency combs," *Nature*, vol. 502, no. 7471, pp. 355–358, 2013.
- [89] A. Hipke, S. A. Meek, T. Ideguchi, T. W. Hänsch, and N. Picqué, "Broadband Doppler-limited two-photon and stepwise excitation spectroscopy with laser frequency combs," *Physical Review A - Atomic, Molecular, and Optical Physics*, vol. 90, no. 1, pp. 1–5, 2014.

- [90] P. Imany, O. D. Odele, J. A. Jaramillo-Villegas, D. E. Leaird, and A. M. Weiner, “Characterization of coherent quantum frequency combs using electro-optic phase modulation,” *Physical Review A*, vol. 97, no. 1, pp. 1–5, 2018.
- [91] M. Kues, C. Reimer, P. Roztocky, L. R. Cortés, S. Sciara, B. Wetzels, Y. Zhang, A. Cino, S. T. Chu, B. E. Little, D. J. Moss, L. Caspani, J. Azaña, and R. Morandotti, “On-chip generation of high-dimensional entangled quantum states and their coherent control,” *Nature*, vol. 546, no. 7660, pp. 622–626, 2017. [Online]. Available: <http://dx.doi.org/10.1038/nature22986>
- [92] P. Imany, J. A. Jaramillo-Villegas, O. D. Odele, K. Han, D. E. Leaird, J. M. Lukens, P. Lougovski, M. Qi, and A. M. Weiner, “50-ghz-spaced comb of high-dimensional frequency-bin entangled photons from an on-chip silicon nitride microresonator,” *Optics Express*, vol. 26, no. 2, pp. 1825–1840, 2018.
- [93] V. Ataie, E. Myslivets, B. P. P. Kuo, N. Alic, and S. Radic, “Spectrally equalized frequency comb generation in multistage parametric mixer with nonlinear pulse shaping,” *Journal of Lightwave Technology*, vol. 32, no. 4, pp. 840–846, 2014.
- [94] N. J. Doran and D. Wood, “Nonlinear-optical loop mirror.” *Optics letters*, vol. 13, no. 1, pp. 56–58, 1988.
- [95] M. Jinno and T. Matsumoto, “Ultrafast all-optical logic operations in a nonlinear Sagnac interferometer with two control beams.” *Optics letters*, vol. 16, no. 4, pp. 220–2, 1991. [Online]. Available: <http://www.ncbi.nlm.nih.gov/pubmed/19773888>
- [96] I. Duling, “Subpicosecond all-fibre erbium laser,” *Electronics Letters*, vol. 27, no. 6, p. 544, 1991. [Online]. Available: http://digital-library.theiet.org/content/journals/10.1049/el_19910342
- [97] K. Smith, N. J. Doran, and P. G. Wigley, “Pulse shaping, compression, and pedestal suppression employing a nonlinear-optical loop mirror.” *Optics letters*, vol. 15, no. 22, pp. 1294–1296, 1990.
- [98] M. E. Fermann, F. Haberl, M. Hofer, and H. Hochreiter, “Nonlinear amplifying loop mirror,” *Optics Letters*, vol. 15, no. 13, p. 752, 1990. [Online]. Available: <http://www.osapublishing.org/viewmedia.cfm?uri=ol-15-13-752&seq=0&html=true>
- [99] I. N. Duling, C. J. Chen, P. K. Wai, and C. R. Menyuk, “Operation of a Nonlinear Loop Mirror in a Laser Cavity,” *IEEE Journal of Quantum Electronics*, vol. 30, no. 1, pp. 194–199, 1994.
- [100] A. M. Weiner, “Femtosecond pulse shaping using spatial light modulators,” *Review of scientific instruments*, vol. 71, no. 5, pp. 1929–1960, 2000.
- [101] A. J. Metcalf, V. Torres-Company, D. E. Leaird, and A. M. Weiner, “High-power broadly tunable electrooptic frequency comb generator,” *IEEE Journal of Selected Topics in Quantum Electronics*, vol. 19, no. 6, pp. 231–236, 2013.
- [102] Z. Kong, C. Bao, O. Sandoval, B. Liu, M. Qi, and A. M. Weiner, “All-linear phase retrieval of a single-soliton kerr comb,” in *CLEO: Science and Innovations*. Optical Society of America, 2018, pp. STh4N–4.

- [103] Z. Kong, C. Bao, O. E. Sandoval, B. Liu, C. Wang, J. A. Jaramillo-Villegas, M. Qi, and A. M. Weiner, “Characterizing pump line phase offset of a single-soliton kerr comb by dual comb interferometry,” *Optics letters*, vol. 44, no. 6, pp. 1460–1463, 2019.
- [104] F. Ferdous, H. Miao, P.-H. Wang, D. E. Leaird, K. Srinivasan, L. Chen, V. Aksyuk, and A. M. Weiner, “Probing coherence in microcavity frequency combs via optical pulse shaping,” *Optics express*, vol. 20, no. 19, pp. 21 033–21 043, 2012.
- [105] K. Saha, Y. Okawachi, B. Shim, J. S. Levy, R. Salem, A. R. Johnson, M. A. Foster, M. R. Lamont, M. Lipson, and A. L. Gaeta, “Modelocking and femtosecond pulse generation in chip-based frequency combs,” *Optics express*, vol. 21, no. 1, pp. 1335–1343, 2013.
- [106] T. Herr, V. Brasch, J. D. Jost, C. Y. Wang, N. M. Kondratiev, M. L. Gorodetsky, and T. J. Kippenberg, “Temporal solitons in optical microresonators,” *Nature Photonics*, vol. 8, no. 2, p. 145, 2014.
- [107] V. Brasch, M. Geiselmann, T. Herr, G. Lihachev, M. H. Pfeiffer, M. L. Gorodetsky, and T. J. Kippenberg, “Photonic chip-based optical frequency comb using soliton cherenkov radiation,” *Science*, vol. 351, no. 6271, pp. 357–360, 2016.
- [108] X. Yi, Q.-F. Yang, K. Y. Yang, M.-G. Suh, and K. Vahala, “Soliton frequency comb at microwave rates in a high-q silica microresonator,” *Optica*, vol. 2, no. 12, pp. 1078–1085, 2015.
- [109] M. Karpov, H. Guo, A. Kordts, V. Brasch, M. Pfeiffer, M. Zervas, M. Geiselmann, and T. J. Kippenberg, “Raman induced soliton self-frequency shift in microresonator kerr frequency combs,” *arXiv preprint arXiv:1506.08767*, 2015.
- [110] M. H. Pfeiffer, A. Kordts, V. Brasch, M. Zervas, M. Geiselmann, J. D. Jost, and T. J. Kippenberg, “Photonic damascene process for integrated high-q microresonator based nonlinear photonics,” *Optica*, vol. 3, no. 1, pp. 20–25, 2016.
- [111] P.-H. Wang, J. A. Jaramillo-Villegas, Y. Xuan, X. Xue, C. Bao, D. E. Leaird, M. Qi, and A. M. Weiner, “Intracavity characterization of micro-comb generation in the single-soliton regime,” *Optics Express*, vol. 24, no. 10, p. 10890, 2016. [Online]. Available: <https://www.osapublishing.org/abstract.cfm?URI=oe-24-10-10890>
- [112] L. A. Lugiato and R. Lefever, “Spatial dissipative structures in passive optical systems,” *Physical review letters*, vol. 58, no. 21, p. 2209, 1987.
- [113] T. Herr, V. Brasch, J. D. Jost, I. Mirgorodskiy, G. Lihachev, M. L. Gorodetsky, and T. J. Kippenberg, “Mode spectrum and temporal soliton formation in optical microresonators,” *Physical Review Letters*, vol. 113, no. 12, pp. 1–6, 2014.
- [114] Y. H. Wen, M. R. Lamont, S. H. Strogatz, and A. L. Gaeta, “Self-organization in kerr-cavity-soliton formation in parametric frequency combs,” *Physical Review A*, vol. 94, no. 6, p. 063843, 2016.
- [115] S. Wabnitz, “Suppression of interactions in a phase-locked soliton optical memory,” *Optics letters*, vol. 18, no. 8, pp. 601–603, 1993.

- [116] A. B. Matsko, W. Liang, A. A. Savchenkov, D. Eliyahu, and L. Maleki, “Optical cherenkov radiation in overmoded microresonators,” *Optics letters*, vol. 41, no. 13, pp. 2907–2910, 2016.
- [117] C. Bao, Y. Xuan, D. E. Leaird, S. Wabnitz, M. Qi, and A. M. Weiner, “Spatial mode-interaction induced single soliton generation in microresonators,” *Optica*, vol. 4, no. 9, pp. 1011–1015, 2017.
- [118] O. E. Sandoval, N. B. Lingaraju, P. Imany, D. E. Leaird, M. Brodsky, and A. M. Weiner, “Polarization diversity phase modulator for measuring frequency-bin entanglement of a biphoton frequency comb in a depolarized channel,” *Optics Letters*, vol. 44, no. 7, pp. 1674–1677, 2019.
- [119] O. E. Sandoval, N. B. Lingaraju, P. Imany, D. Leaird, M. Brodsky, and A. M. Weiner, “Measuring frequency-bin entanglement in depolarized biphoton frequency combs,” in *CLEO: QELS-Fundamental Science*. Optical Society of America, 2019, pp. FTh1A–2.
- [120] —, “Polarization diversity phase modulator for measuring frequency-bin entanglement of biphoton frequency combs in a depolarized channel,” in *Frontiers in Optics / Laser Science*. Optical Society of America, 2018, p. JTu3A.69. [Online]. Available: <http://www.osapublishing.org/abstract.cfm?URI=FiO-2018-JTu3A.69>
- [121] J. M. Lukens and P. Lougovski, “Frequency-encoded photonic qubits for scalable quantum information processing,” *Optica*, vol. 4, no. 1, pp. 8–16, 2017.
- [122] L. Oslager, J. Cussey, A. T. Nguyen, P. Emplit, S. Massar, J. M. Merolla, and K. P. Huy, “Frequency-bin entangled photons,” *Physical Review A - Atomic, Molecular, and Optical Physics*, vol. 82, no. 1, pp. 1–7, 2010.
- [123] E. L. Wooten, K. M. Kissa, A. Yi-Yan, E. J. Murphy, D. A. Lafaw, P. F. Hallemeier, D. Maack, D. V. Attanasio, D. J. Fritz, G. J. McBrien *et al.*, “A review of lithium niobate modulators for fiber-optic communications systems,” *IEEE Journal of selected topics in Quantum Electronics*, vol. 6, no. 1, pp. 69–82, 2000.
- [124] C. Wang, M. Zhang, X. Chen, M. Bertrand, A. Shams-Ansari, S. Chandrasekhar, P. Winzer, and M. Lončar, “Integrated lithium niobate electro-optic modulators operating at cmos-compatible voltages,” *Nature*, vol. 562, no. 7725, p. 101, 2018.
- [125] H. Fukuda, K. Yamada, T. Tsuchizawa, T. Watanabe, H. Shinojima, and S.-i. Itabashi, “Silicon photonic circuit with polarization diversity,” *Optics express*, vol. 16, no. 7, pp. 4872–4880, 2008.
- [126] C. Haffner, D. Chelladurai, Y. Fedoryshyn, A. Josten, B. Baeuerle, W. Heni, T. Watanabe, T. Cui, B. Cheng, S. Saha *et al.*, “Low-loss plasmon-assisted electro-optic modulator,” *Nature*, vol. 556, no. 7702, p. 483, 2018.
- [127] M. Brodsky, E. C. George, C. Antonelli, and M. Shtaif, “Loss of polarization entanglement in a fiber-optic system with polarization mode dispersion in one optical path,” *Optics letters*, vol. 36, no. 1, pp. 43–45, 2011.

- [128] D. E. Jones, B. T. Kirby, and M. Brodsky, “Tuning quantum channels to maximize polarization entanglement for telecom photon pairs,” *npj Quantum Information*, vol. 4, no. 1, p. 58, 2018.
- [129] C. D. Poole, “Measurement of polarization-mode dispersion in single-mode fibers with random mode coupling,” *Optics Letters*, vol. 14, no. 10, p. 523, 1989. [Online]. Available: <https://www.osapublishing.org/abstract.cfm?URI=ol-14-10-523>
- [130] C. D. Poole and D. L. Favin, “Polarization-Mode Dispersion Measurements Based on Transmission Spectra Through a Polarizer,” *Journal of Lightwave Technology*, vol. 12, no. 6, pp. 917–929, 1994.
- [131] D. Collins, N. Gisin, N. Linden, S. Massar, and S. Popescu, “Bell inequalities for arbitrarily high dimensional systems,” no. 2, pp. 5–8, 2001. [Online]. Available: <http://arxiv.org/abs/quant-ph/0106024>
<http://dx.doi.org/10.1103/PhysRevLett.88.040404>
- [132] M. Fox, *Quantum optics: an introduction*. OUP Oxford, 2006, vol. 15.
- [133] R. T. Thew, A. Acin, H. Zbinden, and N. Gisin, “Bell-type test of energy-time entangled qutrits,” *Physical review letters*, vol. 93, no. 1, p. 010503, 2004.
- [134] “Silicon Photonics Process Design Kit (APSUNY PDKv2.5a), <http://www.aimphotonics.com/pdk/>,” AIM Photonics. [Online]. Available: <http://www.aimphotonics.com/pdk/>
- [135] T. F. Da Silva, D. Vitoreti, G. Xavier, G. Do Amaral, G. Temporao, and J. Von Der Weid, “Proof-of-principle demonstration of measurement-device-independent quantum key distribution using polarization qubits,” *Physical Review A*, vol. 88, no. 5, p. 052303, 2013.
- [136] S. Walborn, S. Pádua, and C. Monken, “Hyperentanglement-assisted bell-state analysis,” *Physical Review A*, vol. 68, no. 4, p. 042313, 2003.
- [137] “Pid theory explained.” [Online]. Available: <http://www.ni.com/en-us/innovations/white-papers/06/pid-theory-explained.html>
- [138] X. Xue, Y. Xuan, Y. Liu, P.-H. Wang, S. Chen, J. Wang, D. E. Leaird, M. Qi, and A. M. Weiner, “Mode-locked dark pulse kerr combs in normal-dispersion microresonators,” *Nature Photonics*, vol. 9, no. 9, p. 594, 2015.
- [139] A. Weiner, J. Heritage, R. Hawkins, R. Thurston, E. Kirschner, D. Leaird, and W. Tomlinson, “Experimental observation of the fundamental dark soliton in optical fibers,” *Physical review letters*, vol. 61, no. 21, p. 2445, 1988.
- [140] C. Bao, Y. Xuan, C. Wang, A. Fülöp, D. E. Leaird, V. Torres-Company, M. Qi, and A. M. Weiner, “Observation of breathing dark pulses in normal dispersion optical microresonators,” *Phys. Rev. Lett.*, vol. 121, p. 257401, Dec 2018. [Online]. Available: <https://link.aps.org/doi/10.1103/PhysRevLett.121.257401>
- [141] C. Souza, C. Borges, A. Khoury, J. Huguenin, L. Aolita, and S. Walborn, “Quantum key distribution without a shared reference frame,” *Physical Review A*, vol. 77, no. 3, p. 032345, 2008.

- [142] J. M. Lukens, A. Dezfooliyan, C. Langrock, M. M. Fejer, D. E. Leaird, and A. M. Weiner, "Orthogonal spectral coding of entangled photons," *Physical review letters*, vol. 112, no. 13, p. 133602, 2014.

VITA

VITA

Oscar E. Sandoval graduated with a B.S. degree - cum laude - in electrical engineering from the California State Polytechnic University, Pomona in 2013 and a Masters degree in electrical and computer engineering from Purdue University in 2015. He is currently pursuing a Ph.D. degree in electrical engineering from Purdue University, and is a research assistant in the Ultrafast Optics and Optical Fiber Communications Laboratory under the supervision of distinguished Professor Andrew M. Weiner. Oscar's research has led to various co-authorships and conference submissions. In addition to his research, Oscar has mentored undergraduate researchers and has taught an undergraduate optics lab. Oscar's current interests include electro-optics, frequency combs, mentorship, horology, and spending time with his partner (Katie Hummel) and her family down the Jersey Shore, and his familia back home on the southeast side of Los Angeles, CA.